

2. ELECTRON BEAM

2.1 Design Concepts

Storage Ring

The current design of the electron beam envisages a race-track shaped storage ring for polarized electrons of 10 GeV with provisions to accommodate energies as low as 5 GeV, and for self-polarized positrons of 10 GeV. The main design goals are high beam polarization and maximum luminosity. The central concept arrives at a luminosity of $0.44 \times 10^{33} / \text{cm}^2 / \text{s}$ based on conservative beam stability and beam-beam interaction limits assuming a single interaction region for electron and hadron beams and two additional hadron-hadron interaction points. A more aggressive scheme is outlined producing a luminosity of $1 \times 10^{33} / \text{cm}^2 / \text{s}$ requiring further R&D towards higher beam-beam tune shifts. The over-all dimensions of the proposed electron ring are governed by the following considerations: The length of the straight sections is given by the space needed for spin rotators (vertical spin in the arc, longitudinal spin at the intersection point), a polarimeter, and the interaction region including the detector. The minimal bending radius in the arcs is determined by the allowable synchrotron light power density deposited on the beam vacuum chambers and the maximal arc radius is governed by the acceptable self-polarization time for positrons, packing fraction of bending magnets and cost.

Optimization within these boundary conditions resulted in an electron (positron) ring of 1/3 of the RHIC circumference ($L=1278\text{m}$) with straight sections of 160m, an arc radius of 152m and a bending radius of $\rho=81\text{m}$ (53% packing fraction). The expected synchrotron power density from a 0.5A, 10 GeV electron beam is $p=11 \text{ kW/m}$, somewhat higher than values at existing B-factories but well within their upgrade goals and a positron polarization time of $\tau = 22 \text{ min}$ at 10 GeV. In view of the relatively firm lower limits on the length of the straight sections and on the required space between bending magnets (packing fraction) which together make up over 50% of the ring circumference, and the strong dependence on ρ of the synchrotron light power density ($\propto \rho^{-2}$) and the polarization time ($\propto L\rho^2$), the choice of the ring circumference is quite restricted: e.g. a ring circumference of 1/4 of RHIC would result in $p \approx 17 \text{ kW/m}$, $\tau \approx 10 \text{ min.}$; for 1/2 of RHIC circumference, $p \approx 4 \text{ kW/m}$, $\tau \approx 81 \text{ min.}$

The current lattice design features an adjustable emittance to optimize luminosity at a range of energies. It features a "flat" beam with a vertical-to-horizontal emittance ratio of 0.18. Although this is not optimal for highest luminosity, the creation of "round" beams without losing polarization is not trivial and needs to be explored further, possibly requiring R&D on the existing storage ring at Bates.

One of the most demanding problems is to design a lattice which preserves polarization (high equilibrium polarization) in the presence of magnet and alignment imperfections. One specific concern is the effect of solenoidal spin rotators proposed for the interaction straight section. Their use would provide near-longitudinal polarization at the interaction point for a range of energies without requiring mechanical reconfiguration of the spin rotators.

The requirement of varying the ion beam energy and thus ion beam velocities implies that either or both of the electron and ion beam ring circumferences have to be adjustable. Three schemes to accomplish this were considered. The first of splitting the 3m long lattice bending magnets into three units (super-bends) to vary the path length through the benders would only allow a path length

change of about 5.5 cm or $4.3 \cdot 10^{-5}$ of the ring circumference to accommodate ions of 100 GeV/amu at the cost of reducing the electron energy to 7 GeV to keep synchrotron power density below 11 kW/m. A second scheme of moving one entire arc section uniformly to lengthen the straight sections would accommodate any ion energies without compromising the e-ring lattice or requiring any ion ring adjustment. The cost of the mechanical engineering for such a moveable arc is still being evaluated and may prove this scheme impractical. A third possibility is a number of fixed chicanes in the arcs which would allow discrete path length increases accompanied by a small continuous path variation in RHIC. A typical arrangement of four chicanes containing 6 displaced magnets and 6 displaced quadrupoles (3 FODO cells) and a continuous path length adjustment of .6m or $1.6 \cdot 10^{-4}$ of the RHIC circumference would allow a continuous ion energy range from 23 to 250 GeV. It would increase the cost of the e-ring arcs by about 20%. An optimized scheme is the subject of further studies.

Injection

Polarized electrons are to be injected into the ring at full energy (5 to 10 GeV) rather than relying on energy ramping and self-polarization of electrons injected at low energy. Although low-energy injection would be cheaper, full energy injection provides more stable, easier ring operations by avoiding ramping, and the possibility of “topping” up the stored electron beam to maximize average luminosity. There is no need for wigglers to self-polarize electrons below 10 GeV (self-polarization for ramped beams is indispensable since ramping most likely destroys any initial polarization. Full-energy polarized injection also would allow frequent injections should beam depolarization times prove too short.

An injection scheme is proposed using a 5 GeV linac with a Recirculator that would also naturally lend itself to include a positron source.

The variable pulse repetition frequencies required for the e-ring for different ion energies and the fixed linac frequency require special measures in the polarized electron source and injection to the linac to provide both relatively high pulse charge at variable pulse frequency.

Interaction Region

The design of the interaction region has to fulfill a number of conditions: maximum luminosity requires β -functions of the order of 10 to 20 cm for both electron and ion beams and both beams have to be separated less than 5m past the interaction point to avoid second collisions of the 28 MHz pulse trains. Both requirements limit the free space around the interaction point and restrict the available solid angle for detection of the reaction products from the electron-ion collisions. At the same time, background from intercepted synchrotron radiation produced in bending and focusing the electron beam must be minimized. Finally, the effects of the solenoidal magnetic field of the particle detector must be neutralized to maintain beam stability. In order to minimize depolarization of the electron beam, vertical bending of the electron beam should be avoided while vertically bending the ion beam requires large bending strengths. Keeping both beam in the horizontal plane then poses the problems of beam crossing in the arcs of the electron and ion rings.

An interaction region conceptual design addressing all those conditions has been arrived at using half-quadrupoles to separate and focus the interacting beams without unduly restricting solid angles for particle detection and minimizing synchrotron background. Further development of these ideas will require close cooperation with detector design.

2.2 Geometry and Location at the BNL Site

Existing RHIC collider has six interaction regions. Two of them, at 6 and 8 o'clock, are occupied by two large detectors, STAR and PHENIX. These regions are excluded from consideration for additional electron accelerator as they will continue their work for the physics studies with ion-ion collisions.

Although the two smaller experiments, PHOBOS and BRAHMS located at 10 and 2 o'clock interaction regions, correspondingly, will finish their experimental program before the eRHIC era, these regions also can not be used for eRHIC. The warm sections around 10 o'clock interaction region, where the PHOBOS detector is located, are used for the beam dump purposes. The electron ring cannot be put at 2 o'clock because of environmental restrictions due to a water flow of the Peconic River.

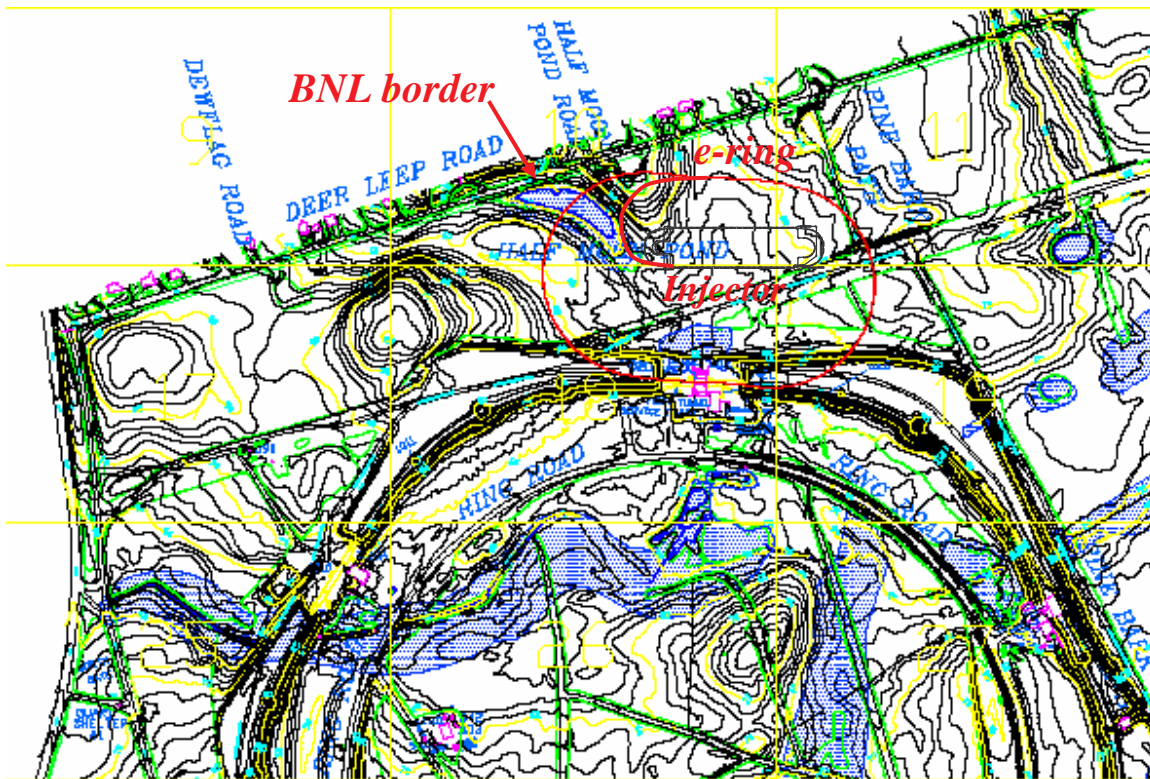


Figure 2.2-1: The scheme of the electron accelerator location at 12 o'clock RHIC region.

The remaining two interaction regions at 12 and 4 o'clock can be considered as possible locations of the electron accelerator. The first choice could be the northern 12 o'clock interaction region as shown in Figure 2.2-1. The electron ring does fit within the BNL site but one section is relatively close to the laboratory border, about 50m at the closest point. There is a residential area outside of the laboratory border and this could be considered as definite disadvantage. The major advantage of that location is an already prepared excavation for a new detector. Because of limited space available in the 12 o'clock, the electron injector has to be placed inside the electron ring circumference, as presented in Figure 2.2-1. The injector design based on normal conducting linac could be easily placed inside the electron ring circumference.

2.3 Injector Accelerator

2.3.1 Polarized Electron Photoinjector

Peak Current and Timing Requirements:

The advancement in the polarized electron source technology over the past decade at nuclear and particle physics accelerator centers have been substantial [1,2,3]. Highly polarized electron beams of diverse peak currents, time structures and duty cycles including CW beams are now routinely produced at Jefferson Lab, SLAC, HERA, MIT-Bates, Mainz and Bon [1,2,3,4,5]. These polarized injectors are based on photoemission process from strained GaAs based photocathodes illuminated by laser radiations at 800-850 nm followed by an extraction process with high gradient electric field. The stored current of order 0.5 A of highly polarized electron beam in a storage ring such as eRHIC normally would represent a modest technical requirement on present state of the art polarized source technology. The ability to stack multiple pulses in the storage ring presents a great advantage in achieving high stored average currents from repeated injection with relatively low linac peak currents. For instance, at MIT-Bates, highly polarized stored currents of few 100 mA are now routinely achieved by stacking of microsecond long pulses ~2 mA high. However, the collider nature of eRHIC with synchronized bunches precisely matching the proton bunches represents a great challenge to the injector setup and the polarized source architect. In this section we present two architects for the polarized injector and the front end of the accelerator that in principle can meet the injection requirements of the synchronized bunches for eRHIC. These options are presented assuming a room temperature copper accelerator at 2856 MHz. Modification to the architect of these options may be required if a superconducting RF linac is used instead. The principles of the two options are still valid for SRF linac. The variations between these two options are in the time structure of the photoemission drive laser systems and in the electron beam line for bunching and chopping functions. In this section, the photoemission process from high polarization photocathodes are described followed by a description of the two options for the laser systems for the source.

High Polarization Photocathodes

Polarized electron beams for accelerators are generated by photoemission process using longitudinally polarized laser lights at 750-850 nm from the surface of GaAs based photocathodes under UHV conditions. The electrons are extracted from the surface using high gradient field present between the anode and cathode electrodes. The maximum theoretical limit for degree of polarization from a bulk GaAs surface is 50% and ~40% in practice due to depolarization effects in the bulk. The photoemission process in bulk GaAs is the simultaneous excitation of electrons in degenerate states in the valance band to the conduction band. To the degree that this degeneracy in the valance band is removed, higher degree of polarization can be achieved. A common technique to remove the existing degeneracy is to introduce strain in the lattice by growing GaAsP layers on substrate GaAs. The lattice mismatch between GaAs and GaAsP produces mechanical strain near the boundary surface [6]. The active layer must be very thin of the order few hundred nm to keep the strain present near the surface of the photocathode. The reduced depth in the active layer causes a substantial reduction in the Quantum Efficiency (QE) of the photocathode. QE is the fractional number of electrons generated by a single photon. QE for bulk GaAs photocathodes with pol~30-40% is of the order of 1-10 % and 0.01-0.1% for high polarization strained GaAsP, smaller by two decades. The high

polarization photocathodes therefore, have the inherent problem of low QE's. With a laser radiation of wavelength λ and power P, the maximum peak current generated from a photocathode of appropriate band gap structure is given by

$$I(\text{mA}) = \frac{\text{QE} \times P(\text{mW})\lambda(\text{nm})}{1239}$$

For instance, with $P=1\text{W}$, $\text{QE}=0.1\%$ at $\lambda=800\text{ nm}$, a peak current of $\sim 0.64\text{ mA}$ can be generated. As shown in Figure 2.3.1-1, the QE and polarization are strong functions of λ .

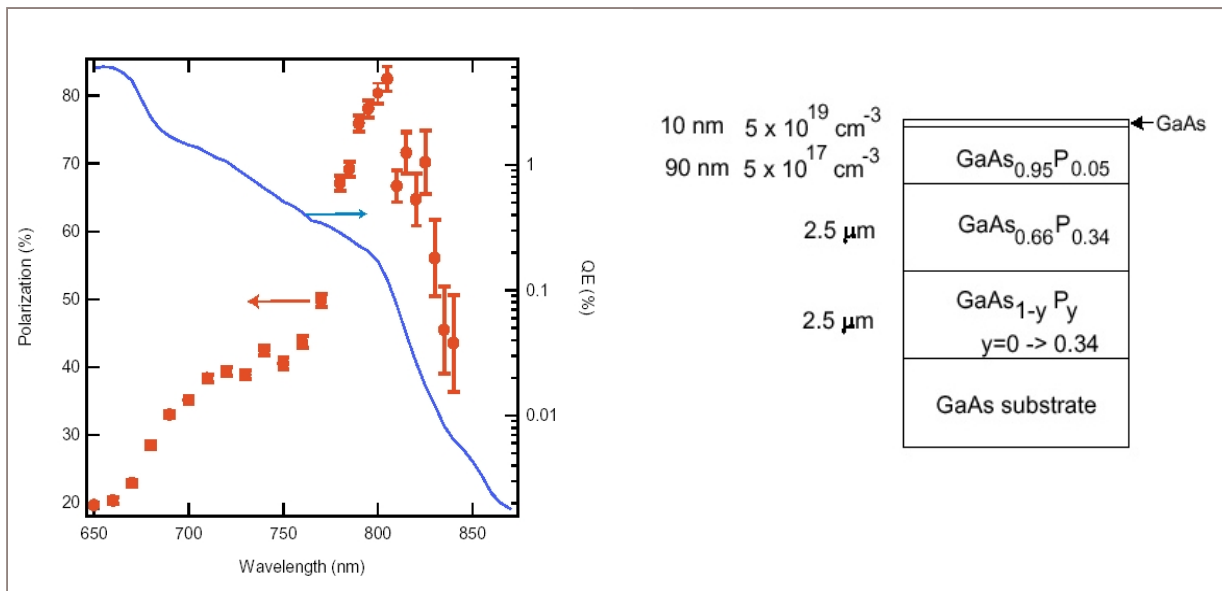


Figure 2.3.1-1. (Left) Photoemission data on a GaAsP from SLAC [7] showing Polarization and QE as a function of wavelength. (Right) A schematic diagram of the lattice structure of a high polarization high gradient doped strained GaAsP photocathode [8] now in use at SLAC and MIT-Bates. The peak polarization for this sample is near 800 nm where commercial high power lasers are more readily available. The 10 nm thick layer is highly doped to reduce the surface charge limit effect.

Surface Charge Saturation Effect

In a perfectly atomically clean and freshly activated photocathode, the extracted charge is proportional to the incident laser power. However, as the QE of the photocathode decreases due to surface pollution, the relationship between the laser power and the extracted charge begins to deviate from linear. This is particularly pronounced at high laser power densities where due to an abundance of negative charges on the surface, the effective work function near the surface is increased causing a reduction in the extracted charge per bunch. This effect has been observed at SLAC and at MIT-Bates and studied in great detail at SLAC [8]. Figure 2.3.1-2 shows data from the MIT-Bates polarized injector that clearly indicates the deviation from linear as the photocathode is aged over the course of many months. As charge saturation effect increases more laser power is required for producing the current required. To reduce the surface charge limit in the high gradient doped sample currently used at SLAC and MIT-Bates, the top 10 nm GaAs layer is heavily doped. However, this thin layer is evaporated after several heat cleanings at near 600 C. Care must be taken to reduce the number of heat cleanings for as long as possible. There are potentially several other methods to reduce the surface charge limit for high polarization photocathodes. These include cathode biasing, higher gun

voltage, higher QE and the use of superlattice structures [9]. These methods and have been tested in various photocathode and gun R&D programs mainly at SLAC and Nagoya but further R&D is required to make them practical.

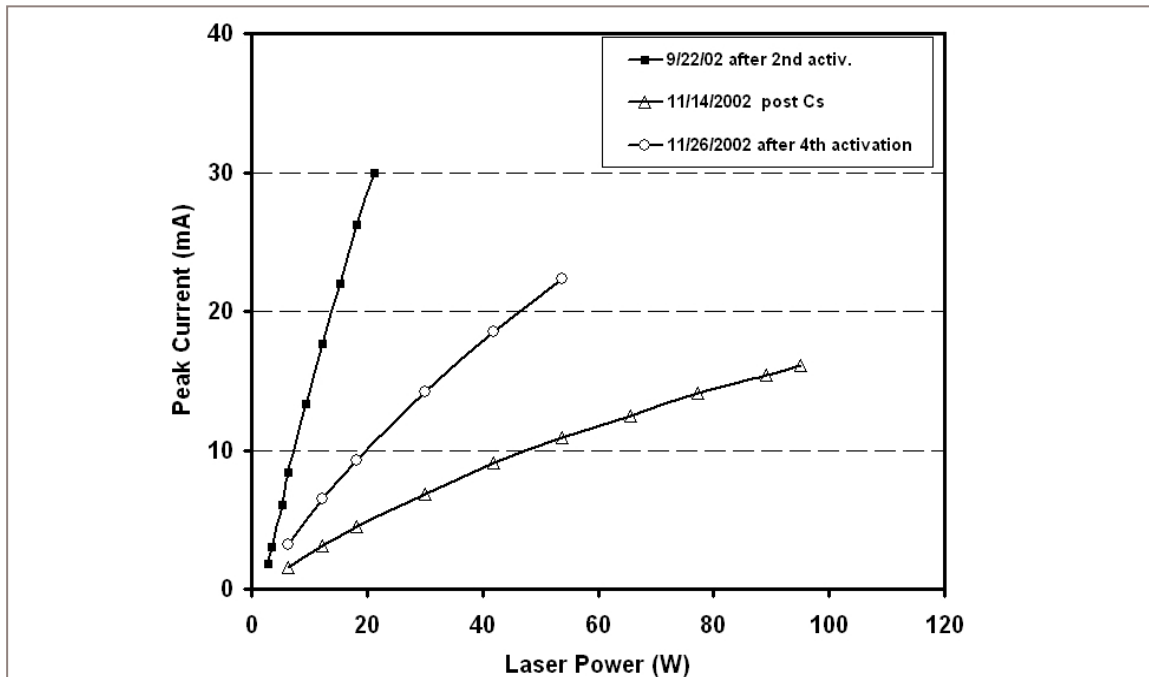


Figure 2.3.1-2. Peak current vs. laser power shown after several heat cleaning and activations for a two months period for the MIT-bates polarized injector. Due to surface charge limit effect the slope of the current vs. laser power decreased between 9/22 and 11/26 (squares and triangles). A heat cleaning and activation on 11/26 partially restored the slope (circles).

Charge per Bunch

Assuming 120 bunches distributed evenly in the eRHIC electron ring that is $4.3 \mu\text{s}$ long, a 480 mA stored current would correspond to 20 nC charge per collider bunch. With ~ 25 Hz injection repetition rate, and 10 minutes fill time a total of 15000 pulse trains (each $4.3 \mu\text{s}$ long , 35 MHz) with 1.3 pC in each bunch from the linac are required to stack the required 20 nC collider bunch. The charge per bunch from the polarized source to provide these bunches in the linac would be 1.3 pC divided by the capture efficiency of the injector to linac. The photoinjector to linac capture efficiencies will be discussed for the two photoinjector options discussed later in this section. Table 2.3.1-1 illustrates the important parameters of the collider ring, the linac and the polarized injector.

	Quantity	Value	Unit
Collider Ring	Stored current	480	mA
	Frequency	28.	MHz
	Ring circumference	4.3	μs
	Number of bunches in the ring	120	
	Charge per macroscopic bunch	20	nC
	stacking: pulse train rep. rate	25	Hz
Duration	10	minutes	
Total pulse train from injector	15,000 (25x10x60)		
Charge per bunch	1.3		pC
Photocathode	Bunch duration	~ 70	ps
	Bunch charge	1.3	pC
	Peak current	20	mA
Linac	Microscopic duty cycle (within 4.3 μs)	2×10^{-3}	
	Macroscopic duty cycle during fill	1×10^{-4}	
	Macropulse average current	40	μA
	Average current during fill	4	nA

Table 2.3.1-1. Important beam parameters for the collider ring, the electron linac and the polarized injector.

Two Options for eRHIC Polarized Injector

There are two classes of options considered for the eRHIC polarized injector. In one option, the radiation from a mode locked laser system at the collider frequency of 28 MHz (102nd sub-harmonic of 2856 MHz copper linac) is modulated and amplified with a shutter Pockels cell and an amplifier. The photoemitted electron beam has the synchronous bunch and time structures required for the collider ring. No further chopping or bunching is necessary. In the second option, a high power diode laser similar to one for the MIT-Bates polarized injector [11] produces DC radiation $\sim 4.3 \mu\text{s}$ long directed to the photocathode. The 28 and 2856 MHz RF structures are introduced into the electron beam by a 102 MHz buncher and a 28 MHz chopper synchronous with the collider ring followed by a drift and a chopper-buncher system at 2856 MHz. These two options are described here. The microscopic and macroscopic pulse structures for the injector and the collider ring are shown schematically in Figure 2.3.1-3. The microscopic and macroscopic duty cycles for the current pulse structures are 2×10^{-3} and 1×10^{-4} respectively. The overall duty cycle of the injector and linac is 2×10^{-7} .

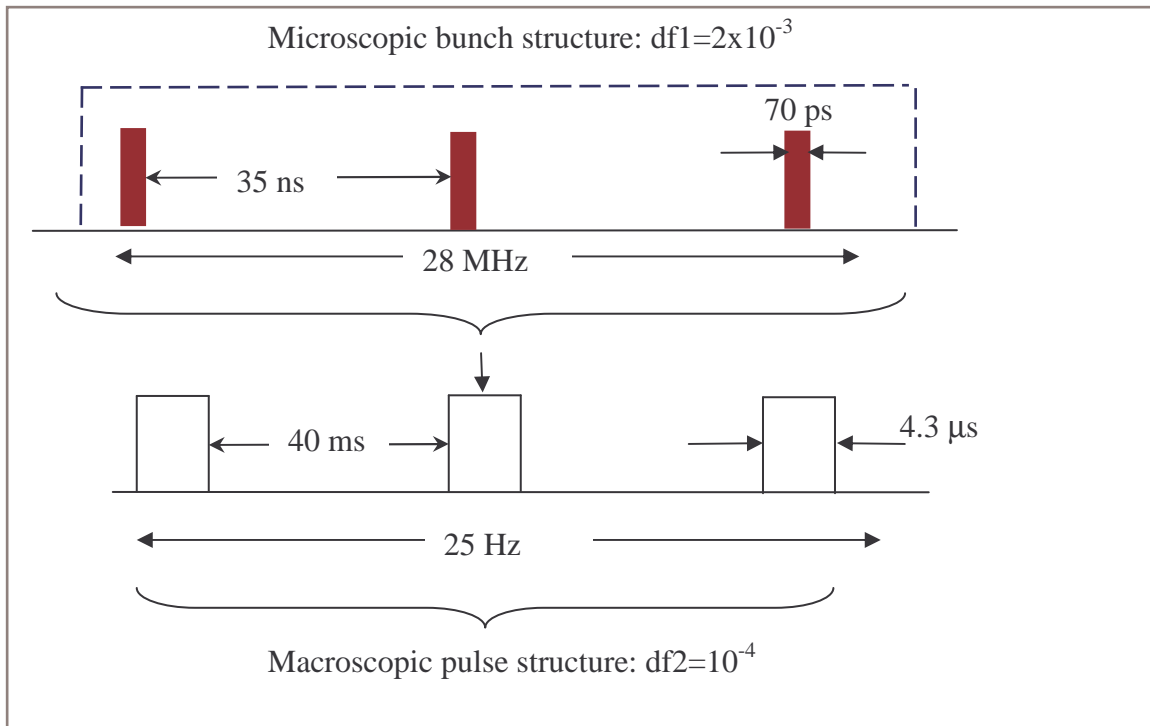


Figure 2.3.1-3. Schematic diagrams of microscopic bunch structure (top) and the macroscopic pulse structure (bottom). The duty factors are 2×10^{-3} and 1×10^{-4} respectively. The overall duty cycle of the injector and linac is 2×10^{-7} .

Option 1: Mode locked laser with synchronous amplifier

This option would consist of a mode locked laser at 28 MHz, 102^{th} -subharmonics of the 2856 MHz copper linac followed by a shutter Pockels cell (SPC) for generating the macroscopic pulse length of 4.3 μ s and a possible laser amplifier operating synchronously at the collider frequency of 28 MHz. The $\lambda/2$ SPC combined with a polarizer would provide the necessary switching of the beam for long pulses. These ~ 100 ps wide pulses should arrive synchronously within the 2 ns wide storage ring bunches. A schematic view of this laser system is shown in Figure 2.3.1-4. The macroscopic pulse length and repetition rates are ~ 4.3 μ s and ~ 25 Hz respectively.

Today, such mode locked lasers can produce 300 mW of average power. The peak power for 70 ps long pulses at 28 MHz would therefore be as high as 150 W as shown below

$$P_{peak} = \frac{\bar{P}}{f_{ring} * dt} \quad \text{with } f_{ring}=28 \text{ MHz and } dt=70 \text{ ps}$$

As stated earlier in this section, to fill the ring to 480 mA with 120 bunches in the ring with 10 minutes fill time would require bunches from the linac with ~ 1.3 pC charge each. The peak current for these 70 ps wide pulses would be about 18 mA. With a QE of 5×10^{-4} and $\lambda=800$ nm, to produce 18 mA peak would require peak laser power of order ~ 50 W which is factor of 3 less than what a 28 MHz mode lock laser can produce. This is the safety factor required for degradation of QE over time. The capture efficiency of the injector with this laser system is 50-100% depending on the beam optics in the injector.

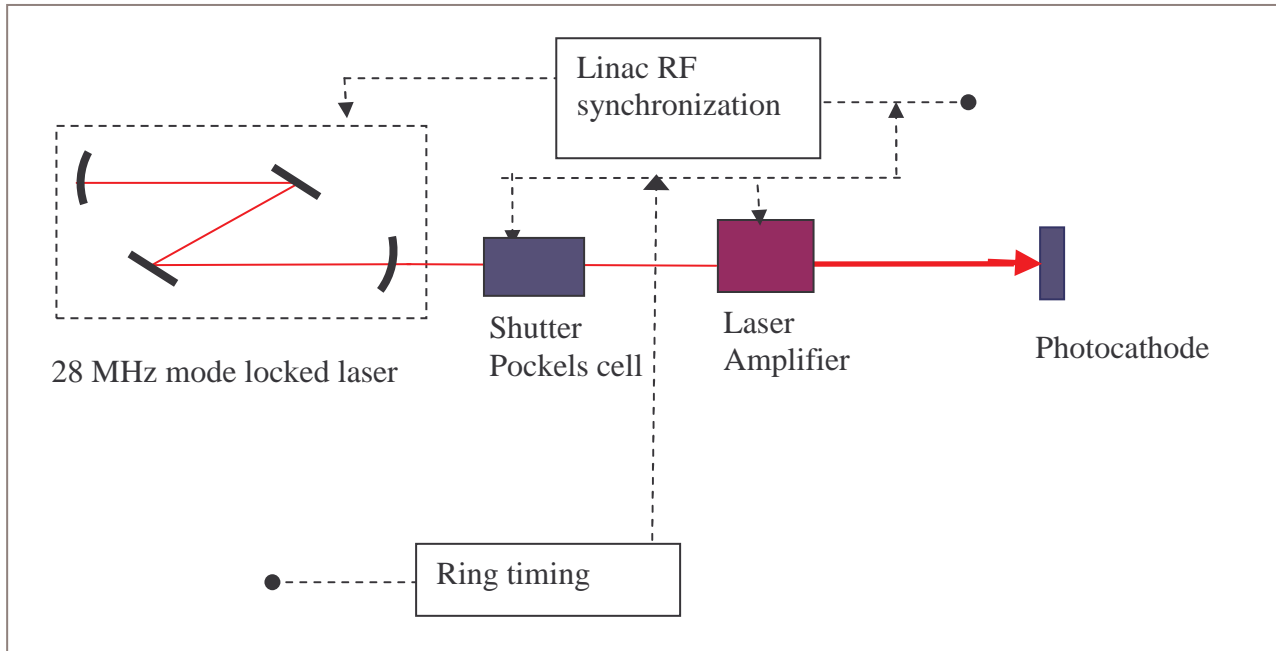


Figure 2.3.1.4. Schematic diagram of mode locked laser option for the eRHIC electron injector.

The drawback of this option is the timing stability requirement associated with mode locked lasers compared to DC or pulsed lasers. The advantage of this option is the built-in collider frequency into the photo-emitted electrons from the source. No chopping and bunching of the electron beam is necessary in this option.

Option 2: High power pulsed diode laser with e beam bunching

In this option, a high power fiber coupled DC diode laser produces $4.3 \mu\text{s}$ long laser pulses directed to the photocathode. After accelerating to several hundred keV, the photo-emitted polarized electron pulses pass through a structure consisting of a 102 MHz buncher and drift cavity, a 28 MHz chopper synchronous with the collider ring, and a 2856 MHz chopper and buncher system. The purpose of the 102 MHz buncher and the drift is to increase the peak current by a factor of 5-10 by compressing each 10 ns cycle down to about 1 ns through velocity bunching at ~ 200 keV in a 5-10 m drift space. The corresponding drift space for a 28 MHz buncher is unrealistically long and the bunching gain for a 476 MHz buncher is not as much as the one from a 102 MHz buncher. Figure 2.3.1-5 shows this option schematically. As stated above, the charge per linac bunch required for the collider is ~ 1.3 pC. The requirement on the peak current from the source will be reduced by a factor of 5-10 if the 102 MHz buncher could efficiently capture a total of ~ 1 ns of the DC beam near the zero crossing of the sinusoidal RF and compress it down to ~ 200 -100 ps. The peak current in the linac for a 70 ps wide bunch and 1.3 pC charge is 18 mA. With a 102 MHz bunching fraction F_{bunch} , and a linac capture efficiency $\epsilon_{\text{capture}}$ the required peak current in the polarized injector before bunching would then be

$$I_{\text{peak}} = \frac{I_{\text{peak}}^{\text{linac}} * \epsilon_{\text{capture}}}{F_{\text{bunch}}}$$

Assuming a linac capture efficiency of $\epsilon_{\text{capture}}=0.5$ and a bunching factor of $F_{\text{bunch}}=5$, the required peak current from the source to meet the linac charge per bunch of 1.3 pC is ~ 7 mA. This is quite possible with a high power diode laser system such as one used at MIT-Bates illuminating a high polarization photocathode that is not highly surface charge limited.

The advantage of this option is the simplicity and the stability of the DC high power diode laser array system that is commercially available and as the operational experience at MIT-bates indicates, they are trouble free and maintenance free operating for years. The drawback of this option is the complex chopping and bunching elements on the electron beam and the less than desired low capture fraction between the photocathode and accelerator.

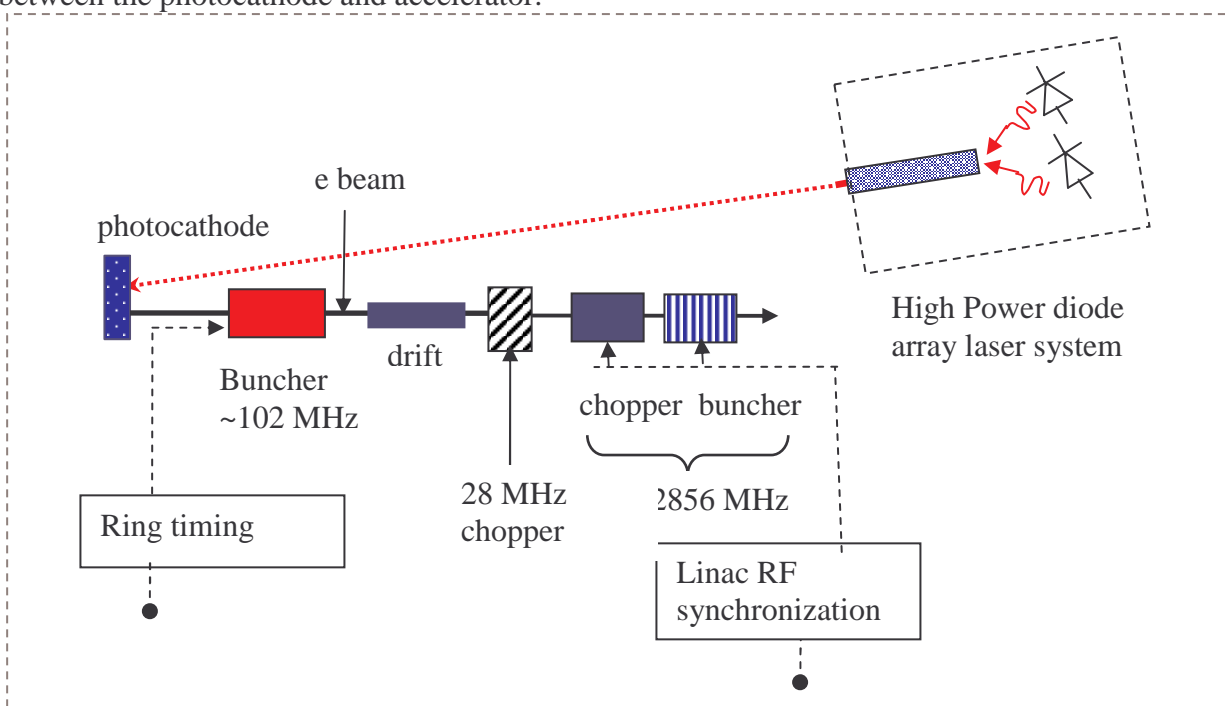


Figure 2.3.1-5. Schematic diagram of the eRHIC electron injector utilizing high power pulsed diode laser and electron beam bunching. The ~ 102 MHz buncher and the drift are intended to reduce the peak current requirements for the injector.

Multiple Injectors and Load Lock System:

For increase in the operation efficiency of the accelerator it is prudent to have a dual polarized injector each consisting of a polarized gun and the initial beam optics elements connected to the front end of the accelerator with isolation gate valves. This dual setup would permit the operation of one of the injectors at a time and the second as a stand by for backup. In addition, the gun chamber can be equipped with a load lock system that would provide the capability of loading of photocathodes into the gun assembly without a lengthy bakeout of the gun chamber often necessary to achieve UHV conditions. The SLAC polarized injector for instance, has a load lock system in use for many years. A load lock system is a more complex multiple chamber system with moving parts under UHV

conditions. However, a load lock system with proper design would provide up to half a dozen photocathode samples that can be moved into the photoemission position.

References:

1. “*Status of the Jefferson Lab Polarized beam*”, J. Grames, AIP proceeding of SPIN2002 Vol. 675 p1047.
2. “*The SLAC Polarized Electron Source*”, J. E. Clendenin, AIP proceeding of SPIN2002 Vol. 675 p.1042
3. “*MIT-Bates Polarized Source*”, M. Farkhondeh, PESP2002 workshop, Danvers, MA, AIP proceeding of SPIN2002 Vol. 675 p.1098.
4. “*Status of the polarized source at MAMI*”, K. Aulenbacher, AIP proceeding of SPIN2002 Vol. 675 p1088.
5. “*The polarized Electron Source at ELSA*”, W. v. Drachenfels, AIP proceeding of SPIN2002 Vol. 675 p1053.
6. T. Maruyama, et. al., Phys. Rev. Lett. **66** (1991) 2376.
7. T. Maruyama et al., NIM A492, 199(2002)
8. Bandwidth Semiconductor Inc., Bedford, NH.
9. “*Suppression of the Surface Charge Limit in Strained GaAs Photocathodes*”, T. Maruyama, AIP proceeding of SPIN2002 Vol. 675 p1083.
10. Jpn J. Appl. Physics Vol. 34 (1995) pp. 355, and SLAC-PUB-6350, July 1994
11. Spectra-Physics Opto Power diode laser model OPC-DO60-mmm-FC. Also” *High power Diode Laser System for SHR*”, E. Tsentalovich, AIP proceeding of SPIN2002 Vol. 675 p1019.

2.3.2 eRHIC Injector

Preliminary Design Considerations for a 10 GeV Electron/Positron Accelerator

The baseline injector for the proposed eRHIC collider is a 10 GeV machine capable of accelerating either electrons (polarized) or positrons (unpolarized). The successful realization of the eRHIC physics program requires the highest possible luminosity, $\sim 10^{33} \text{ cm}^{-2} \text{ s}^{-1}$, and highest possible polarization of the colliding beams. To maintain the optimum currents, ~ 0.5 Amps, in the eRHIC electron/positron (e-/e+) ring and preserve the high electron polarization available from today's photoinjectors, $P > 70\%$, the most straightforward technique is to inject into the e-/e+ ring at its operating energy of up to 10 GeV.

Injecting on energy into the eRHIC e-/e+ ring has the three important benefits listed below.

- 1) **Stability:** Injecting at the full energy allows the e-/e+ ring to run under CW conditions. The stability and control will be superior for a ring with static conditions, compared to one where the beam energy is ramped. This stability will be important for the fine tuning of the e-/e+ ring that will be required to maximize the luminosity of the colliding beams.
- 2) **Rapid Filling:** Injecting on energy allows for rapid filling of the e-/e+ ring. This will reduce the filling time that is required for the e-/e+ ring. If the filling time is too long it will reduce the integrated luminosity. In practice, the eRHIC collider fill time is likely to be limited by the fill time required for the hadron side. However, it is still desirable to keep the e-/e+ fill time short enough so it has a negligible impact on the integrated luminosity. Further, on energy injection allows a "top-off" mode of operation where the current in the electron ring is periodically topped-off at intervals which are much more frequent than the hadron storage time. This will increase the maximum achievable peak luminosity by allowing the eRHIC ring to operate at a higher beam-beam tune shift. The shorter e-/e+ lifetime is compensated by more frequent filling. This also increases the integrated luminosity by running the electron current at nearly constant value at all times.
- 3) **Highest Electron Polarization at all Energies/High Positron Polarization at 10 GeV:** For low energies, 5 GeV, the electron polarization will be determined by the source. This avoids the high radiation load and complexity in the main ring that would be required to radiatively polarize electrons at the low energies. On energy injection also avoids depolarization that is likely to occur if the main ring is ramped. This depolarization occurs principally as spin resonances are crossed during the ramping cycle. This effect has been observed at many existing synchrotrons [1, 2] and would severely impact the physics program requiring polarization observables.

The performance requirements of an on energy injector are listed below:

- Accelerate polarized electrons to the e-/e+ ring operating energy, a maximum of 10 GeV.
- Preserve the electron polarization during the acceleration process.

- Create and accelerate unpolarized positrons to the e-/e+ ring operating energy, a maximum of 10 GeV
- Fill the e-/e+ ring to its operating current of 0.5 A in 10 minutes for either positrons or electrons
- Maintain the capability to “top off” the current in the e-/e+ ring by delivering a pulse of a few mA every few minutes.
- Fill the e-/e+ ring with the bunch structure required by the collider. The present design calls for 35 ns bunch spacing. The ideal injector will deliver good bunch to bunch charge uniformity, <1%. The injector should allow flexible filling patterns including other bunch spacings and unpopulated bunches to limit ion trapping and accommodate finite rise time of the e-/e+ ring injector elements.

Since the eRHIC program uses stored colliding beams with lifetimes well in excess of one hour the average current requirements of the injector accelerator complex are quite modest. However, details of the collider timing requirements place some additional demands on the injector accelerator complex. Table 2.3.2-1 lists the necessary properties of the beam delivered to the eRHIC electron/positron ring. Ideally the positron beam would meet the same performance specifications (excepting polarization) as the electron beam.

Beam Energy	10 GeV
Macro Pulse Repetition Rate (during fill)	30 Hz
Electron Bunch Spacing	35 ns
Bunch Train Length	4.3 μ s (single turn in the e-/e+ ring)
Charge/Bunch	3 pC
Fill time (Machine on time)	<10 minutes
Time between fills (Machine idle time)	>2 Hrs
Injection Efficiency (Qring/Qsource)	>50%

Table 2.3.2-1. eRHIC electron/positron injector accelerator parameters.

The small macro current of 100 μ A in table 2.3.2-1 results in very small beam loading for all of the injector variants considered below. The parameters here reflect a mode of operation where the eRHIC e-/e+ ring is not “topped-off.” If a “top-off” mode is adopted the accelerator would be required to periodically wake up and deliver a pulse to the eRHIC e-/e+ ring at approximately 10 minute intervals.

While several multi-GeV injectors are operational at existing facilities [3-5], there is considerable performance risk for the eRHIC physics program depending on the particulars of the injector design. As a principle design tenet we assert that the maximum luminosity of the collider and maximum polarization of the electron/positron ring should not be limited by the performance of the injector.

Several distinct accelerator topologies appear to have the potential to meet these requirements. At this early stage of design we consider three variants:

- 1) Recirculating copper S-band linac,
- 2) Recirculating superconducting linac
- 3) Figure-eight booster synchrotron.

Considerations that will affect the choice of injector include performance, performance risk, reliability, and cost. Another important factor will be the possible use of the eRHIC injector for multiple purposes on the Brookhaven site. At this point all three topologies are viable options. Each is presented in more detail below.

Recirculating Copper Linac

Figure 2.3.2-1 shows a possible layout of an injector based on a copper linac and recirculator. Here the linac structures are 3 m SLAC 2856 MHz traveling wave sections. The 2856 MHz frequency is well established and the accelerator and high power RF sources are commercially available. The performance characteristics of this technology are known and therefore this design presents little risk for an eRHIC injector.

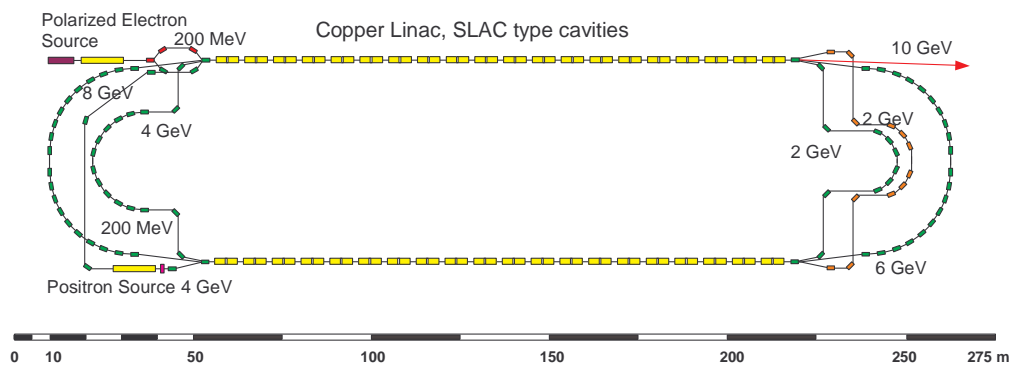


Figure 2.3.2-1. eRHIC injector accelerator. A polarized electron beam is accelerated to 200 MeV and injected into a 2 GeV copper linac. At the end of the linac the beam is transported through a 180 deg isochronous recirculation arc into a 2nd 2 GeV linac where the beam is accelerated to 4 GeV. One and a half subsequent recirculations increase the beam energy to a total of 10 GeV. Positron production is supported.

The parameters of a copper linac that would satisfy the eRHIC requirements are listed in Table 2.3.2-2. Below we consider a pre-conceptual design of a copper accelerating “module,” where a module consists of a 350 kV power supply, a capacitor bank, a HV modulator switch, a 50 MW klystron, RF waveguide distribution, 2 three meter accelerating sections and their associated RF loads.

Linac Frequency	2856 MHz
Linac Gradient	16 MV/m
Number of Linacs	2
Active Linac Length	120 m
Linac Length	170 m
Linac Section Length	3 m
Shunt Impedance	53 MOhm/m
RF Input Power/Section	25 MW
RF Macropulse Length	10 μ s
Beam Pulse Length	2 μ s (one recirculation period)
Macropulse Current	0.1 mA
Pulse Repetition Rate	30 Hz
Section Fill time	0.820 μ s
Klystron Power	50 MW
Klystron Current	350 A
Klystron Voltage	350 kV
Klystrons/Modulator	1
Accelerating Sections/Klystron	2
Number of Sections	80 (40/Linac)
Number of Klystrons	40 (20/Linac)

Table 2.3.2-2. RF parameters – Copper S-band eRHIC injector linac.

The pulse repetition rate of 30 Hz is a reasonable requirement for a linac of this type. An average power of 30 kW per klystron is expected. These pulses would be line locked for increased stability. The rate is also well matched with the main eRHIC damping time of 7 (58) ms at 10 (5) GeV. Optimal filling of the main ring is achieved at repetition rates equal to approximately three inverse damping times.

The copper linac is limited to a smaller number of recirculations (2-3) due to constraints on the pulse widths available from the high power klystrons, i.e. pulses <10 μ s in duration. The circulation time in the linac is 2 μ s. So the required RF pulse width for two turns of beam acceleration is 6 μ s where two microseconds have been allocated for the RF turn on. This is a good match with the pulse widths that are available from these high power 50 MW klystrons. For 6 μ s of RF 8 μ s of video current from the klystron would be required.

A beam pulse length of 2 μ s is matched to the injector circulation time so that a “head-to-tail” mode of operation may be used. This keeps the current in the linac constant after the initial turn and limits the impact of beam loading. The linac would be required to pulse twice to fill the full 4.3 μ s circumference of the e⁻/e⁺ ring.

In principle RF compression (SLED) technology could be used to increase the peak power from the klystron from 50 to ~100 MW. Higher gradients of 24 MV/m would be possible. However typical pulse widths from these compression schemes are 1-3 μs long and therefore not readily compatible with a recirculating linac. Therefore we have not adopted RF compression for this variant.

More detailed considerations of the RF sources and modulators for a copper linac are presented in the following sections.

Pulse-Modulated RF Power Amplifier

The existing technology baseline is the Toshiba 50 MW peak-power 2.856 GHz klystron MVED capable of 10 μs pulse duration, at 40% efficiency, requiring 125 MW peak beam power input (350 kV beam voltage and 350 A beam current). An emerging technology option (development required) is the Multiple-Beam Klystron (MBK) with higher efficiency (50-65%), due to lower perveance of individual beams (typically 0.5 micropervs per beam, compared with 2.0 micropervs for single-beam gun), and operating at lower beam voltage, typically half that of single-beam klystron of same peak power, due to higher conversion efficiency and, more importantly, higher *total* beam perveance (typically 4 micropervs for 8-beam gun). A block diagram of a pulsed S-band transmitter is shown in figure 2.3.2-2

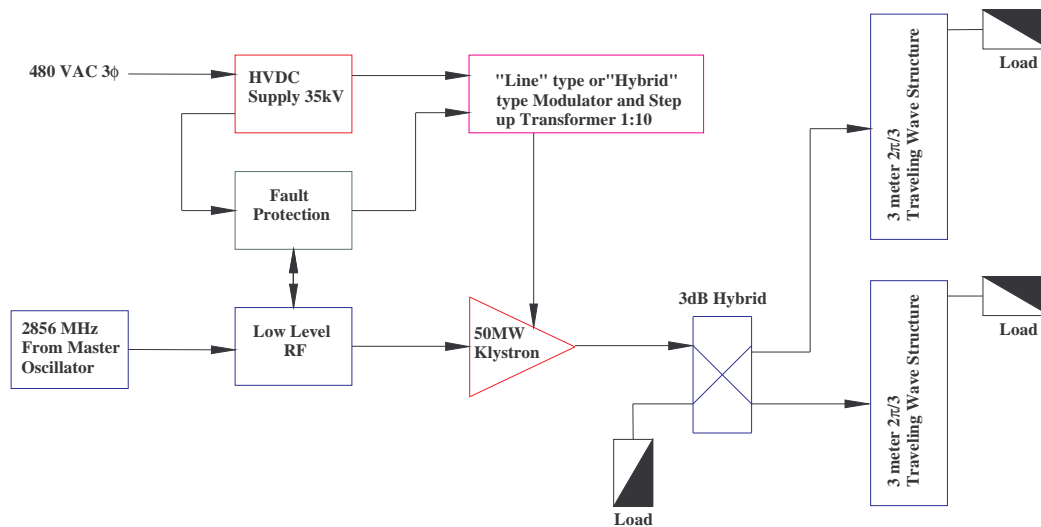


Fig 2.3.2-2 Block diagram of a Pulsed S- band Transmitter

Pulse Modulator

The traditional technology baseline is the “Line-type” modulator, as shown in Figure 2.3.2-3, using an artificial transmission-line pulse-forming network with characteristic impedance matched to transformed load (klystron beam) impedance, switched by half-control (closing switch only) such as Hydrogen Thyatron or high-current Thyristor stack. The pulse duration is determined by time delay

of network. The Klystron load is coupled by step-up pulse transformer, typically 10:1 turns ratio. All of the stored network energy is transferred to the klystron load each pulse. Referenced to pulse-transformer primary, the modulator switch must be rated at twice the output voltage, for normal operation, and twice the normal load current, for a short-circuit load fault condition, a non-simultaneous rating that is 4 times the load power under normal conditions. The switch peak power rating, therefore, must be 500 MW, for 125 MW peak load power.

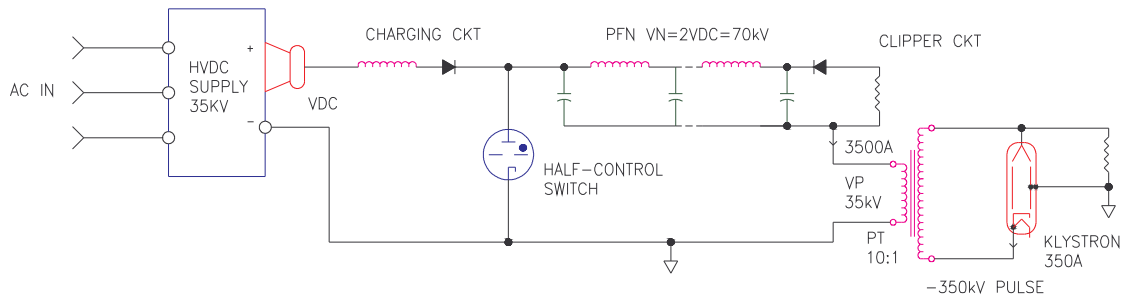


Fig. 2.3.2-3 Simplified schematic of basic “line” type modulator

An option is the so-called “Hybrid” modulator, as shown in Figure 2.3.2-4, using a step-up pulse transformer but with the PFN replaced by a capacitor bank and the half-control switch replaced with a solid-state full-control switch (turn-on and turn-off), comprising series-connected Insulated-Gate Bipolar Transistors (IGBTs). The duration of the output pulse is the same as that of the IGBT gate-drive. The voltage droop of the output pulse is determined by the ratio of capacitor-bank charge storage to the charge delivered to the load each pulse. Referenced to the pulse-transformer primary winding, the switch voltage rating is the same as the output voltage. Short-circuit fault current is interrupted by opening the IGBT switch (less than 1 μ -sec opening time). The switch peak-power rating is the same as the load power, or 125 MW, assuming a large capacitor bank, and negligible voltage droop. A variant replaces the capacitor bank with an under-matched PFN, having a characteristic impedance small compared to that of the transformed klystron beam impedance. PFN delay-time must be more than half of the longest output pulse duration. The output pulse has zero droop, but has a voltage step at the leading edge, (depending on degree of under-match), continuing throughout the pulse, and pulse-top voltage ripple, determined by number of network stages. The pulse duration is the same as the IGBT gate-drive. The switch voltage and power rating must be greater than output voltage and power, depending on degree of under-match (for instance, 10% greater, for 10% undermatch).

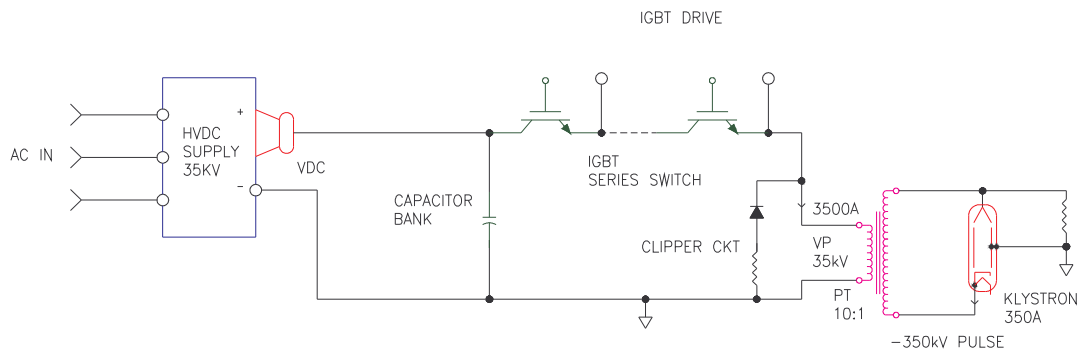


Fig 2.3.2-4 Simplified schematic of “hybrid” type modulator

Other options, in the category of emerging technology (development required) are the direct-drive, series-connected IGBT switch, with no step-up pulse-transformer, and an adaptation of the so-called “Marx” generator topology. Energy storage capacitors are charged from a relatively low-voltage DC source, in parallel, and discharged, in series, by means of IGBT switch modules distributed throughout the generator.

High-Voltage DC Power Supply

Except for the emerging-technology options, the required DC power supply output voltages is less than the peak pulse output voltage by a factor equal to the pulse-transformer turns-ratio. Notwithstanding the continuing improvement in power output capability of high-frequency switch-mode DC power supplies, the optimum power-supply topology is the poly-phase (typically 12-pulse) line-frequency transformer-rectifier. It is the simplest (no active components), most reliable (fewer components) and most efficient (lowest total losses) source of high-quality DC output. It is also the largest and heaviest, but these are factors of only secondary importance. Voltage regulation, soft-start, and high-speed fault disconnect can be provided by SCR primary conduction-angle control.

Recirculating Superconducting Linac

Figure 2.3.2-5 shows a possible layout of an injector based on a superconducting accelerator and recirculator. Here the TESLA frequency of 1300 MHz is chosen due to their established performance [6], but the use of other frequencies between 500 – 1500 MHz is also possible.

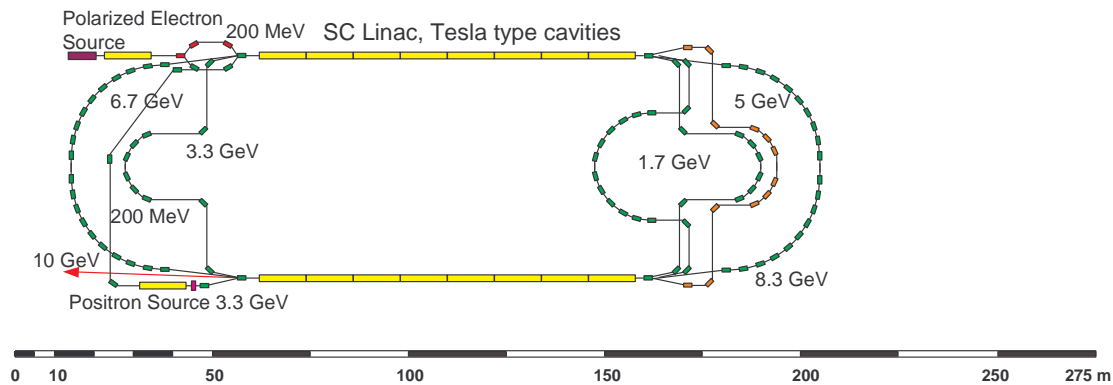


Figure 2.3.2-5. Same as Figure 2.3.2-1 except that here the linac is two 1.7 GeV superconducting TESLA style structures. The electron beam is accelerated through 3 revolutions before reaching the maximum eRHIC energy of 10 GeV. Not shown here, a positron damping ring may be necessary to limit beam losses in the superconducting structure. Notice that the scale of the superconducting complex is ~200 m x 50 m while the normal conducting is ~300 m x 50 m.

The parameters of a possible superconducting linac for eRHIC are listed below in Table 2.3.2-3 are baseline consideration of the superconducting version we use the parameters of a TESLA type 1.3 GHz accelerator.

Linac Frequency	1300 MHz
Linac Gradient	26 MV/m
Number of Linacs	2
Active Linac Length	64 m
Linac Length	92 m
Linac Cavity Length	1 m
Shunt Impedance (R/Q)	1038 Ohm
Cavities/Cryomodule	8
RF Macropulse Length	40 ms – CW
Average Macropulse Current	0.01 μ A
RF Pulse Repetition Rate	CW – 10 Hz
External Coupling (Q_{ext})	$2 \cdot 10^{+7}$
Cavity Fill time	1-4 ms
Klystron Power/Cavity	<10 kW
Cavities/Klystron	1
Maximum Heat Load at 2K	5 kW (for CW operation)
Average Heat Load at 2K	100 W (10 minute fill every 8 hrs) + 80 W (10 sec top up every 10 minutes)

Table 2.3.2-3. Parameters for a possible superconducting linac for eRHIC.

Unlike the copper linac, the number of circulations for the superconducting linac will not be limited by the maximum RF pulse width but by the complexity and cost of the recirculation. The cost differential for one incremental recirculation scales with the required length of the linac. The incremental linac cost for one additional recirculation is proportional to $[1/N - 1/(N+1)]$ where N is the number of recirculations. Further, each incremental recirculation arc is more expensive than the previous as it is transporting beam at a higher energy and must not interfere with the prior recirculation arcs. Figure 2.3.2-6 shows capital cost as a function of the number of recirculations, where a very simple cost model is adopted. The superconducting linac is costed at \$0.5M per active meter and the recirculator is costed at \$0.1M/m multiplied by a weakly increasing function which reflects the additional cost of transporting a higher energy beam. These considerations show that the largest cost benefit is in the first recirculation and that an optimum exists near two recirculations (three passes). Not included are the substantial offset costs of other accelerator systems including injector accelerator, cryogenic refrigerator, polarized electron source, positron damping ring and other infrastructure. This optimization can be compared with the existing Jefferson Lab Accelerator which has four recirculations (5 passes). Here the optimum (lowest capital cost) is at a lower number of turns than Jlab due to the high gradient, 25 MV/m available from the TESLA accelerating cavities.

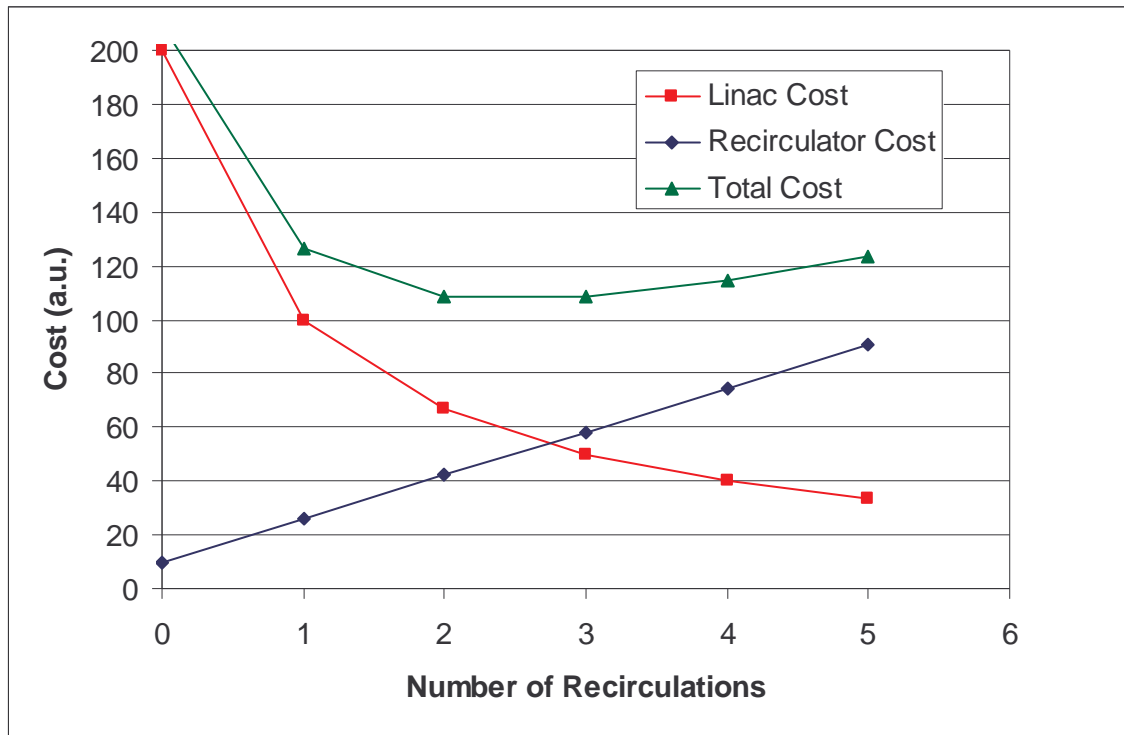


Figure 2.3.2-6. Capital cost scaling of a superconducting eRHIC accelerator injector as a function of the number of recirculations. The falling cost for the linac is balanced against a rising cost of the recirculator leading to an optimum near two recirculations (three passes).

The time structure of the beam required to fill eRHIC, (4 μ s, 0.1mA pulses at 30 Hz with a micro structure of 3 pC every 35 ns) gives a very modest requirement on the beam power that the RF sources need to deliver. The average beam current is less than 20 nA and therefore the beam power per cavity is less than one Watt. This is to be contrasted with the TESLA collider requirement where the macropulse beam current is 10 mA and the required RF power for the beam is 200 kW per cavity. Clearly a very different RF source is required. For negligible beam power as above and very low wall losses in the superconducting cavity ($P \sim 30$ W at 25 MV/m), the limitations on the minimum required RF power come from control and stability requirements of the superconducting cavities. Several institutions are pursuing active piezo-restrictive tuners that would control the cavity center frequency [7]. These devices show great promise, but require operation inside the cryomass and themselves have resonant behavior which places limits on their performance. Bates is developing an RF recycling concept that would make use of an external tuner and phase shifter, which would allow the RF sources to be much more closely matched to the intrinsic power requirements of ~ 100 W. This topology may allow the use of solid state amplifiers rather than klystrons. If successful, this effort would substantially reduce both the capital and the operating cost associated with the eRHIC a superconducting recirculating linac injector.

Another RF source, a 30 kW, 1.3 GHz Inductive Output Tube (IOT) is also under development by industry. This is a gridded vacuum tube which does not require the use of a High Voltage modulator. The removal of low level RF from the grid stops the current emission from the cathode, eliminating all power demand. Further, these devices have very high AC to RF efficiency ($\sim 65\%$) due to the bunched nature of the current emission from the cathode. The sinusoidal potential on the RF grid

limits the emission angle of the cathode to less than 180 degrees thus increasing the bunching (and RF source) efficiency. Since the IOT is capable of delivering 30 kW it has the ability to overdrive a superconducting cavity system during the long fill time (up to 4 ms) which requires only a few kW in equilibrium. This would make higher pulse rates possible for a pulsed superconducting eRHIC injector accelerator.

The 2K dynamic heat load of this accelerator is substantial, 30W per cavity at 25 MV/m and $Q_0 = 10^{10}$. For 128 cavities this will correspond to a refrigerator power demand in excess of 5 MW for CW operation of the linac. However the periodic nature of eRHIC filling, 10 minutes every eight hours, or 10 seconds every 10 minutes every half for top-up operation, allow operation of the linac with a macroscopic duty factor substantially less than 10%.

Positron losses must be kept to a minimum in the superconducting structures. Average positron currents of 20 nA, an average energy of 5 GeV and 50% current losses distributed over the length of the linac would add an additional heat load of 100 W at 2K. This should be contrasted with the dynamic heat load of ~ 5 kW for CW operation. More serious would be localized losses that could cause a cavity quench or even permanent damage to the superconducting structure.

The success of the JLAB superconducting recirculating accelerator demonstrates that such a machine could accommodate the requirements for electron injection into the

eRHIC e-/e+ ring. Further work is necessary to optimize this type of injector with consideration of recent progress in superconducting RF systems. The integration of positron acceleration will also require significant effort. A normal conducting positron pre-accelerator and damping ring may be required.

Figure Eight Booster Synchrotron

Another variant of the eRHIC injector that merits consideration is the figure eight synchrotron. This injector topology (Figure 2.3.2-7) is similar to that proposed for the electron Light Ion Collider (ELIC) presently under consideration by a machine design group at JLAB [8]. Due to the two opposing 270 degree arcs, this geometry has the attractive feature that the forward spin precession in one half is cancelled by that in the other half, i.e. the net spin precession is zero and independent of energy. Therefore this synchrotron should be able to ramp at moderate rates, ~60 Hz, with little loss of polarization. No spin resonances will be crossed during the ramping process.

The parameters of this type of synchrotron are listed in Table 2.3.2-4. For this geometry the synchrotron losses per turn at 10 GeV are substantial, 47 MV, so 75 MV of RF voltage must be installed in the ring. However, the average energy during the ramp is only 5 GeV, the supported current is also quite modest, I~1 mA and the synchrotron has a duty factor of less than 50%. Therefore the average beam power is much less than 10 kW. This combination of high voltage and low beam power might be well matched to a superconducting RF system. These RF parameters are quite distinct from the main eRHIC electron ring where currents of 0.5 A and synchrotron losses of 10 MV require in excess of 5 MW. A critical task for the “figure eight” geometry will be a detailed

simulation of the polarization behavior during the ramp to assess the level of polarization that would be achievable for the electron and positron beams delivered to the eRHIC main ring.

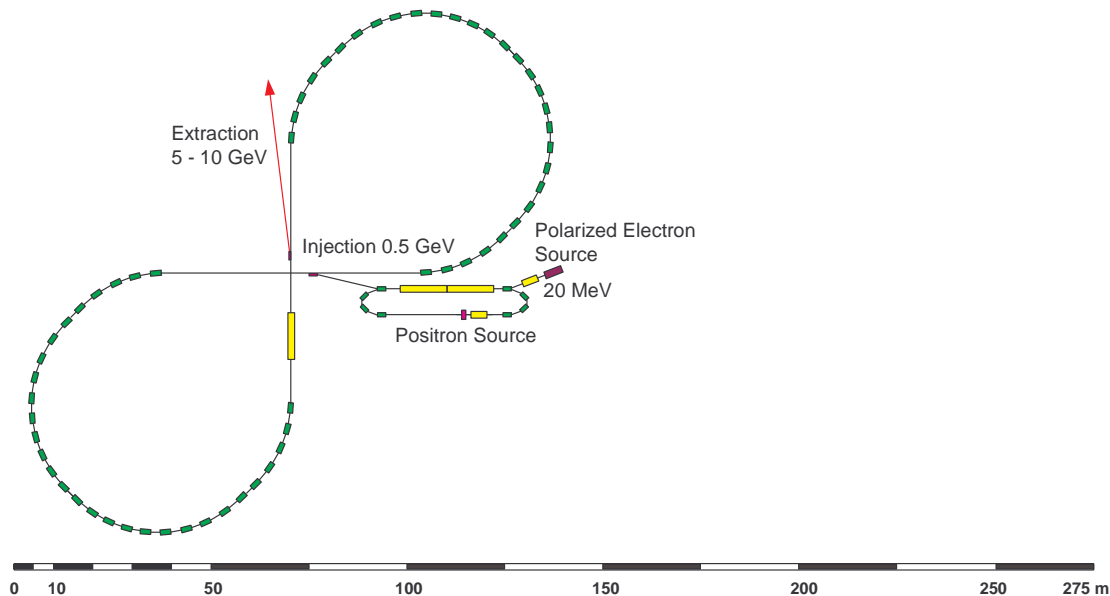


Figure 2.3.2-7. eRHIC injector synchrotron with “figure eight” geometry. A 20 MeV injector and 500 MeV linac fill the synchrotron ring to 0.1-1 mA after which it is ramped in energy from 0.5 to 10 GeV in 10-100 ms.

Due to the small dipole curvature, ~ 30 m, the ring will have a polarization damping time of 40 s at 10 GeV. This should not cause significant depolarization as the beam circulates in the booster for less than 100 ms.

Maximum Energy	10 GeV
Injection Energy	500 MeV
Circumference	500 m
Dipole Curvature	30 m
Synchrotron Radiation Losses/Turn	47 MV @ 10 GeV
Accelerated Current	1 mA
Peak Beam Power @ 10 GeV	50 kW
Installed RF Voltage	75 MV
Installed RF Power	100 kW
Synchrotron Cycling Frequency	<60 Hz
Polarization Damping Time	40 s
Equilibrium Polarization	0

Table 2.3.2-4. Parameters for a possible figure eight synchrotron injector for eRHIC.

If the polarization properties (small depolarization) of the accelerated beam permit a slower ramp it would be desirable to fill the synchrotron with several pulses (~ 10) at its injection energy to a peak current of ~ 1 mA and operate the synchrotron at a lower frequency of 5-10 Hz. The multiple pulse filling could be achieved with either momentum stacking from a 60 Hz 500 MeV copper linac (160 ms) or phase space painting with a superconducting 500 MeV injector linac (20 μ s).

Positrons

The requirement to deliver 10 GeV positrons to the eRHIC ring adds considerable complexity to the eRHIC injector. As illustrated in Figures 2.3.2-1 and 2.3.2-5 our preliminary concept for positron production with either a normal or superconducting linac is accomplished by accelerating electrons through one turn before striking the production target. In the positron acceleration mode the electron transport is indicated in the figures by the red magnets. The subsequent positron transport is then indicated by the green magnets.

The specifications for the positron production target are comparable are less demanding than performance already demonstrated by the Stanford Linear Collider (SLC) positron source. [9] Table 2.3.2-5 lists the parameters for the SLC positron target and for the target for all three of the above injector topologies

	SLC 94	Copper Linac	SC Linac	Figure Eight Synchrotron
Electron Drive Beam				
Energy (GeV)	30	4	3.3	0.5
Pulse Charge (nC)	5.6	2	4	20
Pulse Width (us)	Single Bunch	2	4	2
Repetition Rate (Hz)	120	30	30	60 (Linac freq)
Beam Energy/Pulse (J)	160	8	13	10
Avg. Beam Power (kW)	20	0.24	0.4	1.2
Positron Yield/e-	2.4	~ 0.1	~ 0.1	~ 0.01

Table 2.3.2-5. Positron Production Specification for eRHIC accelerator injector and SLC94 .

For the two recirculating linacs (copper and superconducting) the peak electron current can be increased from 100 μ A to ~ 1 mA to compensate for the lower electron energy striking the production target. This still results in much lower pulse energy and average power than was achieved at the SLC. A positron yield of 0.1 per incident electron could then deliver the same average currents as when the eRHIC injector operates in the electron mode. The 500 MeV linac injector of the figure eight synchrotron could compensate for the lower energy of the electron drive beam by running at macro pulse currents of 10 mA and a slightly higher repetition rate of 60 Hz.

Summary

The design of a 5-10 GeV eRHIC injector accelerator for electrons and positrons is a tractable problem. The three distinct architectures described above may all meet the needs of the eRHIC

physics program. Five important questions that must be addressed to clarify the choice of injector are listed below:

- 1) How will the reliability and operability of each injector affect the performance of the eRHIC program?
- 2) To what degree will the figure eight synchrotron maintain the electron polarization during the synchrotron's acceleration?
- 3) How best can positron production and acceleration be integrated into a superconducting recirculating linac?
- 4) Will this injector serve other functions on the Brookhaven site in addition to e-/e+ injection into eRHIC?
- 5) What are the costs of each injector system?

Future work that will help address these questions includes:

- 1) Development of an operational model for the eRHIC collider complex
- 2) Computer simulation of the polarization behavior in the figure eight synchrotron
- 3) Development of a consistent cost model for each of the considered injectors.
- 4) Detailed integration of positron production and acceleration for each of the considered injectors.

The guiding principle for the eRHIC injector should be to develop an injector which will not limit the physics performance of the eRHIC program and will deliver this performance with the least cost and most reliability.

References:

1. C. Steier et. al., "Acceleration of Polarized Electrons in ELSA" European Particle Accelerator Conference EPAC 98 p.433 1998.
2. H. Huang et. al., "Preserving Polarization through an Intrinsic Depolarizing Resonance with a Partial Snake at the AGS" in AIP proceedings of SPIN 2002 Vol.675, p. 794, 2003.
3. S. Milton, "The APS Booster Synchrotron: Commissioning and Operational Experience" in 16th IEEE Particle Accelerator Conference (PAC 95) Vol. 1 p 594, 1995.
4. <http://www.slac.stanford.edu/accel/pepii/pep2aerial.gif>
5. R. Schmitz, "A CONTROL SYSTEM FOR THE DESY ACCELERATOR CHAINS" in 2nd International Workshop on Personal Computers and Particle Accelerator Controls (PCaPAC 99) Tsukuba, Japan 1999.
6. http://tesla.desy.de/new_pages/TDR_CD/start.html p II-32
7. S. Simrock et. al., "First Demonstration of Microphonic Control of a Superconducting Cavity with a fast Piezoelectric Tuner" in PAC 03, Portland Oregon 2003.
8. Nucl.Phys.A721:1067-1070,2003.
9. Tang et. al., "The NLC Positron Source" <http://ccdb3fs.kek.jp/cgi-bin/img/allpdf?199611228>

2.4 Electron Storage Ring

In this chapter we describe the physics design of the electron ring of the eRHIC collider. The performance goals of the ring are summarized based on the physics requirements outlined in chapter 1.1 and the expected performance of the existing RHIC collider in chapter 1.2. We first discuss the choices of main ring parameters and major technical approaches. Then a preliminary ring lattice design is presented as a baseline design. Following the design section, beam dynamics topics are discussed, including beam collective effects, beam-beam physics, and polarization issues. The RF system is discussed in the final section. The choice of RF parameters and technology has a strong impact on ring performance, technical risk, and cost.

The scope of the eRHIC physics experiments is very broad. First, the extent of center of mass energies that the experiments intend to cover, and then the wide variety of hadron species that will collide with the electron or positron beams require a collider with an unusually wide range of operating parameters. The electron ring is required to have a large energy operation range: 5-10 GeV, and the electron beam emittance is required to change by more than one order of magnitude to maximize luminosities in collisions with various hadron species of different energies. Another major feature of this design is that the electron (or positron) beam must be highly polarized. Section 2.4.6 is devoted to polarization issues. These ring design features are quite different from both the existing e^+e^- colliders PEP II [1] and KEKB [2], and from the existent lepton-hadron collider HERA [3].

The electron ring design as part of the eRHIC project must be site-specific to the existing RHIC facility. RHIC is a well-established ion collider and has a well defined upgrade path. The electron ring will be built in a separate tunnel from the RHIC tunnel, with a different circumference. This gives the electron ring designer the freedom to choose appropriate lattice structure and parameters that are best matched to RHIC, enabling much higher luminosity under all of the many collision scenarios than the existing collider and fixed target facilities can provide. The nominal design luminosity for collisions of 10 GeV electron on 250 GeV protons is 10^{32} - 10^{33} $\text{cm}^{-2}\text{s}^{-1}$.

It is clear that to accommodate all of the physics requirements, tuning flexibility must be embedded in the design from the outset, rather than as a future upgrade. The second design criterion is operational reliability, which has proven to be extremely important in the successful e^+e^- B-factory projects. Reliability means uninterrupted operation and high integrated luminosity. Each of the important technical approaches and choices must be decided within the context of its impact on reliability. A number of straightforward but essential measures are adopted to ensure reliable operation. Two important features are full energy injection of a polarized electron beam, allowing top-off or continuous injection with instant polarization and quick recovery from catastrophic beam loss, and sophisticated closed orbit correction schemes with adequate beam position monitors and correction capacities to insure high equilibrium polarization.

2.4.1 Design Overview

The primary goals for the electron ring design are shown in table 2.4.1-1. These goals must be achieved with adequate beam lifetime and acceptable detector backgrounds. In addition, to maximize

luminosity over the wide range of collision scenarios with different ion species, the normalized emittance must be adjustable by an order of magnitude over the range of design energies.

Peak luminosity for 10 GeV e on 250 GeV p	$10^{32} - 10^{33} \text{ cm}^{-2}\text{s}^{-1}$
Longitudinal polarization	> 70% at IP
Average current	0.45 Amp
Electrons per bunch	10^{11}
Number of electron bunches	120
Energy range	5 – 10 GeV
Polarized positron energy	10 GeV

Table 2.4.1- 1 **Primary goals for electron ring design.**

The key features of the baseline ring design are:

- Flat beam, head on collisions.
- High emittance ratio of the elliptical electron beam at the IP.
- Anti-symmetry solenoidal spin rotators in the IR straight, pure longitudinal spin at 8.5 GeV. 4% reduction at 10 GeV and 20% reduction at 5GeV.
- Flexible FODO arc structure for electron beam emittance adjustment. Wigglers or super-bends to increase synchrotron radiation damping for higher beam-beam tune shift limits at low energy.
- Electron path length adjustments up to 0.2 m.
- Adequate vertical closed orbit correction capacities for high beam equilibrium polarization.
- Full energy, polarized electron beam injector with flexible bunch to bunch filling capacity. Feasible for top-off and continuous injection.
- Reliable high power RF system.
- Low field solenoids around the ring to suppress electron-cloud effect for positron beam.
- Low-photodesorption, low impedance, high radiation power resist vacuum chamber.
- Feed back system for suppressing multi-bunch instability.
- Provisions for longitudinal polarimeter operation in the IR straight.

The electron ring will be located either at the RHIC IP12 or IP4 location, as described in section 2.2. The ring circumference is chosen to be one third of the RHIC ring. This length is an optimum based on balancing the requirements from the length of the interaction region, the arc length and mechanical structures considering the range of electron beam emittance, the synchrotron radiation wall power density, and the beam self polarization time at 10 GeV. The self polarization time at 10 GeV is important because, although the electron beam is generated by a polarized full energy injector, the positron beam still depends on self polarization. Cost optimization is always a major factor in the ring circumference consideration as well. There are still concerns about the possibility that coherent beam-beam effects could compromise the performance of any collider with unequal-circumference rings [4]. This is under active investigation and more discussions on this topic are presented in section 2.4.5.

The e-ring RF frequency must be a harmonic of the colliding frequency which is varied from ~28.15 MHz to ~28.13 MHz depending on the ion beam energies (ion velocity variation). The RHIC RF

frequency (~ 197 MHz) is the 7th harmonic of the colliding frequency. It is not necessary to make the e-ring RF frequency a harmonic of the RHIC RF frequency. Higher RF frequencies are preferred for technical reasons as described in section 2.4.7. It is also not possible to make the ring RF frequency a precise sub-harmonic of the linac frequency (either S-band at 2856 MHz or L-band at 1300 MHz) and the harmonic of the colliding frequency at same time. This adds complication to the timing synchronization of the injector, which must provide a flexible bunch filling pattern to the ring. The timing system synchronizing the beam source to the ring is discussed in the injector section 2.3.

A major technology choice is whether to use room temperature copper RF structures or to adopt superconducting structures, which have made rapid advances in recent years. Both technologies are now mature [5] [6] and proven in user facilities. The cavities in use at SLAC at 476 MHz or the KEKB 508 MHz cavities with modifications are both suitable candidates. Further investigation of the reliability and cost of each system is required before a choice is made.

Figure 2.4.1-1 shows the quasi race-track e-ring layout in a detailed scale. The general layout of eRHIC is presented in chapter 1.

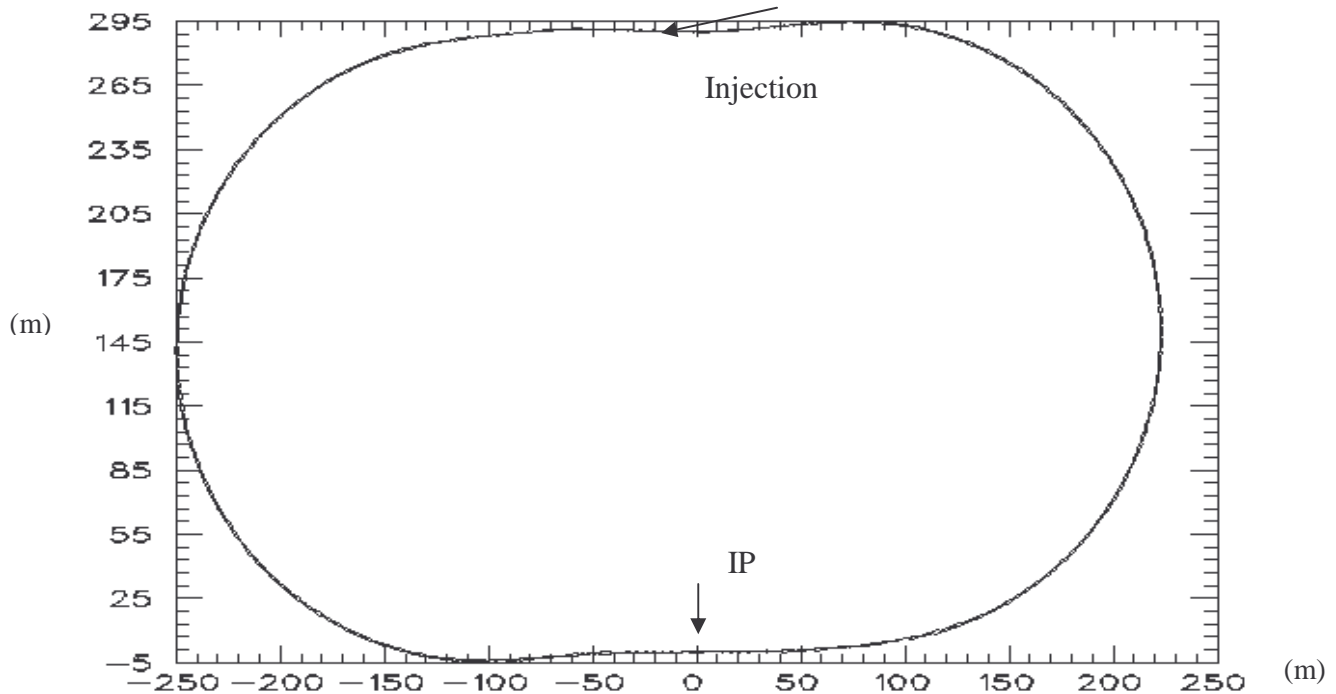


Figure 2.4.1- 1 Electron ring layout

The main ring parameters are listed in Table 2.4.1-2. The nominal parameters are specified for collisions of 10 GeV electrons on 250 GeV protons with the provision of parallel operation of two other hadron beam interaction regions. The goal luminosity is 10^{32} - 10^{33} $\text{cm}^{-2}\text{s}^{-1}$. The proton ring parameters are also listed to give a set of self consistent parameters and appropriate luminosity value. The 10^{33} $\text{cm}^{-2}\text{s}^{-1}$ luminosity is not yet been reached ($\sim 50\%$ less) with the present IP region design and electron beam parameters in the table. Further design considerations for higher luminosity are detailed in section 2.4.2.

		Electron	Proton
Energy E	[GeV]	10	250
Circumference, C	[m]	1277.948	3833.845
Arc dipole radius	[m]	81.02	
$k=\epsilon_y/\epsilon_x$		0.18	1
$K\sigma=\sigma_y/\sigma_x$		0.50	0.50
Nominal emittance(ion) ϵ_n	$[\pi \text{ mm mrad}]$		15.0
Emittancs ϵ_x	[nm.rad]	53.0	9.4
Emittancs ϵ_y	[nm.rad]	9.5	9.4
Beta function at IP x , β_{x^*}	[m]	0.19	1.08
Beta function at IP y , β_{y^*}	[m]	0.27	0.27
Beam-beam parameter x , ξ_x		0.029	0.0065
Beam-beam parameter y , ξ_y		0.08	0.0033
RF frequency (Warm/SC)	[MHz]	478.6/506.7	
RF voltage	[MV]	25	
Bunch length σ_z	[cm]	1.17	
Number of bunches		120	360
Bunch separation	[ns]	35.52	35.52
Particles/bunch		1.00E+11	1.00E+11
Total current	[A]	0.45	0.45
Synch. rad, Loss/turn	[MeV]	10.92	
Linear radiation power density	[kW/m]	9.68	
Damping time (x/s)	[ms]	7.2/3.6	
Luminosity \mathcal{L}	$[\text{cm}^{-2}\text{s}^{-1}]$		4.4E+32

Table 2.4.1- 2 Nominal Machine Parameters

References:

1. “PEP II Conceptual Design Report”, LBL-PUB-5379, SLAC-418, ..., June 1993
2. “KEKB B-Factory Design report”, KEK Report 95-7, 1995
3. U. Schneekloth, (ed) “The Luminosity Upgrade” DESY HERA -98-05, 1998

4. F. Zimmermann, “Summary of Working Group on Interaction Region, Beam-Beam Interaction & Optics”, Workshop e+e- factories 2003, Stanford, CA October 13-16, 2003.
5. T. Furuya, “Update on the performance of Superconducting Cavities in KEKB”, Workshop e+e- Factories 2003, Stanford, CA USA, October 13-16, 2003.
6. P. Corredoura et al. “Experience with the PEP II RF System at High Beam Currents”, p.1891, Proceedings of EPAC 2000, Vienna, Austria.

2.4.2 Luminosity Considerations

The general luminosity expression for a lepton-hadron collider, if the colliding beams are totally overlapped at the interaction point, is:

$$L = \frac{F_c N_i N_e}{4\pi\sigma_x\sigma_y} \quad (2.4.2- 1)$$

Where F_c is the colliding frequency, N_i is the number of ions per bunch, N_e is the number of electrons per bunch, and σ_x and σ_y are the rms transverse beam sizes.

If we assume equal beam-beam tune shift limits for both transverse planes for each of the hadron and lepton beams, then the luminosity expression in terms of linear beam-beam tune shifts can be written as [1]:

$$\begin{aligned} L &= \frac{\pi}{r_e r_i} F_c \gamma_e \gamma_i \xi_i \xi_e \sqrt{\frac{\epsilon_i}{\beta_{i,x}}} \sqrt{\frac{\epsilon_{e,x}}{\beta_{e,x}}} k_e \frac{(1+k)^2}{k^2} \\ &= \frac{\pi}{r_e r_i} F_c \gamma_e \gamma_i \xi_i \xi_e \sigma'_{i,x} \sigma'_{e,x} k_e \frac{(1+k)^2}{k^2} \end{aligned} \quad (2.4.2- 2)$$

Where

- ξ_i or ξ_e is the beam-beam tune shift limit for ion beam or electron beam
- β represents the betatron function at the interaction point
- ϵ is the ion or electron beam geometric emittance
- $k_e = \epsilon_{e,y}/\epsilon_{e,x}$ is the electron beam emittance ratio
- $k = \sigma_y/\sigma_x$ is the beam aspect ratio at IP.
- σ' is the beam angular amplitude.

In the above expression, we also assumed that the smaller beam size is in the vertical (y) direction and $k_e/k \leq 1$, then the dominant linear beam-beam tune shift limits are:

$$\begin{aligned} \xi_{i,x} &= \frac{r_i}{2\pi Z} \frac{N_e}{\gamma_i \epsilon_i} \frac{1}{(1+k)} \\ \xi_{e,y} &= \frac{r_e Z}{2\pi} \frac{N_i}{\gamma_e \epsilon_{e,x}} \frac{1}{k_e (1+1/k)} \end{aligned} \quad (2.4.2- 3)$$

The classical radius r_i of the ion is:

$$r_i = \frac{Z^2}{A} \frac{e^2}{4\pi\epsilon_0} \frac{1}{M_0 c^2} \quad (2.4.2- 4)$$

where Z is the atomic number, A is the atomic mass number, and M_0 is the mass per nucleon. The r_i value for proton is $r_p = 1.53 \times 10^{-18}$ m, for gold $r_{Au} = 49.0 \times 10^{-18}$ m, and $r_e = 2.82 \times 10^{-15}$ m for electrons.

Equation (2.4.2-2) is equivalent to equation (1.1) in section 1.2.3 except writing parameters relevant to luminosity limitations more explicitly, i.e. including the electron beam emittance ratio and electron beam emittance instead of electron beam vertical angular amplitude which does not reach the actual aperture limit in our cases. Our luminosity discussion here will be focused on collisions of 10 GeV electrons on 250 GeV protons, as this is the primary design feature. Other collision scenarios will be discussed accordingly.

Colliding frequency

The colliding frequency is limited by the achievable RHIC bunch number. It comes as a RHIC machine operation and upgrade limit (section 3.2), and it is also raised as a minimum bunch separation requirement from the detector design. The nominal colliding frequency is 28.15 MHz.

Applied to collisions of 10 GeV electrons on 250 GeV protons we have:

$$L = 4.29 \times 10^{43} \xi_i \xi_e \sigma'_{i,x} \sqrt{\frac{\epsilon_{e,x}}{\beta_{e,x}}} \frac{k_e}{4} \frac{(1+k)^2}{k^2} \quad [cm^{-2}s^{-1}]$$

$$\xi_{i,x} = 9.14 \times 10^{-19} \frac{N_e}{\epsilon_i} \frac{1}{(1+k)} \quad (2.4.2- 5)$$

$$\xi_{e,y} = 2.29 \times 10^{-23} \frac{N_i}{\epsilon_{e,x}} \frac{1}{k_e(1+1/k)}$$

Round beam or flat beam collisions and IP magnet aperture limits

Round beam means equal beam sizes in both transverse directions for both lepton and hadron beams, and equal beam emittances in both transverse directions for lepton beam (the ion beams are always supposed to have equal emittances in transverse plans) as well. The luminosity of a round beam compared to a flat beam with the *same beam angular sizes at the IP* is higher due to equal beam-beam tune shift in both transverse plans. From equation 2.4.2-5, compare to flat beam collisions with reasonable beam cross section ratio and lepton beam emittance ratio, say $k_e = 0.1$, $k = 0.5$, the luminosity can be four times higher for round beam collisions. A realistic interaction design in chapter 4 has described a small horizontal angular limit of 93 μ rad for the hadron beam. This means a relatively larger horizontal cross section. To bring the luminosity up, the vertical cross section has to be small. However, the minimum vertical beta function amplitude at IP of the ion beam determined by the ion bunch length sets the lower limit of the beam cross section ratio which is about 0.5 in this design.

The second fundamental problem for round beam collisions comes from electron beam polarization. The electron beam is flat in nature in a storage ring. A round beam can be created by strong coupling between transverse planes or introduction of a vertical synchrotron radiation mechanism to generate vertical beam emittance. As the bending plane is horizontal and the beam spin closed orbit direction is vertical, both methods can end up depolarizing the beam resulting in lower equilibrium polarization [2]. We will concentrate on flat beam collisions in this report.

Electron beam emittance ratio

The lepton beam emittance ratio shown in equations 2.4.2-2 and 2.4.2-3 is an important design parameter that requires further exploration. For flat beam collisions, when beam-beam tune shift limits can be reached for both beams, the luminosity increases linearly with the emittance ratio of the lepton beam. This statement is valid as long as the proton bunch intensity is not a limit (equation 2.4.2-3).

For an accurate evaluation of how luminosity is related to the emittance ratio, we must impose limits from the IR design and minimum β^* values (see following bunch length discussion). We take the e/p, 10 GeV/250 GeV collision as an example. In table 2.4.2-1, the minimum β^* is set to be 0.19m, and the resulting electron beam-beam tune shift limit is 0.08. The IR magnet aperture limits are set from the IR design: $\beta_{i,x}^*=1.08\text{m}$, $\beta_{i,y}^*=0.27\text{m}$, $\epsilon_i=15\text{ nm}$. No proton beam intensity limit is imposed. The electron bunch density is set at 1×10^{11} electrons per bunch.

A significant luminosity gain from very low emittance ratio to the balance point of $k_e=0.25$, where $\beta_{e,x}^*=\beta_{e,y}^*=0.19\text{m}$. Further increase of k_e will require very low electron beam emittance to match the low proton beam emittance and does not help luminosity. The proton beam intensity has to follow up in the sensitive luminosity improvement region ($k_e=0$ to 0.25).

The parameters in table 2.4.2-1 are generated for a special IR design and β^* limit. But we can conclude that luminosity performance is sensitive to lepton beam emittance ratio in a k_e range from very low up to some value (here 0.25) depending on specific IR design (magnet aperture limits) and β^* limits. However to manipulate (increase) electron beam emittance ratio and to maintain high polarization level at the same time can be difficult.

$K_e = \epsilon_{e,y}/\epsilon_{e,x}$	$\epsilon_{e,x}$ (nm.rad)	$\beta_{e,x}^*$ (m)	$\beta_{e,y}^*$ (m)	Protons ($1e^{11}$) per bunch	ξ_x	ξ_y	L $1e32$ ($\text{cm}^{-2}\text{s}^{-1}$)
0.1	54	0.19	0.47	0.57	0.016	0.08	2.5
0.15	54	0.19	0.31	0.85	0.024	0.08	3.8
0.18	54	0.19	0.26	1.0	0.029	0.08	4.5
0.20	54	0.19	0.23	1.13	0.032	0.08	5.0
0.25	54	0.19	0.19	1.41	0.04	0.08	6.3
0.30	45	0.23	0.19	1.41	0.048	0.08	6.3
0.5	27	0.38	0.19	1.41	0.08	0.08	6.3

Table 2.4.2- 1 Lepton beam emittance ratio vs. luminosity

As an example, HERA operation has reached a beam emittance ratio (coupling) of 10% with a beam cross section aspect ratio of 1:4 and electron beam polarization of 60%. They are currently undergoing a luminosity upgrade that aims at achieving 17% coupling with similar beam aspect ratio and ~40% smaller beam cross section. The upgrade is expected to increase luminosity by a factor of 3.5 while maintaining high electron beam polarization. Final results of HERA upgrade are yet to come. Comparing the present design to HERA, the main difference is that the electron beam energy

is $\sim 1/3$ of HERA. The spin resonant strengths are strongly dependent on beam energy, so the challenges at eRHIC should be manageable compared to HERA.

There are ideas [5] and an experimental demonstration [6] of transformation between a round beam and a flat beam using a beam “emittance adaptor”. It is of great interest to have an experimental investigation to see whether this could be applied for a circulating machine. It is especially interesting to establish whether it could work near the IP region where the spin is nearly longitudinal. The goal in this study is to increase the electron beam emittance ratio without depolarizing the beam instead of making a round beam.

Zero crossing angle

Introducing crossing angle can ease beam separation and synchrotron radiation fan problems [3]. A crab cavity would be needed for the hadron beam to avoid luminosity loss [4]. However, the RF voltage of such a crab cavity for the proton beam in this application would be too high, and is technically unrealistic. Therefore, this option is excluded.

Beam-beam tune shift limits

Beam-beam tune shift limits can be reached for both lepton and hadron beams in the eRHIC collider. The lepton beam intensity in particular can be much higher than HERA due to the lower operation energy, and this will drive a higher beam-beam tune shift for the hadron beam.

The beam-beam tune shift limit assumed in this report is 0.0065 for ion beams (per interaction point of three interaction points) and is 0.08 for the lepton beam. They are based on RHIC upgrade parameters [7] and achieved parameters at PEP-II [8]. Even higher lepton beam-beam tune shift limit could be reached if beam loss can be compensated by continuous injection [9]. However, the beam-beam limit for this machine may be different from both the e^+e^- colliding B factories [10] and the ion collisions in RHIC. More discussions are presented in section 2.4.5.

Beam intensity

The nominal design beam current in the electron ring is 0.45 A. The major concern generated by this average current is the linear power density of the synchrotron radiation at 10 GeV. However, this design average current is rather moderate compared to existing B-factories. The number of electrons per bunch, 1×10^{11} , is high compared to other rings. For example, e^+ and e^- per bunch achieved in the PEP II Low (3.1 GeV) and High (9 GeV) Energy Rings are 0.5×10^{11} and 0.8×10^{11} respectively (peak performance, 2.43A and 1.38A, 1317 bunches [8]). The long bunch length and large bunch spacing in the eRHIC e-ring will permit higher limits for bunch charge. The single-bunch charge instability threshold is discussed in section 2.4.4.

The ion beam intensity limits have been defined through RHIC operation. The nominal limit of the number of protons per bunch is $\sim 1 \times 10^{11}$, and is 1×10^9 for Au. Both beam intensities are key adjustable parameters in optimization studies for higher luminosity.

Beam emittance

Electron emittance should be adjusted to match the ion beam for maximum luminosity. However, the electron beam emittance is a parameter of the ring lattice, and is proportional to γ^2 . For example, if the electron beam is run at 5 GeV instead of 10 GeV, then to match the same ion beam the lattice should be adjusted to provide an emittance four times larger than that for 10 GeV. In the present design, the emittance can be varied from ~40 nm to ~360 nm (at 10 GeV). At low energy (5 GeV), an “emittance wiggler” may be needed to further increase the emittance.

The ion beam emittances are well understood through RHIC operation. The normalized proton beam emittance is $\epsilon_{in}=15 \mu\text{m-rad}$. By RHIC convention, the geometrical emittance is $\epsilon_i = \epsilon_{in} / (6\pi(\beta\gamma)_i)$ which is 9.4 nm at 250 GeV. And the normalized Au beam emittance is 6 $\mu\text{m-rad}$ with electron cooling, corresponding to 9.4 nm geometrical emittance at 100GeV/ μ .

Beta function at IP and bunch length

Low β^* means small cross section at IP and higher luminosities. However, the relatively long ion bunch lengths have set limits to minimum β^* values. The constraint is $\beta^* \leq \sigma_z$ in order to avoid reduction of luminosity by the hourglass effect [11]. The minimum proton bunch length in RHIC is ~13 cm, according to the limit of cryogenic power load of 0.5 W/m for 10^{11} protons per bunch. However for 250 GeV proton beam, the bunch length without cooling is about 25 cm. The electron bunch length is only ~2cm, much less than β_e^* at IP, and is not an issue itself. But β_e^* is subjected to the hourglass effect while traveling through the long proton bunch. A low limit of 19 cm for β_e^* is set, corresponding to luminosity reduction of less than 10%. More simulations will be done to evaluate possible lower β_e^* values.

Further Improvement of Luminosity Performance

The luminosity value listed in Table 2.4-1 is $0.44 \cdot 10^{33} \text{ cm}^{-2}\text{s}^{-2}$ for the collisions of 10 GeV electrons on 250 GeV proton. To reach this goal requires upgrades to the existing RHIC collider, and the design of the electron machine may require further development. These are the major topics of this report. Here we discuss further ideas for achieving higher luminosity of $1 \cdot 10^{33} \text{ cm}^{-2}\text{s}^{-2}$ or above with the ring-ring collider option.

From equation (2.4.2-2) and (2.4.2-3), there are several parameters that the luminosity is very sensitive to, including β^* , the emittance ratio, and beam-beam parameters. β^* is limited by ion bunch length. The emittance ratio effect is sensitive within a certain range as discussed above. The actually achievable value of emittance ratio with high beam polarization is not yet clear. The electron beam-beam parameter could be higher if continuous electron beam injection can compensate for higher electron losses due to higher beam-beam tune shift. And the proton beam-beam parameter can be higher if there is only one collision point. However all these sensitive improvements require higher beam intensity.

To make the case for the above arguments, we present two tables similar to our nominal design luminosity and basic parameter tables in section 1.2.3. Table 2.4.2-2 lists two sets of higher luminosity operation parameters for e-p and e-Au collisions at 10 GeV electron beam energy. The main difference between these sets of parameters and the nominal design values are the beam-beam

parameters, and the bunch densities. In table 2.4.2-2, the hadron beam beam-beam parameter is set 1.5 times higher in light of electron-ion collisions only operation scenario. This change requires 1.4 times higher electron beam intensity. Also, the optimization of other parameters and a possible increase of lepton beam beam-beam parameter by 20%, require a similar increase of hadron beam intensity. At this point, from discussions in section 2.4.4 and 3.3, it should be possible to run higher bunch intensities for both electron and ion beams.

A significant challenge to meeting the higher intensity requirements is that they are required in the high electron energy range. The linear radiation power density will be increased to 14 kW/m at 10 GeV for beam current of ~0.65 A. While challenging, the vacuum chamber under such radiation power levels is still technically feasible based on results from R&D for B-factory upgrades.

Energy E	[GeV]	10	250	10	100
$k=\epsilon_y/\epsilon_x$		0.18	1	0.18	1
$K\sigma=\sigma_y/\sigma_x$		0.43	0.43	0.43	0.43
ϵ_n (ion)	[π mm mrad]		15.0		6.0
Emittance ϵ_x	[nm.rad]	54.0	9.4	54.0	9.4
Emittance ϵ_y	[nm.rad]	9.7	9.4	9.7	9.4
β_x^*	[m]	0.19	1.08	0.19	1.08
β_y^*	[m]	0.19	0.2	0.19	0.2
ξ_x		0.042	0.0095	0.033	0.0095
ξ_y		0.1	0.0041	0.08	0.0041
Particles/Bunch		1.40E+11	1.41E+11	1.38E+11	1.43E+09
Luminosity \mathcal{L}	[$\text{cm}^{-2}\text{s}^{-1}$]		1.0E+33		1.0E+31

Table 2.4.2- 2 Parameters for higher luminosity--high electron beam energy.

Table 2.4.2-3 is for low electron energy (5 GeV). The table uses the same higher beam-beam parameters and shorter ion bunch length as applicable. The electron emittance ratio used is slightly higher (0.25) in light of the weaker spin resonance strengths at lower electron beam energy.

The beam intensity requirement for the ion beams are relaxed due to lower electron beam beam-beam parameters in lower electron beam energy operation where less synchrotron radiation and less damping are expected. However, the demand for a higher intensity electron beam remains when the ion beam energy is high. At very low ion beam energy, a much larger electron beam emittance is required to match the proton beam with large geometrical emittance. The very large electron beam emittance will be difficult to produce with normal FODO arc lattice without the help of wigglers or super-bends. The low energy operation will be discussed in the lattice design section.

		Electron	Proton	Electron	Au
Energy E	[GeV]	5	50	5	100
$k=\epsilon_y/\epsilon_x$		0.25	1	0.25	1
$K\sigma=\sigma_y/\sigma_x$		0.50	0.50	0.43	0.43
ϵ_n (ion)	$[\pi \text{ mm mrad}]$		5.0		6.0
Emittance ϵ_x	[nm.rad]	130.0	15.6	56.0	9.4
Emittance ϵ_y	[nm.rad]	32.5	15.6	14.0	9.4
β_x^*	[m]	0.22	1.86	0.18	1.08
β_y^*	[m]	0.22	0.46	0.13	0.2
ξ_x		0.025	0.019	0.029	0.0095
ξ_y		0.050	0.0094	0.050	0.0041
Particles/Bunch		9.74E+10	1.07E+11	1.38E+11	6.42E+08
Luminosity \mathcal{L}	$[\text{cm}^{-2}\text{s}^{-1}]$		1.6E+32		4.5E+30

Table 2.4.2- 3 Parameters for higher luminosity -- low electron beam energy

To summarize, we note that critical steps forward are improvements in IP region design, RHIC upgrades to permit higher ion beam intensity, and shorter bunch lengths to generate higher luminosity. From the electron ring side, higher beam intensity and higher emittance ratio for polarized beams are essential. The immediate task for the electron ring design team is to explore the feasibility of higher beam intensity operation. The goal is 1.4×10^{11} particles/bunch and $\sim 0.65\text{A}$ of average current at 10 GeV. Many of the technical system specifications need to be verified to achieve higher beam intensity operation. An R&D plan to understand and realize higher emittance ratio for highly polarized electron beam is under development.

References:

1. F.Wang “e-ring ZDR progress”, talk at eRHIC collaboration meeting, BNL, August 19-20, 2003.
2. D.P Barber, “Increased vertical e^\pm beam size and polarization ?”, Workshop on the Performance of HERA after Upgrade, Salza, Germany, May 2003.
3. B. Parker, “IP design with warm proton magnets”, talk at eRHIC collaboration meeting, BNL, August 19-20, 2003.
4. K.Oide and K.Yokoya, “The Crab-Crossing Scheme for Storage-ring Colliders”, Phys.Rev.A40:315,1989.
5. Ya. Derbenev, University of Michigan Report No. UM-HE-98-04, 1998
6. D. Edwards et al. “Status of Flat electron Beam Production” p.73, Proceedings of PAC 2001, Chicago, USA. June, 2001.

7. T. Roser, "RHIC STATUS AND PLANS" PAC 2003, Portland , Oregon May 12-16, 2003.
8. J. T. Seeman, "Accelerator Plans at SLAC" e+e- Super-B-Factory Workshop, Hawaii, USA, January 19-22, 2004.
9. U. Wienands et al. "Continuous Injection ("Trickle Charge") at PEP II", Workshop e+e- Factories 2003, Stanford, CA USA, October 13-16, 2003.
10. K. Ohmi, "Beam-beam limit estimated by a quasi-strong-strong simulation", Workshop e+e- Factories 2003, Stanford, CA USA, October 13-16, 2003.
11. G.H. Hoffstaetter et al. "Beam-Beam Limit with Hourglass Effect in HERA", p.401, Proceedings of EPAC 2002, Paris, France.

2.4.3 Lattice Design

The electron ring has a quasi racetrack layout. The anti-symmetrical spin rotator arrangement in the IR straight makes the "straight" section a zigzag line, as is the utility straight on the opposite side of the ring. See Figures 2.4.1-1 and 2.4.3-5.

The lattice design must meet the following criteria:

- Energy range: 5-10 GeV.
- Beam emittance range: ~40-60 nm.rad at 10 GeV, ~50-90 nm.rad at 5GeV.
- Adequate damping rate regarding beam-beam blow up.
- Good dynamic aperture for all lattice configurations.
- High equilibrium polarization ($\geq 70\%$) and longitudinal spin at IP.
- Reasonable self-polarization time at 10 GeV.

Arc Lattice

The two 180° arc sections consist of regular FODO periods with dispersion suppressors at each end. The rationale of choices for each of the basic parameters is discussed below. Figure 2.4.3-1 shows the lattice functions for one arc section.

The dipole bending radius

The design dipole bending radius ρ is ~81m. Synchrotron radiation wall power, electron energy loss per turn and self polarization time at 10 GeV are concerned in choosing the appropriate bending radius.

For constant bend radius, the synchrotron radiation linear power density is

$$P_{linear} (kW / m) \approx 14.085 \frac{E^4 (GeV) I(A)}{\rho^2 (m)} = 9.7 \text{ kW/m} \quad (2.4.3- 1)$$

For nominal stored current of 0.45A, the maximum power density is ~10 kW/m. At this synchrotron radiation (SR) power density level, the technologies for the vacuum chamber are mature [1]. Vacuum chamber technology developed for higher SR power density (~20kW/m) is of interest as we may go for higher stored current. Increasing the bending radius to reduce SR power density is also an option in future lattice design.

The energy loss per turn and total synchrotron radiation power at 10 GeV is

$$P(MW) = U_0 (MeV) * I(A) \approx 0.0885 \frac{E^4 (GeV)}{\rho(m)} (\text{isomag.}) = 10.9(\text{MeV}) * I(A) \quad (2.4.3- 2)$$

Need enough RF gap voltage for beam life time and concern of RF system cost.

A reasonable self polarization time at 10 GeV without use of wigglers is

$$\tau_{POL}(\text{Sokolov - Ternov}) \approx \frac{99R(m)\rho^2(m)}{E^5(\text{GeV})} (\text{sec.}) = 22 \text{ minutes.} \quad (2.4.3- 3)$$

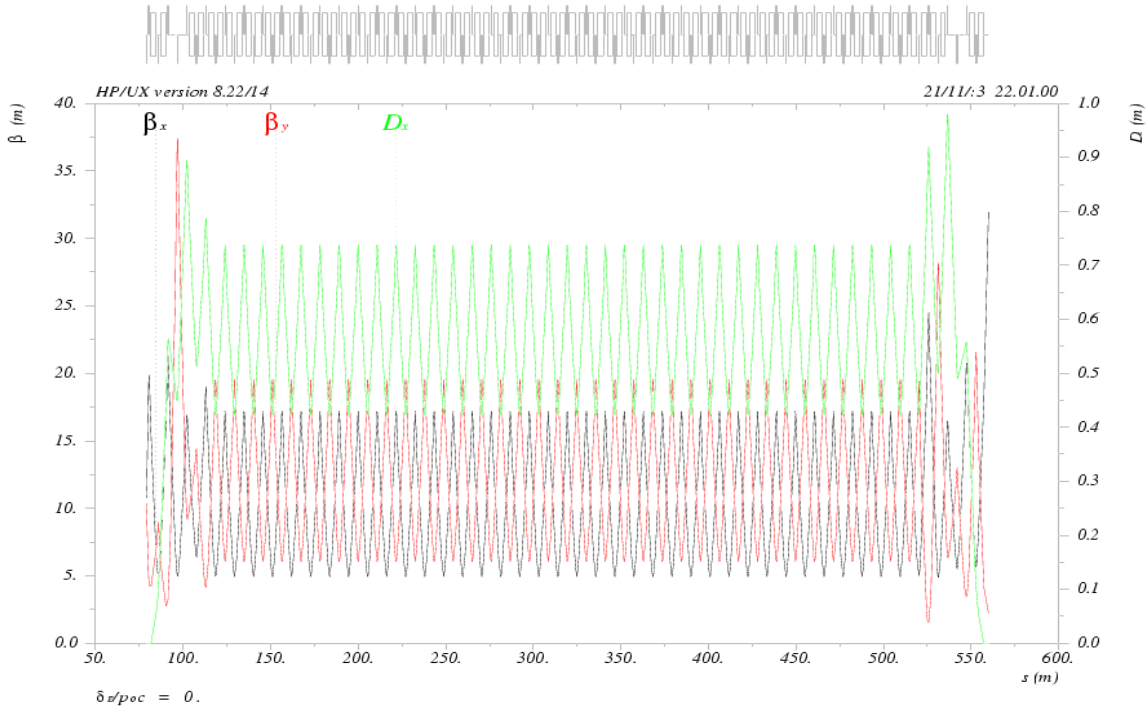


Figure 2.4.3- 1 Layout and optics functions of the arc

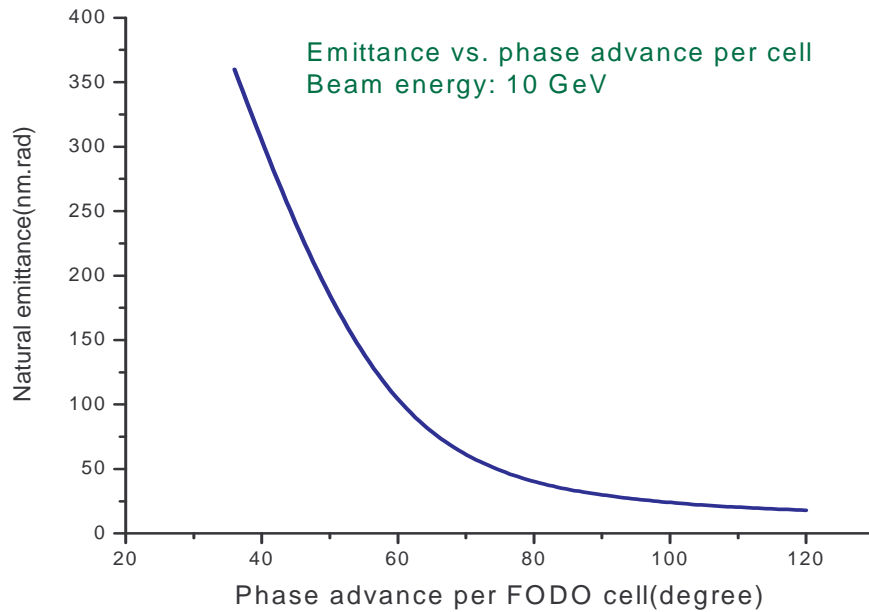


Figure 2.4.3- 2 The natural beam emittance vs. phase advance per FODO cell.

Number of FODO cells and cell length

The number of cells is 84, and cell length is 10.86m. The emittance can be written as [2]:

$$\varepsilon = F(\nu_x, lattice) \frac{E^2 [GeV]}{J_x N_c^3} m.rad \quad (2.4.3- 4)$$

We choose N_c to put the beam's natural emittance in the proper range. The natural emittance vs. phase advance per cell of this design lattice [3] is shown in Figure 2.4.3-2. There should be enough space in a cell for magnets, instrumentation, and vacuum components, and the arc length must fit the ring circumference.

FODO cell betatron phase advance

The horizontal phase shift per cell is used as an emittance adjustment knob. It can be varied from 30 to 80 degrees. The vertical phase shift per cell is somewhat fixed: 60^0 at low and moderate emittances, and $\sim 30^0$ for very large emittance. The fixed phase shift per cell facilitates vertical chromaticity correction sextupole grouping for partial cancellation of second order aberrations from these sextupoles.

Low energy operation with damping wigglers or with super-bends

At 5 GeV the synchrotron damping time is 8 times longer (~ 60 msec.) compared with 10 GeV operation. This has significant impacts on the machine performance, (e.g. the peak and integrated luminosities) since the beam-beam tune shift is limited by intensity dependent beam-beam blow-up. The beam-beam parameter is a function of the damping time [4]:

$$\xi_y^\infty = f[\lambda_d] = f\left[\frac{1}{f_{rev} \cdot \tau \cdot n_{IP}}\right] \quad (2.4.3- 5)$$

where ξ_y^∞ is the beam-beam parameter before beam-beam blow up, τ is the transverse damping time, and n_{IP} is the number of interaction points. From experimental data, it is suggested that

$$\xi_y^\infty \propto \lambda_d^{-0.3-0.4}. \quad (2.4.3- 6)$$

The damping decrement λ_d is proportional to γ^3 in an isomagnetic field ring. For the eRHIC electron ring, the expected beam-beam tune shift limit will be reduced by a factor of 2 as the energy drops from 10GeV to 5 GeV.

The injection rate at 10 GeV can be 50 Hz, but this reduces to ~ 5 Hz at 5 GeV limited by synchrotron radiation damping.

There are two options to increase the synchrotron damping to deal with these problems. One of the options is to install damping wigglers. When wiggler radiation is dominant, the vertical synchrotron damping time is:

$$\tau_y (ms) \approx 10.52 \frac{C[m]}{E[GeV] B_0^2 [T] L_w [m]} \quad (2.4.3- 7)$$

where B_0 is the maximum magnet field in the wiggler, L_w is the wiggler length C is the ring circumference, and E the electron beam energy. For example: asking for τ of ~ 25 ms at 5 GeV will give a beam-beam parameter reduction of 30% instead of 50% from the value at 10 GeV. From equation 2.4.3-7, the damping wiggler will be 25 m in length with peak field of 2 Tesla. With the

wiggler the injection rate should reach 13 Hz. Another benefit of using the wiggler is that it increases the beam emittance at low energy, reducing the required range of phase advance in the FODO cell. This will be important for very large emittance (>100 nm at 5 GeV) when FODO phase adjustment is not enough to increase the emittance. The challenges posed by installation of the wiggler include high synchrotron radiation power, about 700kW in a narrow fan of ~ 100 mrad angle, and other unwanted effects on beam optics such as increased momentum spread. The merits and disadvantages of using damping wigglers for the low energy operation need to be further evaluated. The CESR collider lower energy upgrade is based on using damping wigglers [5]. There are comparable machine and operation scenarios between CESR and eRHIC e-ring low energy operations. Therefore the CESR operation can provide useful design and operation experiences to the decision making of the e-ring damping wiggler option. The damping wigglers can be located in the short straight section in the dispersion suppressor sections that have missing dipoles. Local dispersion there is not zero, leading to a desirable increase in emittance growth from the wigglers. The local Twiss parameters are shown in Figure 2.3.4-3.

Another option is to redesign the ring bending magnet to be like a “super-bend”. The super-bend magnets in the original self-polarizing electron ring design [6] are used to provide short polarization time at low energies. Here the 'radiation' super-bend will be made of three separately powered short bends. The total effective length of these three dipoles is equivalent to the 3m long arc dipole in the nominal machine design. The magnetic field of the center dipole can be 50% higher than the outer ones. At low energy, this allows the outer ones to be turned off and leave the center one on. The bending radius of the short center bend will be 27m. For such a “super-bend” configuration, the total radiation at 5 GeV for 0.5A is 1 MW, three times higher than the 0.34 MW for the nominal design. This radiation power is comparable to the 1.04 MW radiation power of the above described ring with damping wigglers (1.04 MW). The transverse damping time will be 21 ms. The “super-bend” design avoids the complicated wiggler insertions, but has more complicated designs for the arc magnets and vacuum chambers all around the ring. Further comparison of the two options will be based on their effects on optics and beam parameters, technical feasibility, operational flexibility and cost.

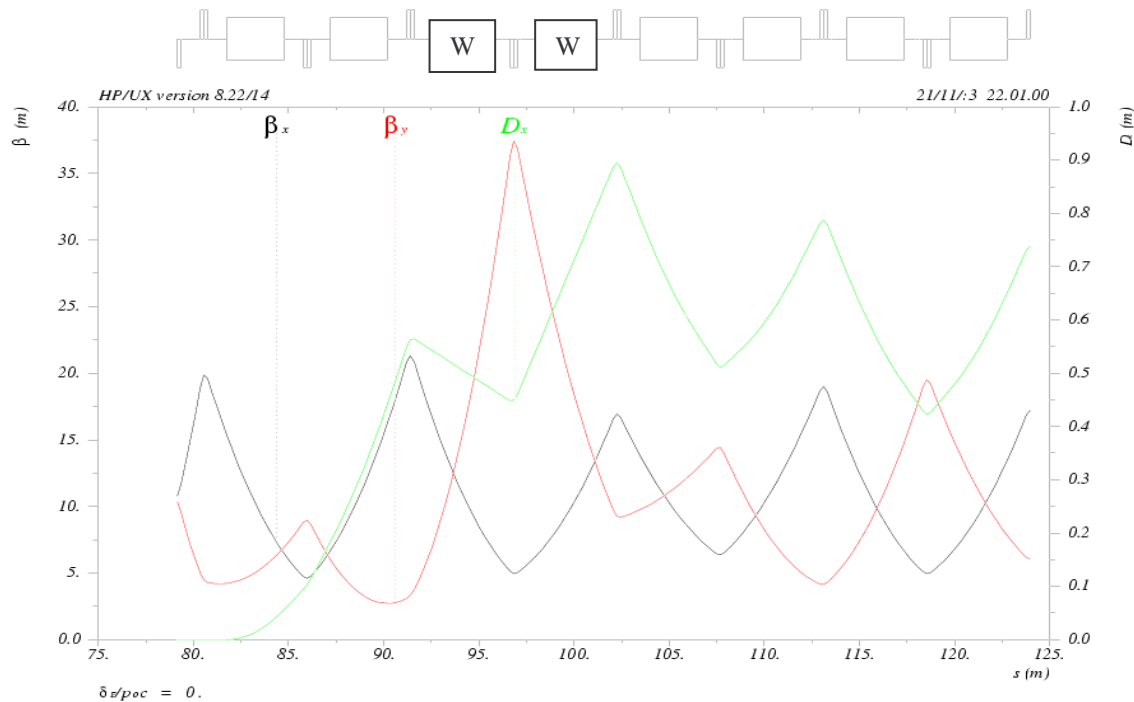


Figure 2.4.3- 3 The dispersion suppressor: arc to IR.

The Interaction Straight

The interaction straight has the most complex optics. The major subsections are the interaction region detailed in Chapter 4, and the antisymmetric solenoid spin rotators described in sections 2.4.6 and 4.4. Figure 2.4.3-4 show the layout of this straight.

The spin is designed to be pure longitudinal at 8.5 GeV. At that energy, the horizontal spin rotation angle is 90 degrees from the end of the solenoid to the IP. The corresponding horizontal orbit bending angle is ~ 4.7 degree. There will be 4% reduction of longitudinal polarization at 10 GeV and 20% reduction at 5GeV. The anti-symmetric horizontal spin rotation bends at either side of the IP consist of six dipoles. Three of them are combined function magnets near the detector which also serve as IP beam separators. A small reverse bend dipole (BRp in figure 2.4.3-6) is arranged to facilitate longitudinal polarimeter installation (actually, only the one downstream of IP exactly serves that purpose). Then two identical dipoles (BR) complete the required rotation.

The lattice optics near the IP has to be adjusted to accommodate various beam sizes (different combination of β^* and beam emittance) required for different collision scenarios. It is important to keep the peak betas at the IR region quadrupoles low to reduce chromaticity to begin with. Another import issue is spin transparency. We leave that discussion to section 2.4-6. Figure 2.4.3-4 shows the IR optics for $\beta^*_{x,y}=0.19/0.27\text{m}$. The maximum β function amplitude is only $\sim 55\text{m}$.

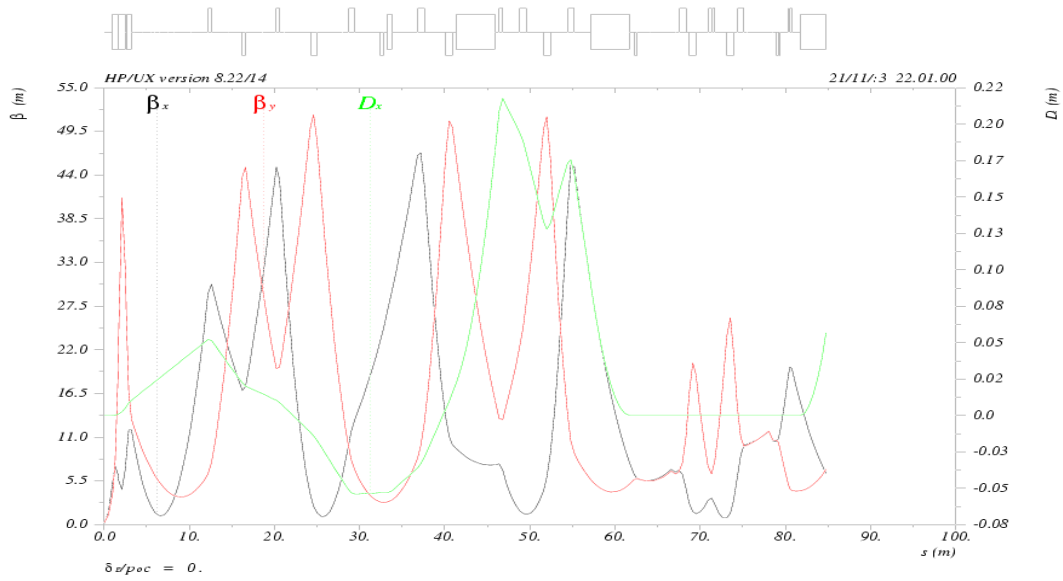


Figure 2.4.3- 4 IR optics with $\beta^*_{x,y} = 0.19, 0.27\text{m}$

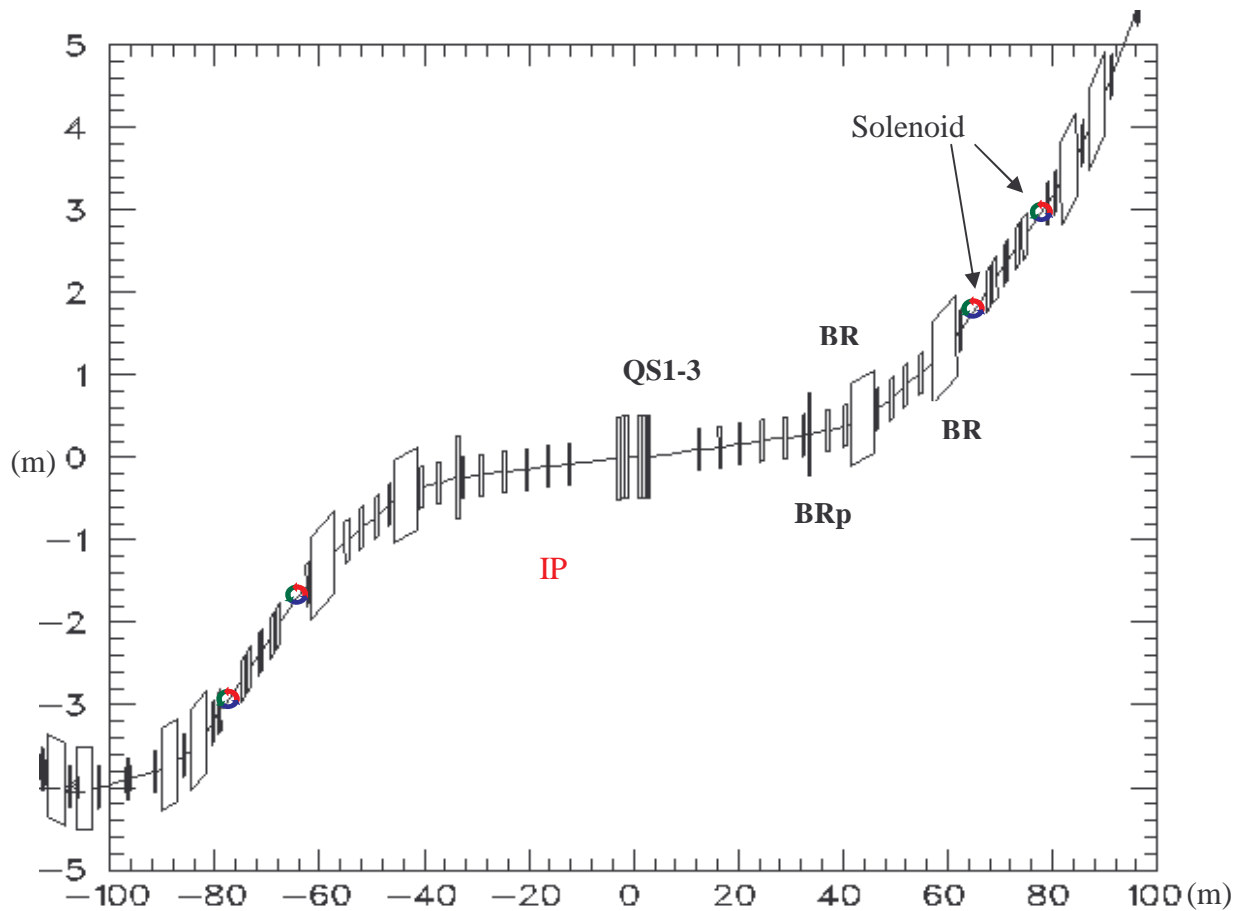


Figure 2.4.3- 5 Interaction straight layout

In Figure 2.4.3-5, the IP coordinate is (0,0). Colored circles indicate solenoid locations of the spin rotators. There are six horizontal spin rotation dipoles on either sides of the IP. They are labeled as

BR, BR, BRp, and QS1-3. QS1-3 are combined function beam separation bends. BRp reverses the deflecting direction. The BRs are normal spin rotation bends.

Compensation of the x-y coupling effects generated by the detector solenoid field is one of the important issues in designing the optics around the IP. The detector is expected to have a maximum solenoid field of 2 Tesla. The plan is to use bucking solenoids to cancel the integrated field around the IP. The merit of using bucking solenoids instead of skew quadrupoles is that this works for particles of any energy, and the bucking solenoids could be placed around the beam pipe inside the detector. Detailed design is still under way.

The Utility Straight

This “straight” has similar zigzag geometry as the IR straight. The injection section is in the middle of the straight. On both sides of the injection section are the two achromats that somewhat resemble the asymmetry layout of the IR region and facilitate ring closure.

The two straight sections connecting the center part of the utility straight to the arcs are used for fractional tune adjustments for ring operation. The optical structure of the two fractional tune adjustment sections are basically FODO cells. The tune adjustment range with the two sections is about 0.1, good for small adjustments in operation.

The RF cavities will be located in these two fractional tune adjustment sections. For example, in the copper RF cavity design option, there will be 28 cavities powered by 14 klystrons. Each two cavity structure has a physical length of ~3.0m. Figure 2.4.3-6 shows half of the utility straight and the RF cavity locations.

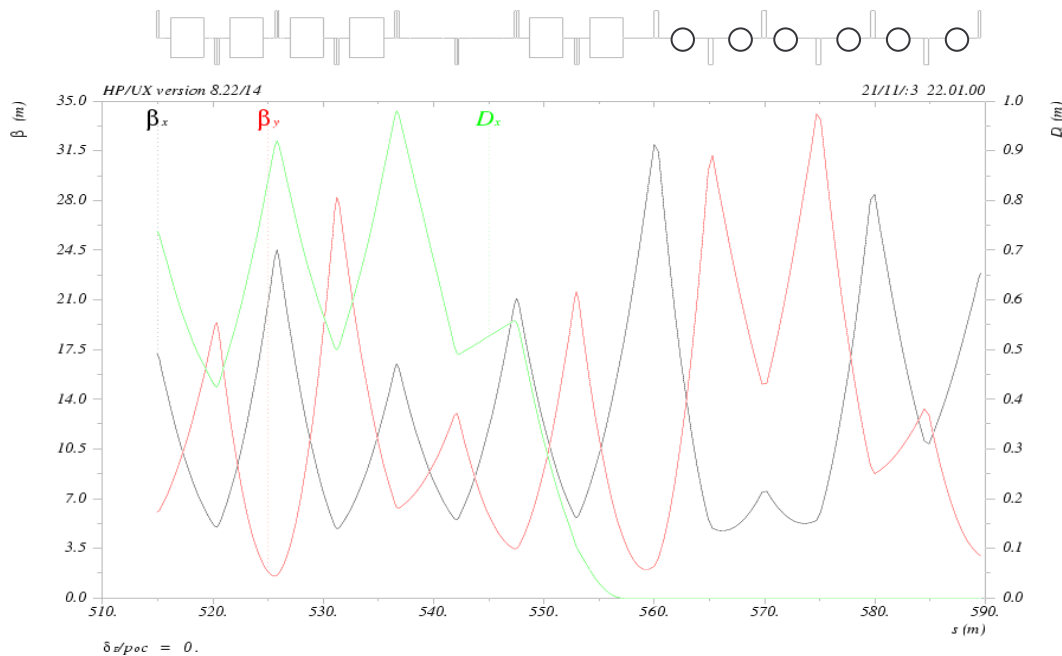


Figure 2.4.3- 6 Optics of the Dispersion suppressor from arc-UT straight and the fractional tune adjustment and RF section. Circles: RF cavity locations.

Electron Beam Path Length Adjustment

Table 2.4.3-1 lists the path length adjustment of the electron ring for matching to different proton beam energies. The required path length change is up to ~0.9 m if the lower end of the proton beam energy is 25 GeV. This length adjustment is large and is difficult to achieve in a conventional way. However if the low end of the proton beam energy is 50 GeV, then the path length adjustment is 0.2m, a much relaxed requirement.

Proton Energy	Proton bunch spacing in time (ns)	Colliding frequency (MHz)	Electron ring RF frequency (MHz)	Electron bunch spacing (m)	Electron beam path length (m)	Electron beam path length changes (m)
25	35.5471	28.1317	478.238	10.6568	1278.812	0.8919
50	35.5283	28.1465	478.491	10.6511	1278.136	0.2161
100	35.5237	28.1503	478.554	10.6497	1277.967	0.0473
250	35.5223	28.1513	478.572	10.6493	1277.920	0.0

Table 2.4.3- 1 Electron beam path length vs. proton beam energy

The conventional means to change path length is with magnetic chicanes in the straights or in the arcs. The most likely scheme is to make chicanes in the arc [7], which saves precious straight sections for other usages. There are technical constraints when making magnet chicanes. The first constraint is the limiting synchrotron radiation power density from a strong bend. The linear radiation power density from a normal dipole is ~10kW/m at 10 GeV with 0.45 A stored current. We require that the power density from a chicane dipole not exceed 20 kW/m, so that the special vacuum chamber technology needed could be obtained from existing B factories. This gives a limit of maximum bending field about 1.4 times of the normal dipole. Other concerns with the chicane are the cost and technical feasibility of a particular design.

Figure 2.4.3-7 shows an eight bend chicane in the arc. It is converted from a normal section of 4 FODO cells. To make the largest path length change with the chicane, the first and the last dipoles are turned off; the lost bending angles will be picked up by the six dipoles in the middle. So the maximum bending field is 4/3 times higher than the normal dipole. Linear radiation power density is about 17kW/m. The first and last dipole can be turned to bend beam in reverse direction to get even larger path length adjustment, but then the middle dipoles will have to bend more strongly and the radiation power density will exceed the limit we have imposed.

Each such chicane can produce a path length difference of 8.25 cm. The path length change can be continuous if precise and reliable mechanical motion control is feasible. Alternatively one can make a fixed change by building another beam line which will be very close to the normal FODO section, in which case the path length change will be discrete. The cost impact and operation reliability issues for the chicane choices have to be further evaluated. The local optics distortion from such a chicane is shown in Figure 2.4.3-8. The overall effect on the ring lattice remains to be examined.

One can activate a number of such chicanes to obtain required path length difference. It seems reasonable to activate four chicanes to get ~20cm path length changes for the 50 GeV proton

collisions. The total length of the moving sections is then about 160 m! And the mechanical motion is complicated. The cost impact will be significant.

However it will be too costly and very destructive to the normal lattice if ten such chicanes (total 80 dipoles, about half of total arc section) have to be activated to make the 0.9 m difference.

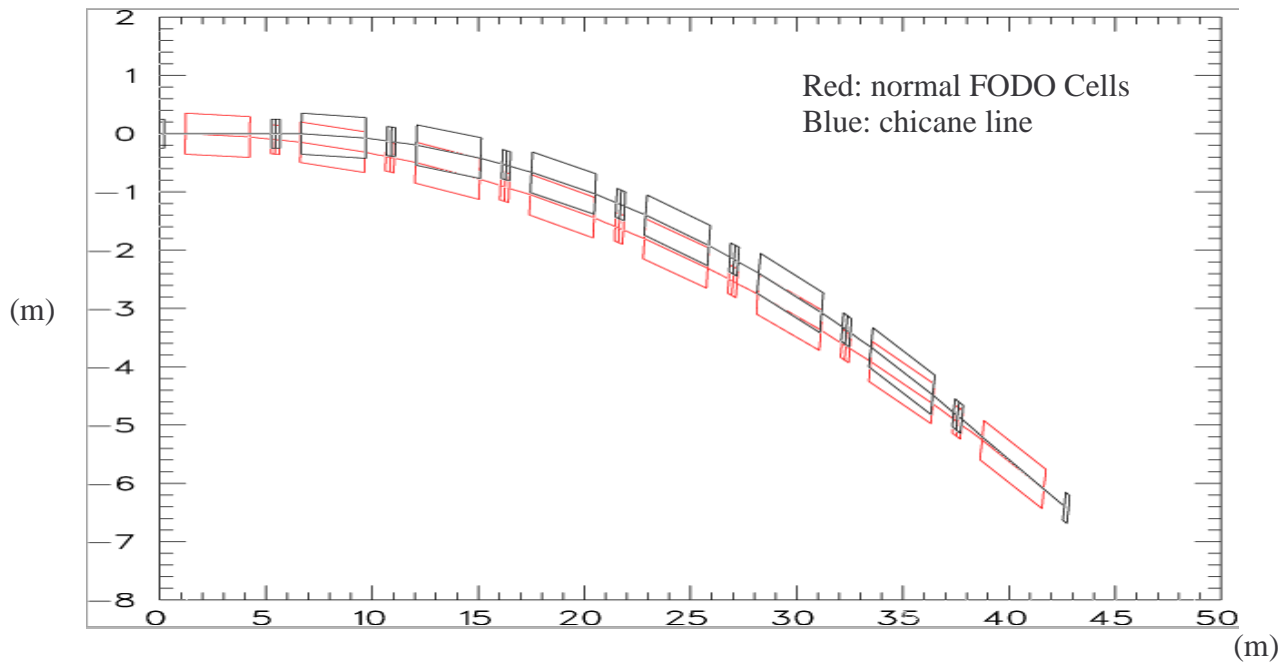


Figure 2.4.3- 7 Layout of an eight bend chicane for path length adjustment.

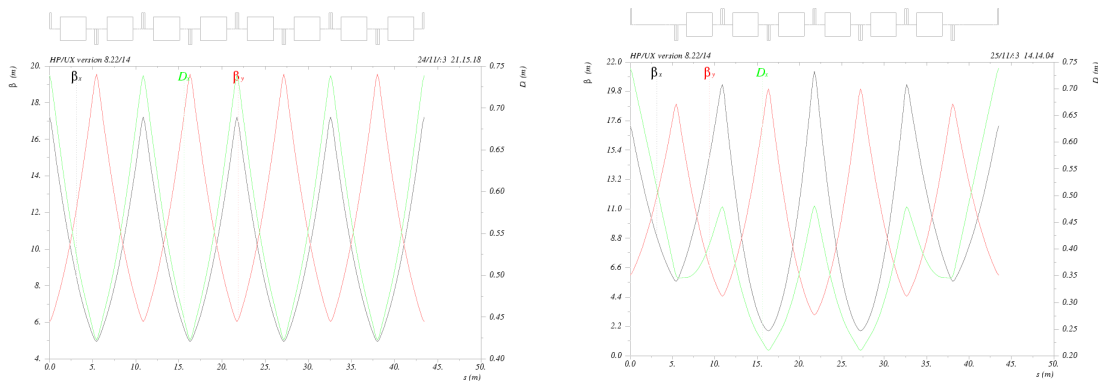


Figure 2.4.3- 8 Optical distortion of the eight bend chicane. Left: the original 4 FODO periods. Right: the chicane optics.

One way to relieve the electron ring path length issue is to adjust the proton ring path length as well [8]. One of the proton rings (YELLOW ring) has to adjust its path length anyway when the BLUE ring is in colliding with electrons while the two proton beams keep colliding at other locations at same time. A comprehensive solution of the path length changes for all the three rings has to be further developed.

For a large path length adjustment scheme, there is not yet an easy solution. One attractive option is to move one of the electron ring arc sections as a whole by 0-0.45m. This option has the advantages of no impact on lattice, no concerns of extra magnets, simple one direction mechanical movement and meets all path length change requirements by one “knob”. The technical details and cost of such a “big move” will be carefully evaluated.

Dynamic Aperture

The criteria of the ring dynamic aperture are set by two requirements: it must be sufficiently large for efficient injection and a long beam lifetime is required under colliding conditions.

Injection takes place in the horizontal plane, so the injection point is horizontally displaced from the closed orbit. For injection, the transverse aperture should include the injection point and several rms beam sizes around it, and the momentum aperture should be at least $\pm 0.5\%$ of the nominal injection energy. For colliding beam, the dynamic aperture should be larger than 10σ for both transverse plans, and the momentum aperture must be at least $\sim \pm 7 \sigma_E$ to guarantee long quantum beam lifetime. An even larger momentum aperture is desirable to tolerate effects other than synchrotron radiation excitation. A larger dynamic aperture is always strongly favored. In this report we will take as the design goal a momentum aperture of $\pm 10 \sigma_E$ and transverse aperture $> \pm 10 \sigma$ with all machines errors and under colliding conditions. The damped beam momentum spread σ_E of the ring is about 1×10^{-3} at 10 GeV and $\sim 0.5 \times 10^{-3}$ at 5 GeV.

The emittance of the full energy injected electron beam is usually smaller than the ring natural emittance. So the $\pm 10\sigma$ transverse aperture requirements are good for injection. However, for the positron beam, the expected emittance at 10 GeV could be as high as 100 nm-rad if no damping ring is included in the positron injector system. More simulation will be performed to see if any significant beam loss could happen and also to investigate the effects on colliding beams in such an operation scenario.

The major cause of reduction of dynamic aperture is the nonlinearity of the sextupole magnets which are introduced to correct chromaticity in the ring. One can expect that a ring with lower chromaticity will need less sextupole strengths and therefore possibly obtain a larger dynamic aperture.

Modern light source rings implement low emittance lattices with strong focusing, and consequently have to deal with strong correction sextupoles that generate high negative chromaticity. Achieving a good dynamic aperture is a major challenge [9]. For collider rings, the arc lattice usually consists of FODO cells with moderate quadrupole focusing and phase shift per cell. Correction of the chromaticity caused by the FODO cell quadrupoles alone will not jeopardize the dynamic aperture. The challenges are to correct the large chromaticity generated by the strong focusing quadrupoles at large β locations near the interaction region.

The ideal way to reduce the nonlinearity by the chromaticity correction sextupole magnets is to use equal strength sextupole pairs that are connected with $-I$ transformers in both transverse plans [10]. This applies to both local corrections around the IP and in the arcs. The noninterleaved 2.5π cell design for the KEKB rings is a good example. The noninterleaved sextupole chromaticity correction scheme is difficult to realize here due to limited space. Also, as mentioned in arc lattice design, the horizontal phase advance has to be widely adjusted to achieve the required beam emittance. At 10 GeV, it varies from ~ 60 - 80 degrees, and can be as low as ~ 30 degrees at 5 GeV. This makes even a conventional interleaved scheme (same phase advance for both transverse planes) not possible. The vertical phase advance per FODO cell has little to do with beam emittance. Smaller vertical phase advance means lower β_y at quadrupoles, and less chromaticity. Therefore, for low and moderate emittance lattices, vertical phase advances are fixed at 60 degrees. Then the sextupoles that are

separated by π phase difference can be paired to partially cancel the second order geometric aberrations.

Repetitive geometric correction is also practiced to cancel second-order geometric aberrations. It requires a lattice made of n identical cells ($n > 3$) having a total phase shift of $2m\pi$ [10]. We have 36 normal FODO cells in each of the 180° arc section. In the vertical plane, three sextupole families are arranged. Then there is a $-I$ transformation for every three FODO cells, and this structure repeats 12 times in an arc section. Horizontal sextupoles will be grouped depending on the phase advance per cell of the specific lattice configuration. Tracking shows that carefully grouping sextupoles according to lattice configurations give much better dynamical apertures than using only two fixed families of sextupoles.

The chromaticity correction scheme in the arc is limited by the large emittance adjustment requirements. However, since we choose the best scheme for the low emittance lattice, the less optimal arrangement for the larger emittance lattice is not necessarily bad for the dynamic aperture because the strengths of the cell quadrupoles are weak for this case, requiring also smaller correction sextupole strengths. For each of the different emittance lattices, the dynamic aperture situation has to be optimized with possible chromaticity correction schemes.

Local chromaticity correction schemes for the IR straight are under development to solve the problem at its source. Due to the different colliding scenarios, the β^* values of the electron beam at IP are required to be varied from 0.19 m to 0.35 m. The local correction scheme has to survive over different IR optics configurations. The space limit in that region also could drive one to consider a scheme like the PEP II High Energy Ring beta-beat scheme for semi-local chromaticity correction [11] which involved a dispersion suppressor and a few arc FODO cells adjacent to the IR straight.

The dynamic aperture is sensitive to working point locations in the betatron tune map to avoid strong resonance lines. The electron ring betatron tunes in e^+e^- colliders are chosen slightly above half-integer for high luminosity based on beam-beam effects [12]. However, in the eRHIC electron ring, the tunes have to be chosen slightly above integer for high polarization. This is because of the absence of parametric resonances $k+1/2$ for the linear spin resonances [13]. The best spin tune is a half-integer spin tune. Therefore the fractional parts of the orbital tunes should be as far away from $1/2$ as is practical to “leave space” around the half integer spin tune. More details are described in section 2.4.6.

The linear lattice is designed using MAD [14]. Chromaticity correction is first optimized with the HARMON module in MAD. High order chromaticities and momentum dependent beta function variations at IP are minimized. Notice that HARMON does not count coupling, so small residual chromaticity exist, and will be further corrected later.

The vertical sextupoles are further divided into six families to facilitate the above process. The horizontal sextupole family number is also doubled. Chromaticity correction results for tune and β^* are plotted in Figure 2.4.3-9.

The initial dynamic apertures are estimated using MAD in the six-dimensional phase space as well. However thick lens tracking in MAD uses maps that are not symplectic by nature, and therefore have to be “symplectified” in order to guarantee energy conservation. This procedure makes them

somewhat unphysical, and makes long-term tracking questionable [15]. We do have concerns about tracking at the edge of apertures with large synchrotron momentum oscillations. The automatic dynamic aperture search DYNAP in MAD could give very sharp drop of apertures at edge for large off-momentum particles. Therefore the dynamic apertures are further evaluated using the two fully symplectic tracking codes LEGO[16] and SAD[17] which show very consistent results when tracking with large synchrotron motions.

Figure 2.4.3-10 and Figure 2.4.3-11 give the dynamic aperture tracking results from both LEGO and SAD. The resulting dynamic apertures are consistent: large momentum aperture of $dp/p = \pm 0.01$.

In all the tracking processes, the horizontal emittance is assumed to be the natural beam emittance and the vertical emittance is half of the natural emittance corresponding to full coupling. We track for 1024 turns, including synchrotron motion and damping. The 1024 turn circulation time corresponds to ~ 0.6 transverse damping time at beam energy of 10 GeV. Longer period tracking of 8096 turns shows very little aperture difference (Figure 2.4.3-10). Therefore, we consider the 1024 turn tracking sufficient to estimate the appropriate dynamic aperture. Dynamic aperture tracking including all magnet errors with proper closed orbit corrections and beam-beam effects are still in progress.

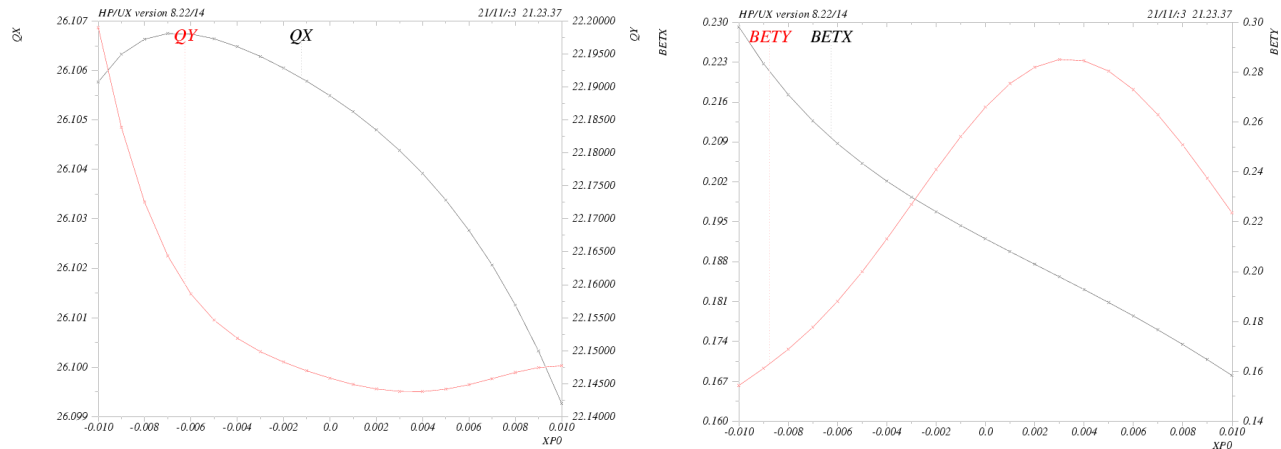


Figure 2.4.3- 9 Chromatic properties of betatron tune and betatron amplitude functions at IP

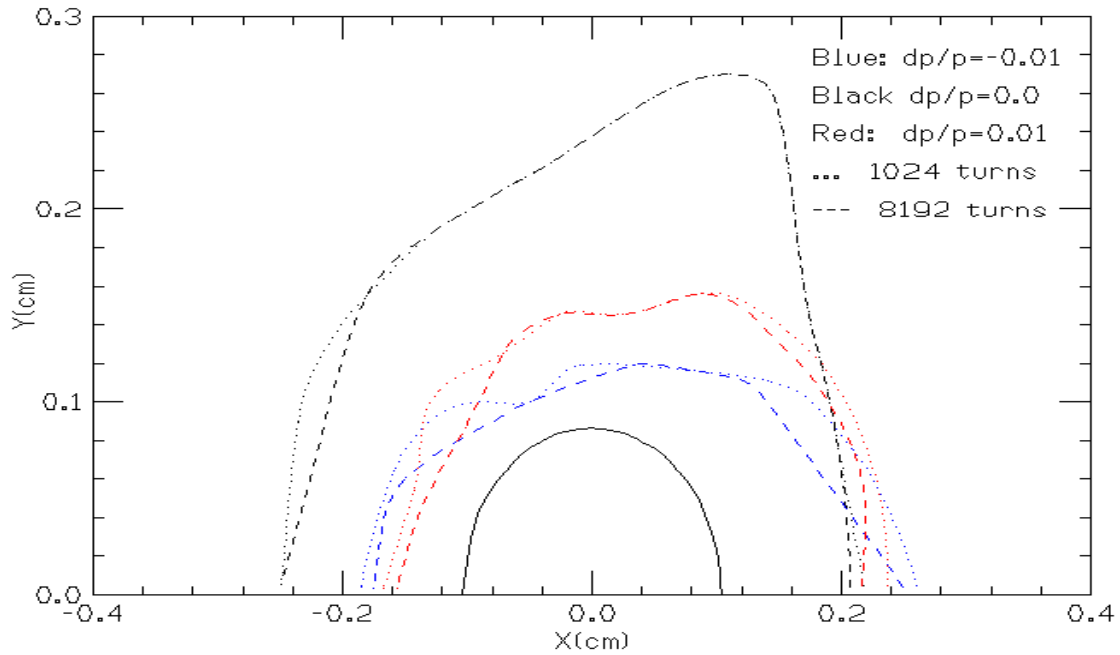


Figure 2.4.3- 10 Dynamic aperture from LEGO tracking. The centered half circle is the 10σ transverse aperture boundary.

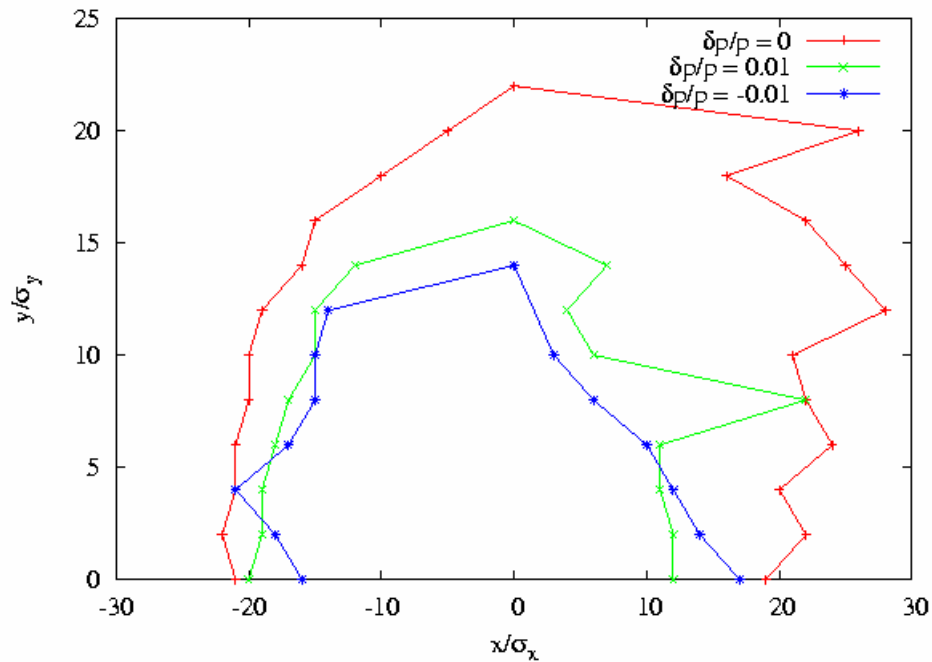


Figure 2.4.3- 11 Dynamic Aperture tracking from SAD

Magnet Errors

Magnet errors include both magnetic field errors and alignment errors. They reduce dynamic apertures, change optics, effect beam polarization and beam lifetime. Table 2.4.3-1 lists typical magnet errors and their effects.

Error	Effect
Dipole Field	Orbit
Dipole Roll	Vertical orbit
Quadrupole Misalignment	Orbit, polarization
Quadrupole Field	Tune, beta and dispersion beat
Quadrupole Roll	Transverse coupling, polarization
Multipole Fields	Nonlinearity

Table 2.4.3- 2 Magnet Errors

The closed orbit errors change particle trajectories through nonlinear elements and will cause detuning. They can reduce dynamic aperture significantly. To obtain small vertical closed orbit distortion is also essential for sustaining high beam polarization (see section 2.4.6). Therefore enough orbit correction magnets and beam monitors with adequate precision should be planned at the design stage. The rms deviation of the closed orbit from the design machine orbit should be 0.1 mm or less. This will greatly reduce the effect of orbit distortion on dynamic aperture. Dynamic aperture will be evaluated under all magnet errors with appropriate orbit correction schemes in place.

While detailed magnet error tolerance study is not the subject of this report. We do track with typical magnet error statistics. In general, tracking with errors to examine their effect on dynamic aperture, luminosity and polarization level will provide the necessary basis for developing various beam-based tuning procedures. Figure 2.4.3-12 shows the dynamic aperture with typical quadrupole and sextupole field errors: 0.1% for quadrupoles and 0.2% for sextupoles.

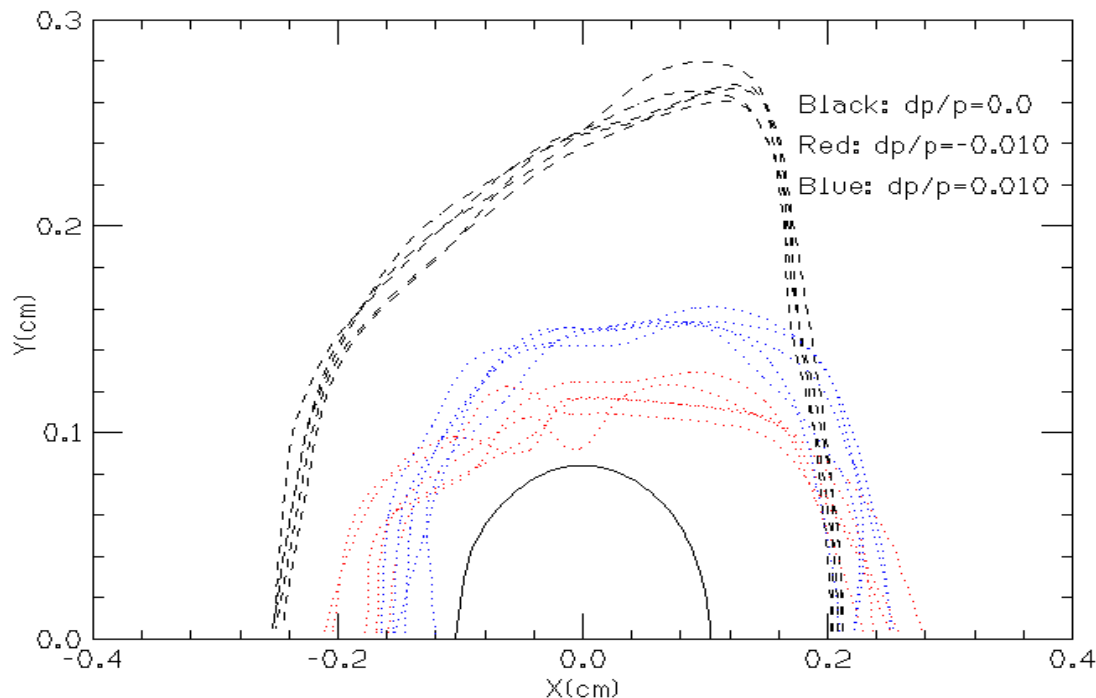


Figure 2.4.3- 12 Dynamic Aperture of lattice ZDR2.0 with multipole field errors.

Machine Parameters

Table 2.4.3- 3 Summary of Machine Design Parameters****

* Beam current at 10 GeV in the table is twice the nominal design value in table 2.4.1-2.

** Path length adjustments are not shown in the table.

ZDR 2.0 2003				
Electron beam energy	10GeV	10GeV	5GeV	5GeV
Ion beam energy	p 250 GeV	Au 100GeV/u	p 50 GeV	Au 100 GeV/u
Circumference(m)	1277.95	1277.95	1277.95	1277.95
Energy (GeV)	10	10	5	5
Bending radius(m)	81.0162	81.0162	81.0162	81.0162
Bunch spacing (ns)	35.52	35.52	35.52	35.52
Bunch spacing(m)	10.65	10.65	10.65	10.65
Number of bunches	120	120	120	120
Bunch population	2.00E+11	2.00E+11	1.00E+11	1.00E+11
Beam current(A)	0.90	0.90	0.45	0.45
Arc cell	FODO	FODO	FODO	FODO
RF frequency MHz	478.572	478.572	478.572	478.572
Harmonic number	2040	2040	2040	2040
Energy loss/turn (MeV)	11.74	11.74	0.72	0.72
Accelarting voltage(MV)	25	25	5	5
Synchrotron tune	0.04	0.04	0.05	0.05
Total rad. power(MW)	10.53	10.53	0.32	0.32
Syn. rad. power/m (KW) in arc	19.25	19.25	0.60	0.60
(from normal bends)				
Self-pola. time at 10GeV(minutes)	22.03	22.03	704.87	704.87
Emittance-x, no coupling (n m.rad)	56.6	56.6	85	54
Beta function at IP (cm) β_y^*/β_x^*	19.2/26.6	19/34	35/20	19/19
Emittance ratio (ϵ_y/ϵ_x)	0.18	0.18	0.45	0.25
Beam size at IP(um) σ_x	104.25	103.70	172.48	101.29
Beam size at IP(um) σ_y	52.06	58.86	87.46	50.65
Momentum compaction α	2.62E-03		9.10E-03	
Momentum spread σ_ϵ	9.61E-04		4.80E-04	
Bunch length (cm) σ_z	1.20	1.20	1.6	1.6
S.R. damping time(x) (mS)	7.3	7.3	58.6	58.6
Beta tune μ_x	26.105			
Beta tune μ_y	22.145			
Natural chromaticity ξ_x/ξ_y	-35.6/-33.8		-28.5/-29.0	

References:

1. Y. Suetsugu et al., "Conceptual Design of Vacuum System for Super KEKB", PAC 2003, Portland, Oregon. May 12-26, 2003.
2. J.B. Murphy "Synchrotron Light Source Data Book", ©1992 American Institute of Physics.
3. D.Wang "Lattice Design of a 10 GeV electron ring for eRHIC", Workshop e+e- Factories 2003, Stanford, CA USA, October 13-16, 2003.
4. R. Assmann and K. Cornelis, "The Beam-Beam Interaction in the Presence of Strong radiation Damping", P.1187, EPAC 2000, Vienna, Austria. June 2000.
5. D. Rice, "CESR-c Status and Accelerator Physics", Workshop e+e- Factories 2003, Stanford, CA USA, October 13-16, 2003.
6. V.Ptitsyn et. al., "Electron-ion collisions at RHIC using a high intensity self-polarizing electron ring", Proceedings of the 2003 Particle Accelerator Conference, p.373, 2003.
7. C. Tschalaer, "Ring path length adjustment", talk at eRHIC collaboration meeting, BNL, August 19-20, 2003
8. B. Weng, S. Peggs, F. Wang, private communications, September-October, 2003.
9. H. Owen et al. "Optimization of the DIAMOND Storage Ring Lattice", p.751, Proceedings of EPAC 2002, Paris, France.
10. K.L. Brown and R.V. Servranckx, "First- and Second-order Charged Particle Optics", SLAC-PUB-3381, July 1984.
11. M.H.R. Donald et al. "Lattice Design for the High Energy Ring of the SLAC B-Facility (PEP-II)", p.576 proceedings of PAC 95, Dallas, TX 1995.
12. Y. Cai and Y. Nosochkov "Tracking Simulations Near Half-Integer Resonance at PEP-II", SLAC-PUB-9812, May 2003.
13. J. Buon, "Polarization of Electron and Proton Beams", CERN 95-06 , 1995.
14. H. Grote, F. C.Iselin, "The MAD Program (Methodical Accelerator Design)" CERN/SL/90-13.
15. Hans Grote and J. Cardona, Private Communication, Aug. 7, 2003.
16. Y. Cai, "LEGO -- A Class Library for Accelerator Design and Simulation" , SLAC-PUB-8011, November 1998.
17. K. Hirata, "An introduction to SAD", Second Advanced ICFA Beam Dynamics Workshop, CERN 88-04 (1988). See <http://acc-physics.kek.jp/SAD/sad.html>.

2.4.4 Beam Instabilities

In previous chapters we discussed the parameter choices of eRHIC. The lattice design of the electron ring presented in 2.4.3 is based on these choices. In this chapter the influence of the various intensity-dependent effects on the machine performance is investigated.

The main parameters of electron ring of the eRHIC are

- Beam energy: 5 -10 GeV
- Particle species: electron and positron
- Beam currents: ~450 mA
- Bunch length: ~ a few cm
- Beam emittance: ~ 50 to 100 nm.rad
- Beam energy spread: 6~10 E-4
- Bunch spacing: ~10.6 m
- Particles/bunch: $\sim 1 \times 10^{11}$

In the current eRHIC design, the bunch spacing is primarily determined by the existing hadron machine complex. There is little flexibility for generating different bunch patterns. One has to deal with a high bunch current and a relatively high total beam current. Since the bunch length of the hadron beams is longer than 10 cm, the bunch length of lepton beams (1-2cm is expected) is not an issue. The main concern for single bunch effect is the transverse mode-coupling instability. We also discuss the power deposition generated by a beam in the form of the higher order mode (HOM) losses by interacting with its surroundings. The narrow-band impedance and related instabilities need to be evaluated carefully due to the relatively large number of RF cavities. The eRHIC machine is planned to operate over a wide range of beam energies. Many collective effects exhibit their strongest behavior at low energy where the beam is less rigid and damping time is much longer than at higher energies. Since electron and positron beams are required by the physics programs, the lepton machine has to account for both electron cloud effects (ECE) for positron operation, and fast beam-ion instability (FBII) for electron operation in the ring design.

Compared to the achieved beam performance in several new machines at the same energy ranges, especially two B-factories, the requirements for eRHIC electron ring appear reasonable and achievable.

In terms of collective effects, several issues are of particular concern including:

- Single bunch instabilities
- Higher-order-mode (HOM) heating
- Coupled bunch instabilities
- Ion related effects
- Electron cloud effects, etc.

The major parameters of eRHIC and other existing machines in the same energy range are summarized in the Table 2.4.4-1.

	eRHIC	PEP-II LER/HER	KEKB LER/HER	CESR-III
Energy(GeV)	5 - 10	3.1/9.0	3.5/8.0	5.3
Circumference(m)	1278	2200	3016	776
RF freq.(MHz)	478.6 or 506.6	476	508	500
RF voltage(MV)	5 - 25	6/15	10/18	3
Total current(A)	0.45	2.4/1.4	1.9/1.2	0.72
Particle/bunch(10^{11})	1.0	1.0/0.6	1.1/0.7	1.3
Bunch spacing(m)	10.6	1.9	2.4	2.4(in train)
Momentum comp.	0.009/0.0026	0.0018	0.0012	0.0025
Energy loss/turn(MeV)	0.72/11.7	1.2/3.6	1.6/3.5	1.0
Average beta(m)	~15	~17	~10	~20
Bunch length(cm)	1~2	1.0	0.4	1.5

Table 2.4.4- 1 Comparison of beam parameters of eRHIC and major existing lepton rings in the same energy **range**

Impedance Budget

We start with the estimate of impedance contributions from various components in the eRHIC lepton ring. Among the impedance-generating elements in the ring, the largest contributors are RF cavities, the resistive vacuum chamber walls, the IR chambers, bellows and masks.

RF cavities

The main contribution to the narrow-band impedance comes from the RF cavities. To substantially reduce the narrow-band impedance a small number of deeply-damped RF cavities will be adopted. At the current design stage, the PEP-II 476 MHz normal conducting RF cavities and KEKB superconducting cavities are both highly successful for operation of high current B-factory storage rings. These two cavity designs are the major candidates for the eRHIC electron ring. The superconducting cavities are especially attractive because their higher accelerating voltage reduces the total number of cavities needed, thus reducing their impedance contribution. Brookhaven also has a long history in superconducting technology, and has recently been developing a facility to test superconducting RF cavities. To compensate energy loss due to synchrotron radiation and keep a reasonable quantum lifetime, a total RF voltage of about 18 MV is needed at 10 GeV. It is assumed that the RF system should be able to provide up to 25 MV total RF voltage. Figure 2.4.4- 1 and Figure 2.4.4- 2 show the bunch length with different beam energies. Over major operating ranges the bunch length would be 1-1.5 cm.

Resistive-wall

Detailed designs of vacuum chamber and components are not yet available, but we can discuss design principles and outline an impedance budget. A vacuum chamber with about 3.5 cm radius, which is comparable to similar machines, is assumed in our current calculations. Copper is the material of choice for its excellent conducting properties. For comparison, aluminum and stainless steel are also simulated.

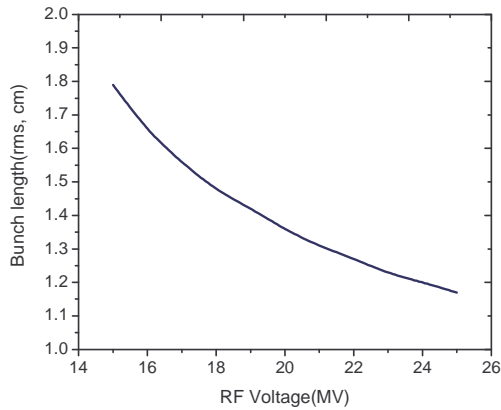


Figure 2.4.4- 1 Bunch length at 10 GeV

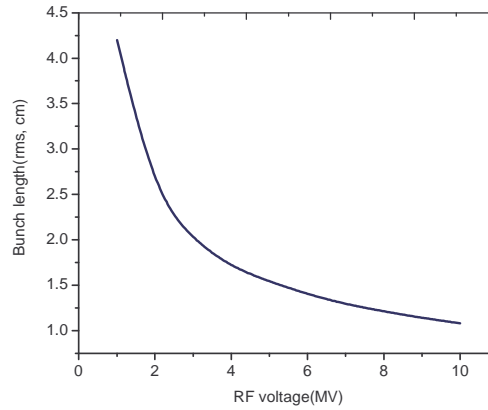


Figure 2.4.4- 2 Bunch length at 5 GeV

Other components

- Pumping slots
- BPMs
- Masks
- IR chambers(including two Y-shape recombination chambers)
- Bellows
- Tapers, etc.

Preliminary estimates of the quantities of each component and the budget of their contribution to the inductive impedance and loss factor (assuming 1 cm bunch length) are shown in Table 2.4.4-2.

component	No. of items (estimated)	Inductive impedance(ohm)	Loss factor budget(V/pC)
Cavities	28(n.c.)/13(s.c.)		~14/10
Resistive wall	1278 m	2e-3	2.0
Masks	TBD	3e-2	2.0
Valves	TBD	6e-3	0.3
BPMs	~300	1e-4	0.6
IR chambers	1+2	2e-3	2.0
Tapers	TBD	2e-2	2.0
Bellows	TBD	1e-2	2.0
Total		~0.06	~25/21

Table 2.4.4- 2 Impedance and loss factor budgets

Based upon above budget the total loss factor with some contingency is ~25 V/pC, which is comparable to that for KEKB [1] and PEP-II [3]. A very conservative estimate for total impedance, 1 ohm, is used for the instability simulations. These should be considered a very preliminary study because number of items is a rough estimate and some of the components, such as feedback pickups, injection kickers, some chamber tapers connecting various components and so on, are not among the listed items. Inclusion of all the detailed beamline components may change these calculations in some extent. For these reasons, a wide range of loss factor and impedance values are considered in calculating the impedance-related collective effects.

Higher Order Mode (HOM) Heating

The estimated total higher-order-mode power of the electron ring is up to about 240 kW with 450 mA current. Compare to that of B-factories the HOM power in eRHIC e-ring is moderate. In case of high intensity operation with 1 A beam current the HOM energy loss would approach to the level of B-factories.

Loss factor(V/pC)	15	25	35
I = 450 mA	120 kW	200 kW	280 kW
I = 1000 mA	590 kW	980 kW	1370 kW

Table 2.4.4- 3 HOM power with different loss factor and beam current

Transverse Mode Coupling Instability (TMCI)

This instability occurs when two head-tail modes ($m=0$ and $m=-1$ in most cases) share the same coherent frequencies. The instability is a severe limitation on the single bunch current in large storage rings with a low beam energy and a low synchrotron tune. Using the estimated transverse wake potential and average beta function of 15 m, it is found that coherent tune shift of the $m=0$ dipole mode is very small at the design bunch current. The transverse mode-coupling instability threshold is expected to scale as

$$I_b = \frac{4(E/e)v_s}{\langle \text{Im}(Z_{\perp})\beta_{\perp} \rangle R} \frac{4\sqrt{\pi}}{3} \sigma_l \quad (2.4.4-1)$$

where v_s is the synchrotron tune, β is the beta function at the location of the impedance, and R is the average ring radius. Compared to the B-factory low energy rings, the eRHIC collider has higher energy, higher synchrotron tune, longer bunch length, shorter circumference, and comparable impedance and beta function. The calculated threshold currents are about 46 mA at 10 GeV and 16 mA, respectively, which are higher than the nominal value (3.8 mA) with comfortable margins. For all of these reasons the transverse mode-coupling instability threshold will not impose a threat to the performance of the lepton ring.

Longitudinal Microwave Instability Threshold

Although not a source of beam loss or intensity limitation, the longitudinal microwave instability together with the potential well effect is considered to be the major source of bunch lengthening. The design beta-functions at IP of the lepton beam are about 15 to 30 cm. Since the bunch length of hadron beams is very long (above, say, 10 cm or longer) the much shorter bunch length of lepton beams (1~2cm is expected) is not considered to be a problem (hourglass effect is negligible). Figure 2.4.4-3 shows the threshold of the longitudinal microwave instability [6].

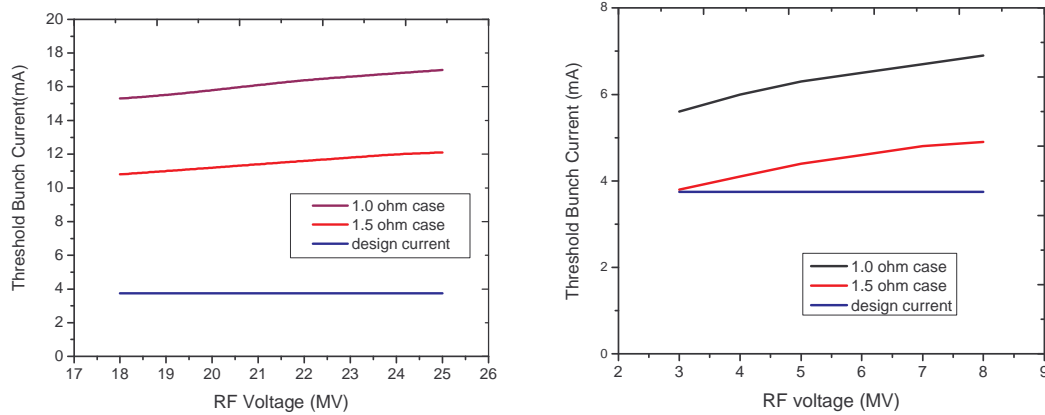


Figure 2.4.4- 3, 4: Single bunch threshold at 10 GeV (left) and 5 GeV (right) with different broadband impedance scaling.

Longitudinal Coupled Bunch Instability

The wake fields in high-Q structures in a storage ring, such as RF cavities and resistive-wall beam pipes, cause different beam bunches to interact. For certain values of relative phase between bunches, the coupled-bunch motion can grow and become unstable, leading to beam loss. The instabilities are characterized by their motion in longitudinal phase space. Longitudinally, the $a=0$ mode can not become unstable, so the lowest longitudinal instabilities are characterized by $a=1$ synchrotron motion. Table 2.4.4-3 and 2.4.4-4 summarize the major monopole modes for these two kinds of RF cavities.[2][4]

f(MHz)	R/Q(ohms)	Q
758	44.6	28
1009	0.006	246
1283	7.68	66
1295	6.57	907
1595	5.06	178
1710	0.44	54
1820	0.13	0.0
2109	3.52	233
2253	1.21	500

Table 2.4.4- 4 Major monopole modes of PEP-II RF cavity

f(MHz)	R/Q(ohm)	Q
783.0	0.12	132
834.0	0.34	72
1018.0	6.6	106
1027.0	6.4	95
1064.9	1.6	76
1076.0	3.2	65
1134.0	1.7	54

Table 2.4.4- 5 Major monopole modes in KEKB sc RF cavity

Mode	Growth time (ms)
a=1	$\tau_1 = 228$ $\tau_2 = 229$ $\tau_3 = 230$
a=2	$\tau_1 = 2139$ $\tau_2 = 2148$ $\tau_3 = 2153$

Table 2.4.4- 6 Growth rates: longitudinal, at 5 GeV

Calculations are performed using the ZAP code [6] with the cavity characteristics given above. Table 2.4.4-5 shows the modes with the fastest growth rates in 5 GeV operations. The growth times are longer in 10 GeV case.

Transverse Coupled Bunch Instability

Tables 2.4.4-6 and 2.4.4-7 summarize the major dipole modes for these two kinds of RF cavities [2][4]. In the transverse plane, the a=0 motion is the lowest mode of instability. Table 2.4.4-7 gives the a=0 and a=1 modes with the fast growth rates for eRHIC electron ring. Again they occur when beam energy is low (5GeV). The situation at higher energy is better.

f(MHz)	R_{tran} (k ohm/m)	Q
792	9.7	96
1063	50.4	34
1133	1.3	0
1202	0.6	642
1327	5.6	510
1420	5.3	554

Table 2.4.4- 7 Transverse modes in PEP-II 476 MHz cavity

(MHz)	R/Q' (ohm/m)	Q
609.0	1.9	92
648.0	40.2	120
688.0	170.4	145
705.0	227.3	94
825.0	6.2	60
888.0	3.5	97

Table 2.4.4- 8 Transverse modes in KEKB sc RF cavity

Note: different units/conventions in transverse modes of two cavities.

Mode	Growth time (ms)
a=0	$\tau_1 = 38$ $\tau_2 = 55$ $\tau_3 = 67$
a=1	$\tau_1 = 164$ $\tau_2 = 165$ $\tau_3 = 166$

Table 2.4.4- 9 Growth rate of transverse modes

The damping times in the electron ring are about 7.4 ms (transverse) and 3.7 ms (longitudinal) at 10 GeV and 58 ms (transverse) and 29 ms (longitudinal) at 5 GeV. The worst situation occurs in the low energy operation, where the coupled-bunch instabilities have the fastest growth rates and damping time is long. The preliminary simulations suggest that a feedback system is needed and sufficient.

Fast Beam-Ion Instabilities (FBII)

The relatively large bunch spacing in the eRHIC electron ring causes a small ion trapping effect. However, the ions accumulated during a single passage of the bunch can cause a transient instability. This so-called ‘fast beam-ion instability’ (FBII) is similar to the multi-bunch beam break-up in a linac. Usually the FBII is more severe in the vertical plane as the vertical emittance is smaller in the lepton machine. According to the linear model [5], the rise time can be described as

$$\frac{1}{\tau} = \frac{4d_{gas} \sigma_{ion} \beta_y N_b^{3/2} n_b^2 r_e r_p^{1/2} L_{sep}^{1/2} c}{3\sqrt{3} \sigma_y^{3/2} \gamma (\sigma_x + \sigma_y)^{3/2} A^{1/2}} \quad (2.4.4-2)$$

where $d_{gas} = p/k_b T = 5.1E13 \text{ m}^{-3}$ is the density of residual gas, σ_{ion} is the ionization cross section, N_b is the particle number per bunch, r_e and r_p are the classical radius of the electron and proton respectively, L_{sep} is the bunch spacing, σ_x and σ_y are the horizontal and vertical beam sizes, and A is the ion mass in unit of proton mass.

	B-factory parameters	eRHIC scaling factor over B-F parameters
N_b	$\sim 1E11$	~ 1
L_{sep}	$\sim 2.5 \text{ m}$	~ 4
σ_x	$\sim 0.8 \text{ mm}$	~ 1
σ_y	$\sim 0.12 \text{ mm}$	~ 3
E	$\sim 9 \text{ GeV}$	$\sim 0.5 \sim 1.2$

Table 2.4.4- 10 Scaling FBII effects in electron ring of eRHIC

Above table shows that the eRHIC lepton ring has some advantages over today’s B-factories on FBII. Below is a more detailed analysis.

Taking into account of the coherent frequency spread, the linear theory gives the couple bunch motion in the bunch train like $y \sim \exp(t/\tau_e)$, the growth time is given by

$$\frac{1}{\tau_e} = \frac{1}{\tau} \frac{c}{2\sqrt{2}l_{\text{train}}(\Delta\tilde{\omega}_i)_{\text{rms}}} \quad (2.4.4-3)$$

where $(\Delta\tilde{\omega}_i)_{\text{rms}}$ is rms spread of ion coherent angular frequency, l_{train} is bunch train length.

$$\omega_i = \left(\frac{4N_b r_p c^2}{3AL_{\text{sep}} \sigma_y (\sigma_x + \sigma_y)} \right)^{1/2} \quad (2.4.4-4)$$

The growth rates of FBII at 10 GeV and 5 GeV are shown in Figure 2.4.4-5 and 6.

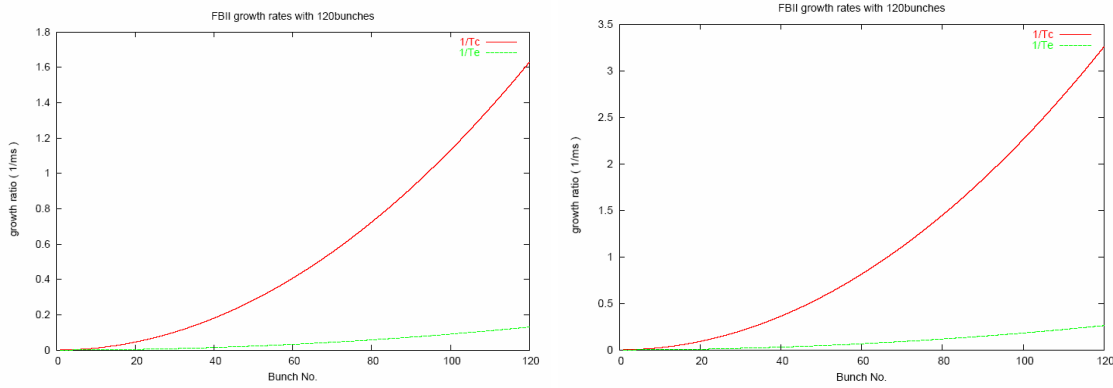


Figure 2.4.4- 2, 6: Growth rates of FBII at 10 GeV (left) and 5 GeV (right), 450 mA

If a total beam current of 1000 mA is assumed, compared to the achieved parameters of the two high energy rings at the B-factories the bunch population of the electron ring of eRHIC would be higher by a factor 2. However, its vertical beam size is larger (for matching the hadron beam size), which improves the situation. We expect the FBII effect with 1000 mA current in the electron ring of the eRHIC collider to be comparable with that in two B-factories. See Figure 2.4.4-7 and Figure 2.4.4-8. A feedback system like those used at PEP-II and KEKB should be able to handle the required beam intensity.

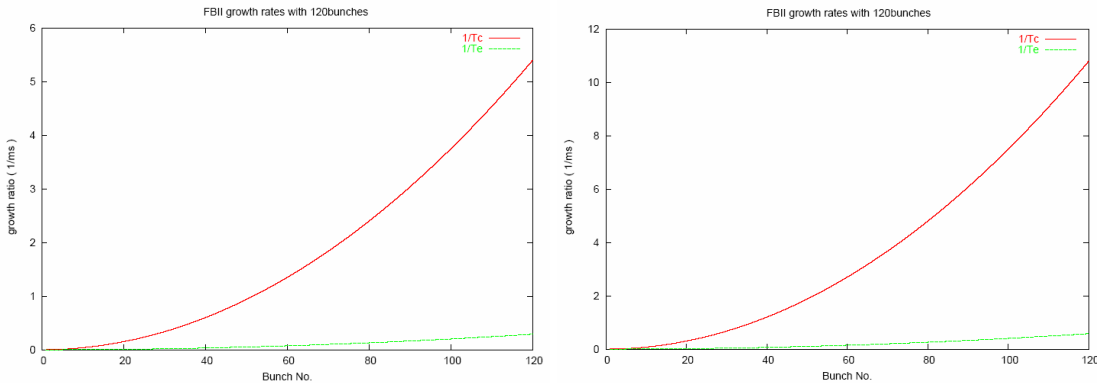


Figure 2.4.4- 7, 8: Growth rates of FBII at 10 GeV (left) and 5 GeV (right), 1000 mA

Electron Cloud Effects (ECE)

In the positron-hadron collision operation of eRHIC, the photo electrons generated by synchrotron radiation hitting the vacuum chamber walls, and secondary emission due to multipacting in the presence of the electric field of the positron beam, can accumulate in the beam pipe during the multi-bunch operation with short bunch spacing. This gives rise to a so-called ‘electron cloud’ (EC). Several effects have been observed in different machines, including

- Pressure rise
- Beam-size blow-up
- Coupled-bunch instability, etc.

Multi-bunch effect

For coupled-bunch instability due to EC, if we assume that the density of the electron cloud is saturated, then the growth time can be estimated as [10]

$$\tau_{CB} = \frac{\gamma \omega_{\beta} h_x h_y L_{sep}}{2 r_e N_b c^2} \quad (2.4.4-5)$$

γ is relative energy factor, ω_{β} is betatron frequency, h_x, h_y are transverse dimensions of the vacuum chamber, L_{sep} is bunch spacing, N_b is number of particles per bunch. Assuming similar vacuum chamber dimensions to that of the existing lepton machines, the growth time is at the level of 1.0 ms in e+ operation.

Single bunch effect

The electron cloud can also drive single bunch instability. Here we use treat it as a transverse mode-coupling instability. With a two-particle model, the threshold electron density of TMCI is [11]

$$\rho_{e,threshold} \approx \frac{2 \mathcal{W}_s}{\pi \beta_y r_e C} \quad (2.4.4-6)$$

C is ring circumference, ν_s is synchrotron tune. The threshold is about 1.2×10^{13} at 10 GeV and 0.6×10^{13} at 5 GeV, respectively. The preliminary simulation shows that the electron cloud density in eRHIC lepton ring could reach this level if no precautionary measure is taken.

To better examine the EC effect for the eRHIC electron operation a comparison is also made among eRHIC and the two Low Energy Rings of B-factories. See Table 2.4.4-11.

The major cures include:

- a vacuum ante-chamber
- coating of the chamber with TiN or NEG
- installation of solenoid coils

The first two measures may reduce the electron cloud density by a factor 3~10. The solenoids field (20~30 Gauss) also prove to be a very effective method to suppress the electron cloud effects in low energy rings of B-Factories [7][8]. The eRHIC lepton ring will adopt the ante-chamber concept with proper coatings in vacuum system designs and the solenoid coils can be the backup solution.

	B-factory parameters	eRHIC scaling factor over B-F parameters
N_b	$\sim 1E11$	1~2
L_{sep}	~ 2.5 m	~ 4
σ_x	~ 0.8 mm	~ 1
σ_y	~ 0.12 mm	~ 3
E	3.1~3.5 GeV	$\sim 1.5\sim 3$
C	2200~3100 m	1.7 ~ 2.4

Table 2.4.4- 11 Scaling ECE effects in positron operation of eRHIC

It appears that the electron cloud effects in positron mode will not be stronger than those in today's B-factories, mainly due to the longer bunch spacing and higher beam energy in eRHIC. By taking the necessary measures mentioned above, the electron cloud effects in positron operation will be under control. The more detailed numerical simulations are underway.

In conclusion, we have made preliminary investigations of the major expected instabilities through analytical calculations, simulations, and scaled performance from the other lepton machines, mainly B-factories. These estimates indicate that good engineering design and feedback can limit the instabilities to a similar or lower level than the B-factories at similar energy.

References:

1. T. Ieiri, et al., Impedance Measurements in the KEKB, EPAC 2000, Vienna, Austria (2000)
2. R. Rimmer, J. Bird, D. Li, Comparison of calculated, measured, and beam sampled impedances of a higher-order-mode-damped rf cavity, Physical Review Special Topics, Volume 3, 102001(2000)
3. PEP-II, an Asymmetric B Factory: A Conceptual Design Report, SLAC-R-418(1993)
4. KEKB B-factory Design Report, KEK Report 95-7(1995)
5. T. Raubenheimer and F. Zimmermann, Physical Review E 52, no.5, p.5487(1995)
6. M. Zisman, S. Chattopadhyay, J. Bisognano, ZAP User's Manual, LBL-21270(1986)
7. J. T. Seeman, Invited Talk in Super B-Factory Workshop in Hawaii, Honolulu, Jan. 19~22, 2004(2004)
8. J. Flanagan, Invited talk in Super B-Factory Workshop in Hawaii, Honolulu, Jan. 19 ~22, 2004(2004)
9. A. Chao, M. Tigner, Handbook of Accelerator Physics and Engineering, World Scientific(1999)
10. F. Zimmermann, G. Rumolo, APAC 2001, 352(2001)
11. K. Ohmi, F. Zimmermann, Physical Review Letters 85, 3821(2000)
12. D. H. Rubin, et al., CESR Status and Performance, PAC 2001, Chicago, 3520(2001)

2.4.5 Beam-Beam Issues

Overview

The beam-beam interaction is one of the most fundamental limitations of colliding beam storage rings. In the eRHIC collider, the beam-beam interaction varies depending on beam energy, colliding particle species, beam current, emittance, and other parameters, and can be quite different under different experimental scenarios. We work from the basic premise that: when the beam-beam interaction is weak, the luminosity performance is mainly dependent on single beam parameters of the e-ring or the RHIC ring; when beam-beam interactions are strong, beam-beam interaction can cause beam blowup, and coherent beam-beam oscillations are likely to be the major obstacle to reaching high luminosity. The following issues are discussed below in addition to the preliminary simulation worked presented in the next section.

Beam-beam interaction, interpretation

The eRHIC collider is similar in nature to HERA except for operating in a different range of center of mass energy and with much higher luminosity. In HERA the proton bunch intensity is $\sim 10^{11}$, which is comparable to RHIC proton beam intensity. But the electron beam current is limited by available RF power to about 58 mA. Therefore a weak-strong model can be applied to simulations. In the eRHIC electron ring, beam energy is only one third that of HERA, so that RF power does not limit beam current. The design beam intensity is 0.45A, about 10 times higher than HERA. And even higher beam intensities are under consideration to generate higher luminosity. Therefore, in many of the eRHIC collision scenarios both the lepton and the hadron beam-beam tune shift limits can be reached. In this case quasi strong-strong or strong-strong models of collision for simulation will be the more accurate tools.

Coherent beam-beam limit (asymmetric collider)

A distinguishing difference of the eRHIC from the existing colliders is the asymmetric circumference of the two colliding rings. The different and smaller circumference of the e-ring permits freedom of design optimization and substantial cost saving. However, coherent beam-beam interactions for the asymmetrical system may limit its performance and must be carefully accounted for. According to reference [1], the instability region of a 1:3 asymmetric e+e- ring collider compared to a symmetric one is about 30% larger with a beam-beam parameter of 0.03. In the present case we have a more complicated collision pattern and our beam-beam tune shift limit is much higher.

Weak radiation damping at low electron beam energy

Operating the electron ring at low energy (5GeV) significantly reduces synchrotron radiation damping, which will reduce the electron beam-beam tune shift limit to half. Measures to increase the damping at low electron energy are discussed in section 2.4.3.

Luminosity reduction from hourglass effect

The minimum proton beam bunch length is limited by the heat load on the cryogenic system for RHIC [2], and is considered to be ~ 20 cm at present. This sets a limit on minimum β^* for both hadron and lepton beams due to the luminosity reduction caused by hourglass effects.

Beam-beam effect on polarization

There were observations in HERA operation [3]. And will be an important issue here. Initial simulations have been done with a weak-strong mode and with linear lattice. That allows us to make a quick evaluation of possible maximum tune shift limits to select the appropriate working point.

Beam-Beam Simulations with Linear Lattice

RHIC is currently operating with beams colliding in four of its six interaction points, where beam-beam tune shift parameters exceeding $\xi_x = 0.005$ per IP have been achieved. It is therefore expected to be safe to assume the same beam-beam parameter for the eRHIC IP, especially since it is most likely that by the time eRHIC is operational the number of actual RHIC IPs will be reduced.

To investigate the feasibility of beam-beam interactions with nominal beam-beam tune shift parameters as high as $\xi_x = 0.025, \xi_y = 0.08$ in the eRHIC electron ring, simulation studies have been performed [4]. In these simulations, the accelerator is represented by a linear one-turn matrix. The tunes of this one-turn matrix are scanned in the range below the quarter resonance to determine the best working point. Synchrotron radiation damping and quantum excitation is included, currently based on an older lattice version that did not produce the emittances required for the interaction region parameters presented here. However, these simulations can nevertheless be considered useful at the present design stage. As a first step, the hadron bunch intensity was lowered such that a vertical beam-beam tune shift of $\xi_y = 0.05$ was achieved, which is the design value of the KEK B-Factory. With a radiation damping time corresponding to 1740 revolutions in the eRHIC electron ring, no beam blow-up and resulting luminosity degradation is observed over a wide tune range around $Q_x = .10, Q_y = .15$, as shown in Figure 2.4.5-1. It should however be emphasized here that due to the lack of a consistent lattice solution, the dynamic emittance effect caused by the modification of the H function,

$$H(s) = \gamma(s)\eta^2(s) + 2\alpha(s)\eta(s)\eta'(s) + \beta(s)\eta'^2(s), \quad (2.4.5-1)$$

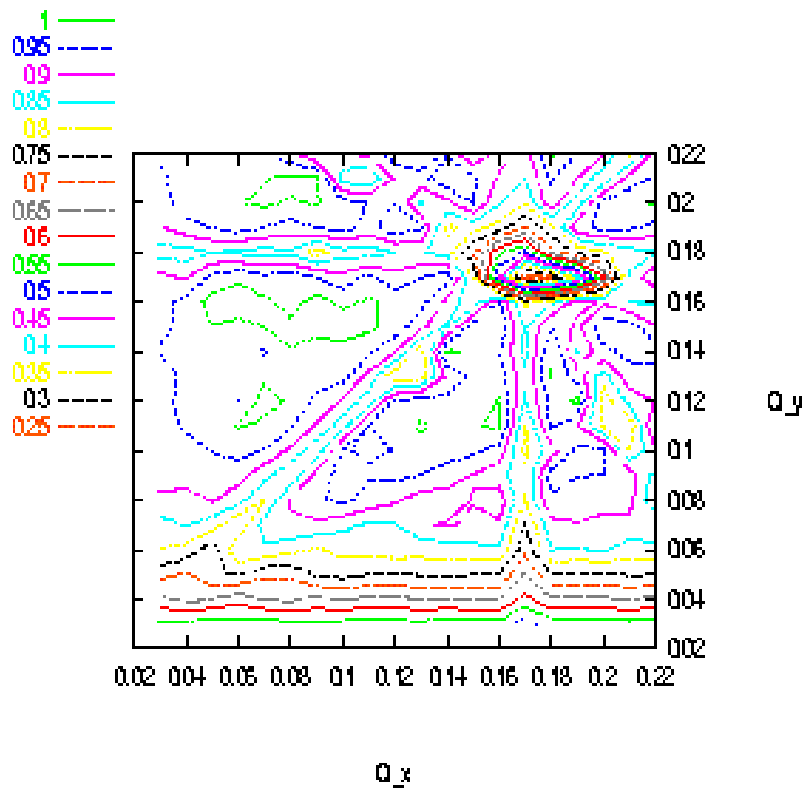
by the presence of a strong beam-beam lens could not be taken into account. Since these effects are mainly observed for tunes very close to the integer or half-integer, this is not expected to significantly alter the results.

Since the nominal hadron bunch intensity had to be lowered by about 40 percent compare to what is routinely accelerated in RHIC to limit the electron beam-beam tune shift to $\xi_y = 0.05$, we studied the effect of the eRHIC design beam-beam parameter, $\xi_x = 0.025, \xi_y = 0.08$, as it results from the regular RHIC bunch intensity of $1.0 \cdot 10^{11}$ protons per bunch. As Figure 2.4.5-2 indicates, there are still large areas in the working diagram where the resulting luminosity is 95% of the nominal geometric value.

These results still have to be checked by full 6D tracking, including lattice nonlinearities and realistic machine imperfections. This work is currently in progress.

Electrons:	
ring circumference [m]	1278
geometric emittance hor./vert. [nm]	53/9.5
β functions hor./vert. [m]	0.19/0.27
particles/bunch	$6.7 \cdot 10^{10}$
beam-beam tune shift hor./vert.	0.025/0.08
damping times hor./vert./long. [turns]	1740/1740/870
Hadrons:	
ring circumference [m]	3834
geometric emittance hor./vert. [nm]	9.5/9.5
β functions hor./vert. [m]	1.04/0.27
particles/bunch	$8.2 \cdot 10^{10}$ (p), $1.0 \cdot 10^9$ (Au)
beam-beam tune shift hor./vert.	0.005/0.005
luminosity [$\text{cm}^{-2}\text{sec}^{-1}$]	$2.7 \cdot 10^{32}$

Table 2.4.5- 1: Parameter table.

Figure 2.4.5- 1: Beam-beam contour plot for nominal beam-beam tune shift parameters of $\xi_x = 0.015$, $\xi_y = 0.05$.

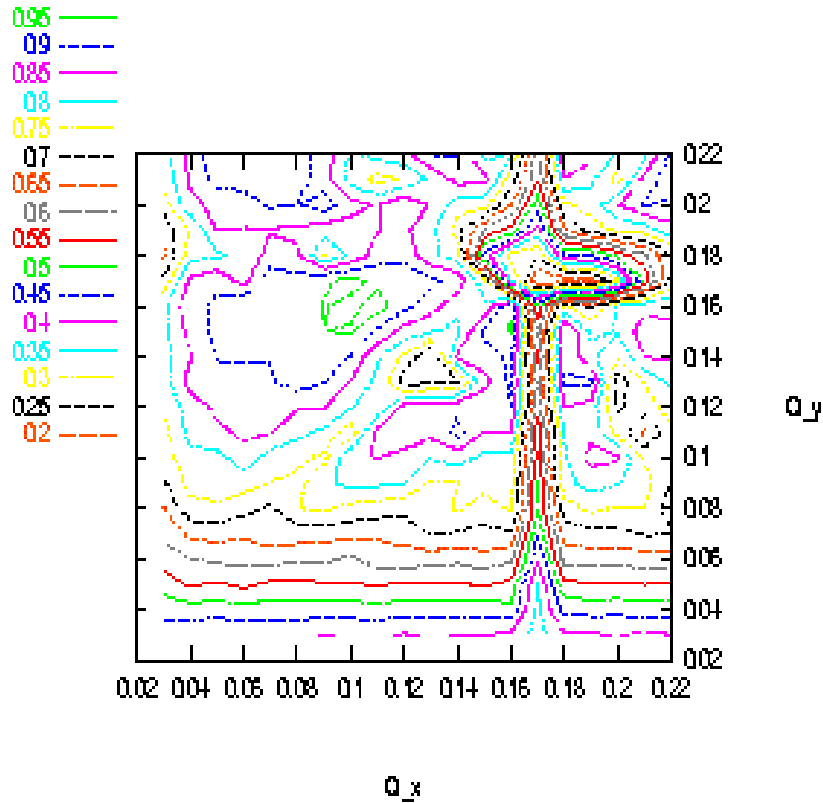


Figure 2.4.5- 2: Beam-beam contour plot for $\xi_x = 0.025, \xi_y = 0.08$, which corresponds to a proton bunch population of $1.0 \cdot 10^{11}$ /bunch.

References:

1. K. Hirata and E. Keil “Coherent beam-beam interaction limit in asymmetric ring colliders”, CERN/LEP-TH/89-54.
2. I. Ben-Zvi et al. “Accelerator physics issues in eRHIC”, NIM A 463(2001) 94-117.
3. M. Bieler et al., “Recent and past experiences with beam-beam effects at HERA”, LHC99 beam-beam workshop.
4. C. Montag, Proceedings of the 30th Advanced ICFA Beam Dynamics Workshop on high Luminosity e+e- Collisions, Stanford, 2003

2.4.6 Beam Polarization

Spin Polarization – an Overview

Before describing concepts for attaining electron and positron spin polarization for eRHIC we present a brief overview of the theory and phenomenology. We can then draw on this later as required. This overview is necessarily brief but more details can be found in [1, 2].

Self polarization

The spin polarization of an ensemble of spin- $\frac{1}{2}$ fermions with the same energies traveling in the same direction is defined as

$$\vec{P} = \left\langle \frac{2}{\hbar} \vec{\sigma} \right\rangle \quad (2.4.6-1)$$

where $\vec{\sigma}$ is the spin operator in the center of mass and $\langle \rangle$ denotes the expectation value for the mixed spin state. We denote the single particle center-of-mass expectation value of $\frac{2}{\hbar} \vec{\sigma}$ by \vec{S} and we call this the “spin”. The polarization is then the average of \vec{S} over an ensemble of particles such as that of a bunch of particles.

Relativistic e^\pm circulating in the (vertical) guide field of a storage ring emit synchrotron radiation and a tiny fraction of the photons can cause spin flip from up to down and vice versa. However, the up-to-down and down-to-up rates differ, with the result that in ideal circumstances the electron (positron) beam can become spin polarized anti-parallel (parallel) to the field, reaching a maximum polarization, P_{st} , of $\frac{8}{5\sqrt{3}} = 92.4\%$. This, the Sokolov–Ternov (S–T) polarizing process, is very slow on the time scale of other dynamical phenomena occurring in storage rings, and the inverse time constant for the exponential build up is [3]:

$$\tau_{st}^{-1} = \frac{5\sqrt{3}}{8} \frac{r_e \gamma^5 \hbar}{m_e |\rho|^3} \quad (2.4.6-2)$$

where r_e is the classical electron radius, γ is the Lorentz factor, ρ is the radius of curvature in the magnets and the other symbols have their usual meanings. The time constant is usually in the range of a few minutes to a few hours.

However, even without radiative spin flip, the spins are not stationary but precess in the external fields. In particular, the motion of \vec{S} for a relativistic charged particle traveling in electric and magnetic fields is governed by the Thomas–BMT equation $d\vec{S}/ds = \vec{\Omega} \times \vec{S}$ where s is the distance around the ring [2, 4]. The vector $\vec{\Omega}$ depends on the electric (\vec{E}) and magnetic (\vec{B}) fields, the energy and the velocity \vec{v} which evolves according to the Lorentz equation:

$$\vec{\Omega} = \frac{e}{m_e c} \left[-\left(\frac{1}{\gamma} + a \right) \vec{B} + \frac{a\gamma}{1+\gamma} \frac{1}{c^2} (\vec{v} \cdot \vec{B}) \vec{v} + \frac{1}{c^2} \left(a + \frac{1}{1+\gamma} \right) (\vec{v} \times \vec{E}) \right] \quad (2.4.6-3)$$

$$= \frac{e}{m_e c} \left[-\left(\frac{1}{\gamma} + a \right) \vec{B}_\perp - \frac{g}{2\gamma} \vec{B}_\parallel + \frac{1}{c^2} \left(a + \frac{1}{1+\gamma} \right) (\vec{v} \times \vec{E}) \right]. \quad (2.4.6-4)$$

Thus $\vec{\Omega}$ depends on s and on the position of the particle $u \equiv (x, p_x, y, p_y, l, \delta)$ in the 6–D phase space of the motion. The coordinate δ is the fractional deviation of the energy from the energy of a synchronous particle (“the beam energy”) and l is the distance from the center of the bunch. The

coordinates x and y are the horizontal and vertical positions of the particle relative to the reference trajectory and (except in solenoids) $p_x = x'$ and $p_y = y'$ are their conjugate momenta. The quantity g is the appropriate gyromagnetic factor and $a = (g - 2)/2$ is the gyromagnetic anomaly. For e^\pm , $a \approx 0.0011596$. B_\parallel and B_\perp are the magnetic fields parallel and perpendicular to the velocity.

In a simplified picture the majority of the photons in the synchrotron radiation do not cause spin flip but tend instead to randomize the e^\pm orbital motion in the (inhomogeneous) magnetic fields. Then, if the ring is insufficiently well geometrically aligned and/or if it contains special magnet systems like the “spin rotators” needed to produce longitudinal polarization at a detector (see below), the spin-orbit coupling embodied in the Thomas–BMT equation can cause spin diffusion, i.e. depolarization. Compared to the S–T polarizing effect the depolarization tends to rise very strongly with beam energy. The equilibrium polarization is then less than 92.4% and will depend on the relative strengths of the polarization and depolarization processes. As we shall see later, even without depolarization certain dipole layouts can reduce the equilibrium polarization to below 92.4 %.

Analytical estimates of the attainable equilibrium polarization are best based on the Derbenev–Kondratenko (D–K) formalism [5, 6]. This implicitly asserts that the value of the equilibrium polarization in an e^\pm storage ring is the same at all points in phase space and is given by

$$P_{\text{dk}} = \mp \frac{8}{5\sqrt{3}} \frac{\oint ds \left\langle \frac{1}{|\rho(s)|^3} \hat{b} \cdot \left(\hat{n} - \frac{\partial \hat{n}}{\partial \delta} \right) \right\rangle_s}{\oint ds \left\langle \frac{1}{|\rho(s)|^3} \left(1 - \frac{2}{9} (\hat{n} \cdot \hat{s})^2 + \frac{11}{18} \left(\frac{\partial \hat{n}}{\partial \delta} \right)^2 \right) \right\rangle_s} \quad (2.4.6-5)$$

where $\langle \rangle_s$ denotes an average over phase space at azimuth s , \hat{s} is the direction of motion and $\hat{b} = (\hat{s} \times \dot{\hat{s}}) / |\dot{\hat{s}}|$. \hat{b} is the magnetic field direction if the electric field vanishes and the motion is perpendicular to the magnetic field. \hat{n} is a unit 3–vector field over the phase space satisfying the Thomas–BMT equation along particle trajectories $u(s)$ (which are assumed to be integrable) and it is 1–turn periodic: $\hat{n}(u; s + C) = \hat{n}(u; s)$ where C is the circumference of the ring.

The field $\hat{n}(u; s)$ is a key object for systematizing spin dynamics in storage rings. It provides a reference direction for spin at each point in phase space and it is now called the “invariant spin field” [2, 7, 8]. At zero orbital amplitude, i.e. on the periodic (“closed”) orbit, the $\hat{n}(0; s)$ is written as $\hat{n}_0(s)$. For e^\pm rings and away from spin–orbit resonances (see below), \hat{n} is normally at most a few milliradians away from \hat{n}_0 .

A central ingredient of the D–K formalism is the implicit assumption that the e^\pm polarization at each point in phase space is parallel to \hat{n} at that point. In the approximation that the particles have the same energies and are traveling in the same direction, the polarization of a bunch measured in a polarimeter at s is then the ensemble average

$$\vec{P}_{\text{ens,dk}}(s) = P_{\text{dk}} \langle \vec{n} \rangle_s. \quad (2.4.6-6)$$

In conventional situations in e^\pm rings, $\langle \hat{n} \rangle_s$ is very nearly aligned along $\hat{n}_0(s)$. The *value* of the ensemble average, $P_{\text{ens,dk}}(s)$, is essentially independent of s .

Equation 2.4.6-5 can be viewed as having three components. The piece

$$\begin{aligned}
P_{\text{bk}} &= \mp \frac{8}{5\sqrt{3}} \frac{\oint ds \left\langle \frac{1}{|\rho(s)|^3} \hat{b} \cdot \hat{n} \right\rangle_s}{\oint ds \left\langle \frac{1}{|\rho(s)|^3} \left(1 - \frac{2}{9} (\hat{n} \cdot \hat{s})^2 \right) \right\rangle_s} \quad (2.4.6-7) \\
&\approx \mp \frac{8}{5\sqrt{3}} \frac{\oint ds \frac{1}{|\rho(s)|^3} \hat{b} \cdot \hat{n}_0}{\oint ds \frac{1}{|\rho(s)|^3} \left(1 - \frac{2}{9} n_{0s}^2 \right)}
\end{aligned}$$

gives the equilibrium polarization due to radiative spin flip. The quantity n_{0s} is the component of \hat{n}_0 along the closed orbit. The subscript “bk” is used here instead of “st” to reflect the fact that this is the generalization by Baier and Katkov [9, 10] of the original S–T expression to cover the case of piecewise homogeneous fields. Depolarization is then accounted for by including the term with $\frac{11}{18} \left(\frac{\partial \hat{n}}{\partial \delta} \right)^2$ in the denominator. Finally, the term with $\frac{\partial \hat{n}}{\partial \delta}$ in the numerator is the so-called kinetic polarization term. This results from the dependence of the radiation power on the initial spin direction and is not associated with spin flip. It can normally be neglected but is still of interest in rings with special layouts.

In the presence of radiative depolarization the rate in Eq. 2.4.6- 2 must be replaced by

$$\tau_{\text{dk}}^{-1} = \frac{5\sqrt{3}}{8} \frac{r_e \gamma^5 \hbar}{m_e C} \oint ds \left\langle \frac{1}{|\rho(s)|^3} \left(1 - \frac{2}{9} (\hat{n} \cdot \hat{s})^2 + \frac{11}{18} \left(\frac{\partial \hat{n}}{\partial \delta} \right)^2 \right) \right\rangle_s \quad (2.4.6-8)$$

This can be written in terms of the spin-flip polarization rate, τ_{bk}^{-1} , and the depolarization rate, τ_{dep}^{-1} , as:

$$\frac{1}{\tau_{\text{dk}}} = \frac{1}{\tau_{\text{bk}}} + \frac{1}{\tau_{\text{dep}}}, \quad (2.4.6-9)$$

where

$$\tau_{\text{dep}}^{-1} = \frac{5\sqrt{3}}{8} \frac{r_e \gamma^5 \hbar}{m_e C} \oint ds \left\langle \frac{1}{|\rho(s)|^3} \frac{11}{18} \left(\frac{\partial \hat{n}}{\partial \delta} \right)^2 \right\rangle_s \quad (2.4.6-10)$$

and

$$\tau_{\text{bk}}^{-1} = \frac{5\sqrt{3}}{8} \frac{r_e \gamma^5 \hbar}{m_e C} \oint ds \left\langle \frac{1}{|\rho(s)|^3} \left(1 - \frac{2}{9} (\hat{n} \cdot \hat{s})^2 \right) \right\rangle_s \quad (2.4.6-11)$$

The time dependence for build-up from an initial polarization P_0 to equilibrium is

$$P(t) = P_{\text{ens,dk}} \left[1 - e^{-t/\tau_{\text{dk}}} \right] + P_0 e^{-t/\tau_{\text{dk}}}. \quad (2.4.6-12)$$

In perfectly aligned e^\pm storage rings containing just horizontal bends, quadrupoles and accelerating cavities, there is no vertical betatron motion and $\hat{n}_0(s)$ is vertical. Since the spins do not “see” radial quadrupole fields and since the electric fields in the cavities are essentially parallel to the particle motion, \hat{n} is vertical, parallel to the guide fields and to $\hat{n}_0(s)$ at all u and s . Then the derivative $\frac{\partial \hat{n}}{\partial \delta}$ vanishes and there is no depolarization. However, real rings have misalignments. Then there is

vertical betatron motion so that the spins also see radial fields which tilt them from the vertical. Moreover, $\hat{n}_0(s)$ is also tilted and the spins can couple to vertical quadrupole fields too. As a result \hat{n} becomes dependent on u and “fans out” away from $\hat{n}_0(s)$ by an amount which usually increases with the orbit amplitudes. Then in general $\frac{\partial \hat{n}}{\partial \delta}$ no longer vanishes in the dipoles (where $1/|\rho|^3$ is large) and depolarization occurs. In the presence of skew quadrupoles and solenoids and in particular in the presence of spin rotators, $\frac{\partial \hat{n}}{\partial \delta}$ can be non-zero in dipoles even with perfect alignment. The deviation of \hat{n} from $\hat{n}_0(s)$ and the depolarization tend to be particularly large near to the spin-orbit resonance condition

$$\nu_{\text{spin}} = k_0 + k_I \nu_I + k_{II} \nu_{II} + k_{III} \nu_{III}. \quad (2.4.6-13)$$

Here $k_0, k_I, k_{II}, k_{III}$ are integers, $\nu_I, \nu_{II}, \nu_{III}$ are the three tunes of the synchrotron motion and ν_{spin} is the spin tune on the closed orbit, i.e. the number of precessions around $\hat{n}_0(s)$ per turn, made by a spin on the closed orbit¹. In the special case, or in the approximation, of no synchrotron coupling one can make the associations: $I \rightarrow x$, $II \rightarrow y$ and $III \rightarrow s$, where, here, the subscript s labels the synchrotron mode. In a simple flat ring with no closed orbit distortion, $\nu_{\text{spin}} = a\gamma_0$ where γ_0 is the Lorentz factor for the nominal beam energy. For e^\pm , $a\gamma_0$ increments by 1 for every 441 MeV increase in beam energy. In the presence of misalignments and special elements like rotators, ν_{spin} is usually still approximately proportional to the beam energy. Thus an energy scan will show peaks in τ_{dep}^{-1} and dips in $P_{\text{ens,dk}}(s)$, namely at the resonances. Examples can be seen in figure 2.4.6-3 below. The resonance condition expresses the fact that the disturbance to spins is greatest when the $|\vec{\Omega}(u;s) - \vec{\Omega}(0;s)|$ along an orbit is coherent (“in step”) with the natural spin precession. The quantity $(|k_I| + |k_{II}| + |k_{III}|)$ is called the order of the resonance. Usually, the strongest resonances are those for which $|k_I| + |k_{II}| + |k_{III}| = 1$, i.e. the first order resonances. The next strongest are usually the so-called “*synchrotron sideband resonances*” of parent first order resonances, i.e. resonances for which $\nu_{\text{spin}} = k_0 \pm \nu_{I,II,III} + \tilde{k}_{III} \nu_{III}$ where \tilde{k}_{III} is an integer and mode III is associated with synchrotron motion. All resonances are due to the non-commutation of successive spin rotations in 3-D and they therefore occur even with purely linear orbital motion.

We now list some keys points.

- The approximation in the second row of Eq. 2.4.6- 7 makes it clear that if there are dipole magnets with fields not parallel to \hat{n}_0 , as is the case, for example, when spin rotators are used, then P_{bk} can be lower than the 92.4% achievable in the case of a simple ring with no solenoids and where all dipole fields and $\hat{n}_0(s)$ are vertical.
- If, as is usual, the kinetic polarization term makes just a small contribution, the above formulae can be combined to give

$$P_{\text{ens,dk}} \approx P_{\text{bk}} \frac{\tau_{\text{dk}}}{\tau_{\text{bk}}}. \quad (2.4.6-14)$$

From Eq. 2.4.6- 9 it is clear that $\tau_{\text{dk}} \leq \tau_{\text{bk}}$.

- The underlying rate of polarization due to the S–T effect, τ_{bk}^{-1} , increases with the fifth power

¹ In fact the resonance condition should be more precisely expressed in terms of the so-called amplitude dependent spin tune [2, 7, 8]. But for typical e^\pm rings, the amplitude dependent spin tune differs only insignificantly from ν_{spin} .

of the energy and decreases with the third power of the bending radii.

- It can be shown that as a general rule the “normalized” strength of the depolarization, $\tau_{\text{dep}}^{-1} / \tau_{\text{bk}}^{-1}$, increases with beam energy according to a tune dependent polynomial in even powers of the beam energy.

Pre-polarization

Instead of relying on self polarization, for e^- one can inject a pre-polarized beam. The polarized e^- are supplied by a gallium arsenide source and then accelerated to full energy in a linear accelerator. Gallium arsenide sources can provide polarizations of 80%. Acceleration in a recirculating device is also possible provided measures are taken to avoid depolarization when accelerating through resonances. The CEBAF machine at the Thomas Jefferson National Accelerator Facility is an example of such a device. These matters are discussed in other sections. It would be necessary to inject the pre-polarized e^- at full energy since it is unlikely that the polarization would survive resonance crossing during acceleration in the ring itself.

Since no simple polarized sources exist for e^+ , a pre-polarized e^+ beam would have to be polarized by the S–T effect in a dedicated preceding ring.

To avoid an immediate loss of polarization in the recipient ring, the polarization vector should lie along the \hat{n}_0 vector at the injection point. In that case the subsequent time dependence is given by Eq. 2.4.6- 12. Note that if the injected polarization is higher than the $P_{\text{ens,dk}}$, the polarization will *fall* to this value with the characteristic time τ_{dk} . Furthermore, if the injected polarization has the “wrong” sign, the S–T effect will drive the polarization through zero and into the natural direction. Again, the characteristic time will be τ_{dk} and the final value will be $P_{\text{ens,dk}}$. Injecting a pre-polarized beam is the only solution if the required energy of the stored beam is so low that τ_{bk} is impractically large. It is also useful if the lifetime of the stored beam is small: full polarization is immediately available while the luminosity is still high.

Software

There are two classes of computer algorithm for estimating the equilibrium polarization in real e^\pm rings:

- (i) Methods based on evaluating \hat{n} and $\left(\frac{\partial \hat{n}}{\partial \delta}\right)^2$ in the D–K formula given the ring layout and magnet strengths; and
- (ii) A more pragmatic approach in which particles and their spins are tracked while photon emission is simulated approximately within a Monte–Carlo framework and τ_{dep} is “measured”. Eqs. 2.4.6- 9 and 2.4.6- 14 then provide an estimate of τ_{dk} and the equilibrium polarization. The programs SITROS [11] and SLICKTRACK [12] exemplify this approach.

The class (i) algorithms are further divided according to the degree of linearization of the spin and orbital motion:

- (ia) The SLIM family (SLIM [13, 14], SLICK [15], SITF [11]) and SOM [16] and ASPIRRIN [17]. The last two utilize approximate versions of the “betatron–dispersion” formalism [1]

and all are based on a linearization of the orbital and spin motion. For spin, the linearization involves assuming that the angle between \hat{n} and \hat{n}_0 is small at all positions in phase space so that \hat{n} can be approximated by the form $\hat{n}(u; s) \approx \hat{n}_0(s) + \alpha(u; s)\hat{m}(s) + \beta(u; s)\hat{l}(s)$. The unit vectors \hat{m} and \hat{l} are 1–turn periodic and chosen so that the set $\{\hat{n}_0, \hat{m}, \hat{l}\}$ is orthonormal. It is assumed that $\sqrt{\alpha^2 + \beta^2} \ll 1$. This approximation reveals just the first order spin–orbit resonances and it breaks down when $\sqrt{\alpha^2 + \beta^2}$ becomes large very close to these resonances.

(ib) SMILE [6]: Linearized orbital motion but “full” spin motion using a high order perturbation theory.

(ic) SODOM [18]: Linearized orbital motion but full spin motion expressed by a Fourier expansion.

Note that the precise evaluation of \hat{n} and $(\frac{\partial \hat{n}}{\partial \delta})^2$ requires calculating beyond the linear approximation. Then large amounts of computer power are needed, especially if a large number of resonances must be taken into account. Thus the calculations presented here are based on a class (ia) algorithm, in particular that in SLICK. This executes very quickly and it furnishes valuable first impressions, even though it can only exhibit the first order resonances. At a later stage results from SLICKTRACK based on a class (ii) algorithm and full spin motion will be available. Then the influence of higher order resonances will be seen. This kind of algorithm also allows the effect of non–linear orbital motion and the beam–beam interaction to be studied. The class (ii) algorithm is mathematically much simpler than the class (i) algorithm but it still requires a large amount of computing power for the simulation for long enough of the motion of enough particles and their spins.

Spin rotators

The eRHIC project, like all analogous projects involving spin, needs longitudinal polarization at the interaction point. However, if the S–T effect is to be the means of making or maintaining the polarization, then as is clear from Eq. 2.4.6- 7, \hat{n}_0 must be close to vertical in most of the dipoles. We have seen at Eq. 2.4.6- 6 that the polarization is essentially parallel to \hat{n}_0 . So to get longitudinal polarization at a detector, it must be arranged that \hat{n}_0 is longitudinal at the detector but vertical in the rest of the ring. This can be achieved with magnet systems called spin rotators which rotate \hat{n}_0 from vertical to longitudinal on one side of the detector and back to vertical again on the other side. Eq. 2.4.6- 7 shows that P_{bk} essentially scales with the cosine of the angle of tilt of \hat{n}_0 from the vertical in the arc dipoles. Thus a rotation error resulting in a tilt of \hat{n}_0 of even a few degrees would not reduce P_{bk} by too much. However, as was mentioned above, a tilt of \hat{n}_0 in the arcs can lead to depolarization and calculations show that tilts of more than about a degree produce significant depolarization. Thus well tuned rotators are essential for maintaining polarization even if the beam is pre–polarized before injection.

Suppression of depolarization – spin matching

Although the S–T effect offers a convenient way to obtain stored high energy e^\pm beams, it is only useful in practice if there is not too much depolarization. Depolarization can also limit the usefulness of beams pre–polarized before injection: τ_{dk} must be large enough to ensure that the large injected polarization survives until it is safe to switch on the sensitive parts of the detector after injection and survives long enough for collecting enough data in the detector. Depolarization can be significant if

the ring is misaligned, if it contains spin rotators or if it contains uncompensated solenoids or skew quadrupoles. Then if $P_{\text{ens,dk}}$ and/or τ_{dk} are too small, the layout and the optic must be adjusted so that $\left(\frac{\partial \hat{n}}{\partial \delta}\right)^2$ is small where $1/|\rho|^3$ is large. So far it is only possible to do this within the linear approximation for spin motion. This technique is called “*linear spin matching*” and when successful, as for example at HERA [19], it immediately reduces the strengths of the first order spin–orbit resonances. Spin matching requires two steps: “*strong synchrobeta spin matching*” is applied to the optics and layout of the perfectly aligned ring and then “*harmonic closed orbit spin matching*” is applied to soften the effects of misalignments. This latter technique aims to adjust the closed orbit so as to reduce the tilt of \hat{n}_0 from the vertical in the arcs. Since the misalignments can vary in time and are usually not sufficiently well known, the adjustments are applied empirically while the polarization is being measured.

Spin matching must be approached on a case by case basis. An overview can be found in [1]. Spin matching for eRHIC will be discussed later.

Higher order resonances

Even if the beam energy is chosen so that first order resonances are avoided and in linear approximation $P_{\text{ens,dk}}$ and/or τ_{dk} are expected to be large, it can happen that that beam energy corresponds to a higher order resonance. In practice the most intrusive higher order resonances are those for which $\nu_{\text{spin}} = k_0 \pm \nu_k + \tilde{k}_s \nu_s$ ($k \equiv I, II$ or III). These synchrotron sideband resonances of the first order parent resonances are due to modulation by energy oscillations of the instantaneous rate of spin precession around \hat{n}_0 . The depolarization rates associated with sidebands of isolated parent resonances ($\nu_{\text{spin}} = k_0 \pm \nu_k$) are related to the depolarization rates for the parent resonances. For example, if the beam energy is such that the system is near to a dominant ν_y resonance we can approximate τ_{dep}^{-1} in the form

$$\tau_{\text{dep}}^{-1} \propto \frac{A_y}{\left(\nu_{\text{spin}} - k_0 \pm \nu_y\right)^2}. \quad (2.4.6-15)$$

This becomes

$$\tau_{\text{dep}}^{-1} \propto \sum_{\tilde{k}_s=-\infty}^{\infty} \frac{A_y B_y(\zeta; \tilde{k}_s)}{\left(\nu_{\text{spin}} - k_0 \pm \nu_y + \tilde{k}_s \nu_s\right)^2}$$

if the synchrotron sidebands are included. The quantity A_y depends on the beam energy and the optics and is reduced by spin matching. The proportionality constants $B_y(\zeta; \tilde{k}_s)$ are called *enhancement factors*, and they contain modified Bessel functions $I_{|\tilde{k}_s|}(\zeta)$ and $I_{|\tilde{k}_s|+1}(\zeta)$ which depend on the *modulation index* $\zeta = (a\gamma_0\sigma_\delta/\nu_s)^2$. More formulae can be found in [20].

Thus the effects of synchrotron sideband resonances can be reduced by doing the spin matches described above. Note that these formulae are just meant as a guide since they are approximate and explicitly neglect interference between the first order parent resonances. To get a complete impression, the Monte–Carlo simulation mentioned earlier must be used. The sideband strengths generally increase with the energy spread and the beam energy.

Spin Polarization in eRHIC

Choice of rotators

For rings like eRHIC two kinds of rotator can be considered: “*solenoid rotators*” and “*dipole rotators*”. The current design employs solenoid rotators. Dipole rotators will be mentioned later.

Various layouts of rotators involving solenoids can be conceived [21, 22, 23]. The layout considered for eRHIC is sketched in figure 2.4.6-1. The vertical \hat{n}_0 in the arc is rotated by 45 degrees towards the horizontal by the longitudinal field of the first solenoid. A second solenoid completes the rotation into the horizontal plane. The vector \hat{n}_0 is then rotated from the radial direction towards the longitudinal direction by a string of horizontally bending dipoles. The orbital deflection required is $90/a\gamma_0$ degrees.

After the interaction point a string of dipoles of reverse polarity rotates \hat{n}_0 back to the radial direction and two solenoids with polarity opposite to that of the first two rotate \hat{n}_0 back to the vertical. Then \hat{n}_0 is vertical in the arcs at all energies. If a solenoid rotates \hat{n}_0 by 45 degrees, then for e^\pm the plane of the transverse particle distribution is rotated by about 22.5 degrees so that the rotator can generate strong transverse orbital coupling.

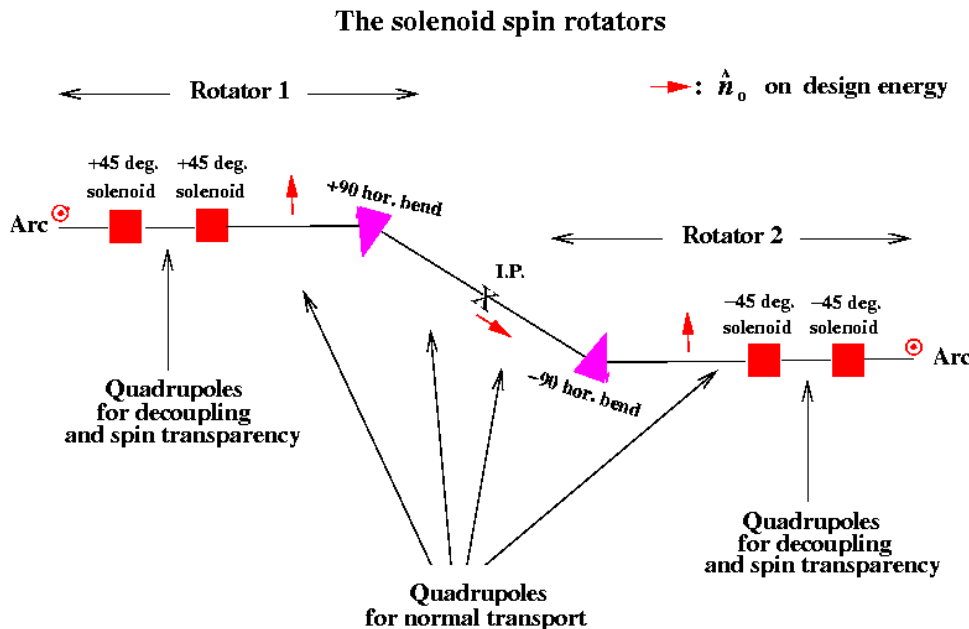


Figure 2.4.6- 1: The schematic layout of the solenoid rotators. Only the positions and functions of the key elements are shown. Each rotator consists of two solenoids and horizontal bend magnets, to rotate \hat{n}_0 into (or out of) the longitudinal direction. Quadrupoles tuned to ensure transverse decoupling and spin transparency w.r.t. x and x' are placed between each solenoid in each rotator. Antisymmetric horizontal bends very near the interaction point are not shown.

However, this coupling can be eliminated by correctly choosing the strengths and positions of quadrupoles placed within the first pair of solenoids and within the last pair (Figure 2.4.6- 1). The orbital motion between the first and second pair of solenoids is uncoupled and the quadrupole strengths in that region can be chosen as required.

Some advantages and disadvantages of solenoid rotators are:

Advantages:

- The arrangement is compact.
- In contrast to the dipole rotators discussed later, no vertical orbit excursion is needed.
- The sign of the longitudinal component of the equilibrium polarization at the interaction point can be reversed by simply changing the polarities of all the solenoids.

Disadvantages:

- The polarization is longitudinal at just one beam energy and that energy is defined by the field integrals of the horizontally bending dipoles on each side of the interaction point. Any remedy for this restriction would require elaborate engineering involving moving the solenoids. However, if it is planned to run eRHIC just around 10 GeV, say in the range 9.69 to 10.13 GeV ($\Rightarrow 22 \leq a\gamma_0 \leq 23$), \hat{n}_0 will always be within about 2 degrees of the beam direction.
- By the Thomas–BMT equation the rate of spin precession in a solenoid is inversely proportional to the beam energy. So solenoid spin rotators are only practical at low energy. At 10 GeV each solenoid needs a field integral of about 26.7 Tm and must therefore be superconducting.
- The solenoids cause transverse coupling which must be eliminated by introducing special quadrupole arrangements. Solenoid spin rotators are also not automatically spin transparent (see below).

A corresponding list of advantages and disadvantages for dipole rotators is given later.

The horizontal dispersion should be zero on entry to the first solenoid and at the exit from the last and the horizontal dispersion is set to zero at the interaction point.

Spin matching with the solenoid rotators

To explain the spin matching conditions needed when the solenoid rotators are used we begin by considering a flat, perfectly aligned ring without the rotators, the detector and the oncoming proton beam. In this case there is no vertical closed orbit distortion and the radiation damping together with the absence of vertical dispersion ensure that the beam has essentially zero thickness. Then as explained earlier, \hat{n}_0 is vertical and $\hat{n}(u; s)$ is vertical at all u and all s . The derivative $\frac{\partial \hat{n}}{\partial s}$ is then zero and there is no depolarization.

However, the solenoids have radial end fields which can tilt spins from the vertical and the longitudinal fields tilt spins step–wise into and out of the horizontal plane so that they then precess in the vertical fields of the quadrupoles inside and between the rotators. Inside a rotator, they also precess in the radial quadrupole fields at the non-zero y induced by the first solenoid of a pair.

Moreover, the total angle of rotation in the two solenoids of a rotator is ± 90 degrees only at $\delta = 0$. Since $\hat{n}(u; s)$ is a functional of the geometry and optics of the ring we see that unless special measures are taken, the solenoid rotators will cause \hat{n} to depend on u and s . Then $\frac{\partial \hat{n}}{\partial \delta}$ will not vanish in the dipoles in the arcs and there will be depolarization.

The remedy is to make the section from the entrance of the first rotator to the exit of the second rotator “*spin transparent*”, i.e. to choose the strengths and positions of quadrupoles and dipoles in this section so that in the approximation of linearized spin motion, the total rotation of a spin around and w.r.t. \hat{n}_0 vanishes for a spin beginning with arbitrary u and traversing this section. We have already mentioned that we eliminate the generation of transverse coupling by the solenoids with the aid of quadrupoles placed within the solenoid pairs. It then turns out that spin transparency w.r.t. x and x' can be arranged in addition, and in a straightforward way, by setting these quadrupoles such that the 4×4 transfer matrix for the transverse motion through a pair has the form [21]

$$\begin{pmatrix} 0 & -2r & 0 & 0 \\ 1/2r & 0 & 0 & 0 \\ 0 & 0 & 0 & 2r \\ 0 & 0 & -1/2r & 0 \end{pmatrix} \quad (2.4.6- 16)$$

where r is the radius of orbit curvature in the longitudinal field of a solenoid and where the elimination of coupling is explicit. The optic between the rotators should be uncoupled. Since the integral of the solenoid fields vanishes for the whole region, at first order there is no net spin perturbation resulting from non-zero δ in the solenoids. Moreover, the constraints on the horizontal dispersion and the layout of the dipoles around the interaction point ensure that the change in direction of the horizontal dispersion, due to quadrupole fields, vanishes for the stretch between the second and third solenoids. Thus there is transparency w.r.t. longitudinal motion too [1]. Providing that the constraints on the dispersion are satisfied, the optic between the second and third solenoids can be chosen at will independently of the need to ensure spin transparency, once the matrices for the rotators have the form just given. So far it has not been necessary to consider spin transparency w.r.t. y and y' since in the perfectly aligned ring and with transverse coupling restricted to the rotators themselves, synchrotron radiation in the arcs does not excite vertical motion. Then $y = 0$ and $y' = 0$ on entering a rotator from the arc. With these conditions it is easy to show that with linearized spin motion and perfect alignment, $\frac{\partial \hat{n}}{\partial \delta}$ indeed vanishes at all dipoles in the arcs [1]. We say that the ring is spin matched at each dipole in the arcs.

Thus although an isolated solenoid is not spin transparent, we have a very elegant way to ensure sufficient overall spin transparency of the whole rotator insertion. Moreover, from the above discussion about the requirements for the optic in the stretch between the second and third solenoids, it is clear that the depolarizing effects from beam-beam forces should be suppressed. The same probably applies to the detector field if it can be prevented from generating coupling. These count among the advantages of such solenoid spin rotators.

Note that our spin matching conditions do not ensure that $\frac{\partial \hat{n}}{\partial \delta}$ vanishes in the dipoles between the rotators. Moreover, since \hat{n}_0 is horizontal in the vertical fields of those dipoles, Eq. 2.4.6- 7 implies that P_{bk} can be lower than 92.4%. However, this lowering of P_{bk} can be limited by making the

dipoles long enough to ensure that their $\int ds / |\rho(s)|^3$ is small compared to that in the arcs. We return to these two points below.

Calculations of the e^\pm polarization in eRHIC

Following this lengthy introduction we now present first calculations of the polarization. The calculations are carried out with the thick lens code SLICK. This accounts for just the first order spin-orbit resonances. No account is taken of the magnetic field of the detector and there is no beam-beam force from oncoming protons. The horizontal and vertical betatron phase advances in the arc cells are 72 and 60 degrees respectively and the fractional parts of the betatron tunes are $[\nu_x] = 0.105$ and $[\nu_y] = 0.146$. The synchrotron tune, ν_s , is 0.044. SLICK automatically produces the correct transverse and longitudinal emittances.

Figure 2.4.6- 2 shows the equilibrium polarization for the perfectly aligned ring in the range 9.25 to 10.58 GeV. With these rotators the spin tune, ν_{spin} , on the design orbit is $a\gamma_0$. Thus this energy range corresponds to $21 \leq \nu_{\text{spin}} \leq 24$, i.e. it spans three full integers. It is seen that P_{bk} (labeled as S-T Polarization) is almost independent of energy at about 84.3%. It is below 92.4% because \hat{n}_0 is perpendicular to the fields in the dipoles around the interaction point. Recall Eq. 2.4.6- 7. The actual polarization, P_{dk} (labeled as Total Polarization), is about 81.7%. The additional decrease of about 2.6% is due to the depolarization caused by the non-zero $(\frac{\partial \hat{n}}{\partial \delta})^2$ in those dipoles. It is interesting that although there is some depolarization, this depolarization shows no resonant structure. This can be understood in terms of some 1-turn integrals appearing in the calculation of $\frac{\partial \hat{n}}{\partial \delta}$ [1]. When these integrals are evaluated starting somewhere in the arc, they are zero because of the spin matching. At resonance these integrals are independent of the starting point. Then they are zero starting at the dipoles around the interaction point and the factors A_x and A_s analogous to the A_y of Eq. 2.4.6- 15, vanish at resonance.

As stated earlier, misalignments can lead to depolarization. In fact experience shows that misalignments can be very dangerous and that care should be invested in the alignment of the ring and measurement of the orbit. Care is also needed for realistic simulations. Figure 2.4.6- 3 shows results of calculations of equilibrium polarizations with SLICK for typical realistic misalignments and after orbit correction. Figure 2.4.6- 4 shows the corresponding τ_{bk} and τ_{dk} . The τ_{bk} exhibits the characteristic γ_0^{-5} dependence. At 9.91 GeV ($a\gamma_0 = 22.5$) τ_{bk} and τ_{dk} are about 21 and 20 minutes respectively. At 5 GeV τ_{bk} would be about 11 hours. In that case self polarization would not be practical and a pre-polarised beam would be needed. Otherwise the average $1/|\rho|^3$ would have to be greatly increased [24].

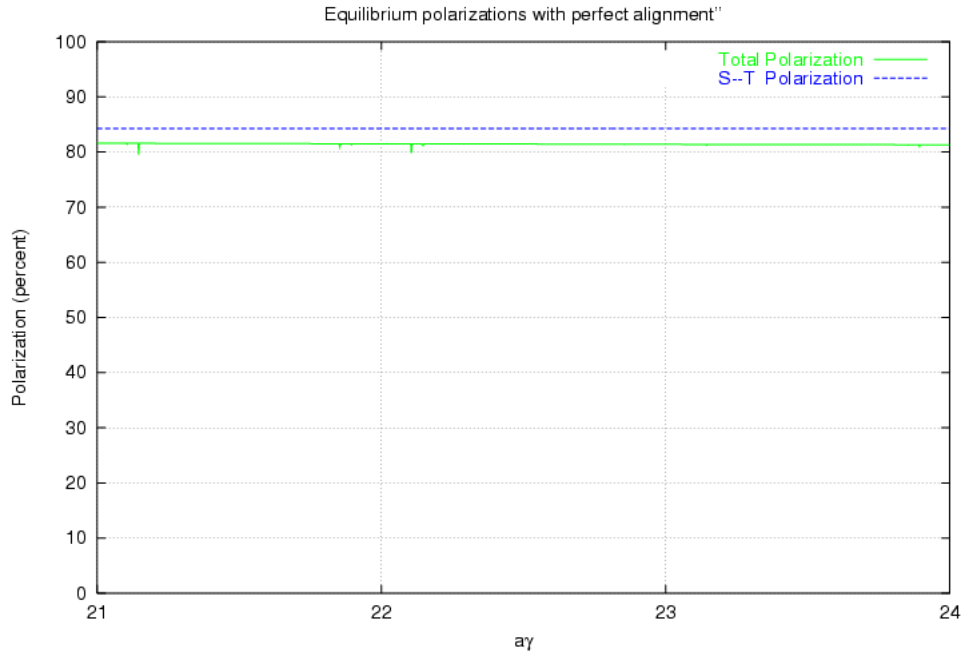


Figure 2.4.6- 2: The polarizations P_{bk} and P_{dk} for a perfectly aligned ring containing a spin transparent pair of solenoid spin rotators.

The misalignments include vertical shifts and roll on the quadrupoles, roll on the dipoles and errors on the beam position monitors. Scale errors on the quadrupole strengths are also included. A monitor and horizontal and vertical correction coils are assigned to each quadrupole. Figure 2.4.6- 3 shows five curves: P_{bk} (labeled as S–T Polarization), P_{dk} (bold and labeled as Total Polarization), and each of the polarizations that would be reached if just one orbital mode were excited. The first order resonances are clearly visible and can easily be identified using the known values of $[\nu_x]$, $[\nu_y]$ and ν_s . Note that the ν_s resonances are so strong that they overlap around integer values of ν_{spin}^2 . In this simulation the peak values of P_{dk} are about 81.5% and occur near half integer values of ν_{spin} . This is characteristic behavior and shows that the beam energy should be set for such values. It is also clear, as usual, that the fractional parts of the orbital tunes should be as far away from 1/2 as is practical to “leave space” around half integer spin tune. It might then be the case that the synchrotron sideband resonances are weak at the recommended energies. This conjecture will be checked at a later stage using a class (ii) simulation. Different choices of the random numbers specifying the imperfections lead to curves which differ in detail from those in figures 2.4.6- 3 and 2.4.6- 4. However, the curves remain qualitatively similar. Before orbit correction the polarization is very small.

In this simulation the tilt of \hat{n}_0 in the arcs is about 2.5 milliradians at the maxima of P_{dk} . The r.m.s. vertical deviation of the closed orbit from the design machine plane is 0.034 mm after the orbit correction mentioned above. The maximum deviation is 0.18 mm. Such small residual closed orbit deviations might look optimistic but realistic misalignments have been assumed and these small residuals arise naturally with the orbit correction algorithm used here. Moreover, the problem of

² But for this first order calculation τ_{dk} does *not* vanish at integer values of ν_{spin} : there are no ‘integer resonances’ in τ_{dk}^{-1} . However, the S–T effect becomes very weak at integer values of ν_{spin} as \hat{n}_0 tilts strongly from the vertical in the arcs.

obtaining very small residual closed orbit deviations has been conquered for modern synchrotron radiation sources. Note that the closed orbit deviations remain small and the peak polarizations remain high even if a random sample of 20% of the monitors is taken out of service. In any case the sensitivity of the polarization to such small deviations shows that *it would be a false economy to skimp on good alignment of the ring, on the provision of correction magnets and on the precision of the beam position monitors*. One should also avoid stray fields from the proton ring and magnetic material in the beam pipe. Experience at HERA [19] supports this view.

Since the tilt of \hat{n}_0 is already small, harmonic closed orbit spin matching has not yet been applied. Perhaps with good enough alignment and corrections it would not be needed.

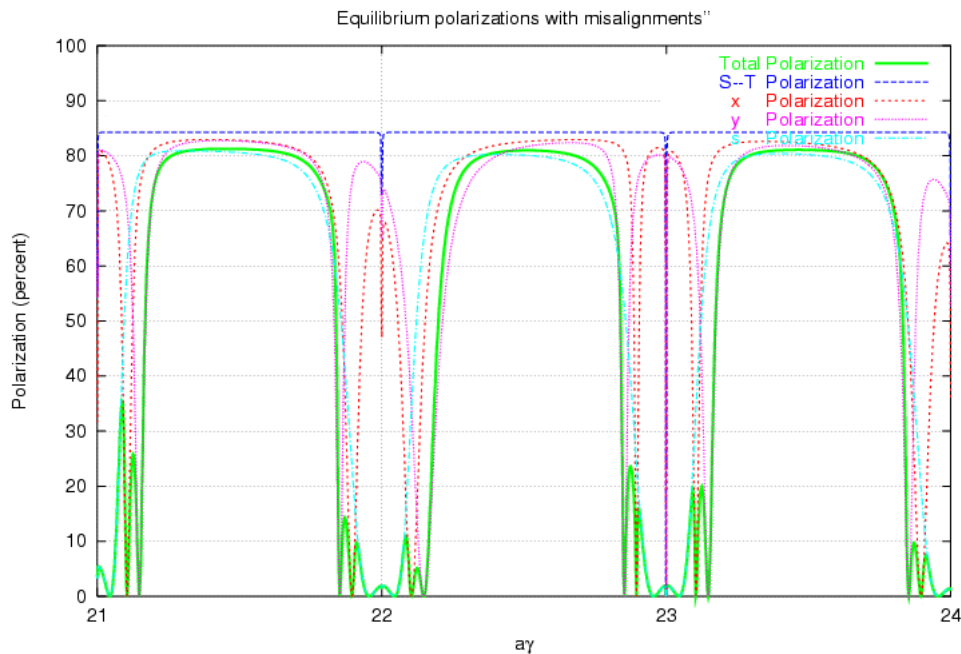


Figure 2.4.6- 3: The polarizations P_{bk} and P_{dk} and the polarizations associated with each of the three orbital modes when realistic imperfections are applied and the orbit is subsequently corrected.

The calculations carried out so far show that with linearized spin motion and in the absence of detector fields and beam-beam forces, both high equilibrium polarizations and reasonable τ_{dk} can be achieved around 10 GeV. Then operation with either self polarized e^\pm or with pre-polarized e^- would be comfortable. For the latter it would be necessary to avoid loss of polarization during injection. Note that in contrast to the injection of polarized protons into a ring, e^- are subject to stochastic depolarization as the beam reaches equilibrium.

Although the results from linearized calculations give strong grounds for optimism, a complete picture will only emerge once full spin motion has been included as well as other effects which have been neglected so far. Some next steps in this direction are discussed below. In the meantime it is important to note that 51% longitudinal e^+ polarization has already been achieved simultaneously at three interaction points at HERA at the almost three times higher energy of 27.5 GeV [25, 26].

To achieve high luminosity it will be necessary to mount quadrupoles inside the detector solenoid. These magnets will then be subject to large inter-magnet forces. Thus, special efforts should be invested in the stability of their mounts and the monitoring of their positions so that they do not cause excessive closed orbit distortion and resultant depolarization. Use should be made of experience with HERA [25].

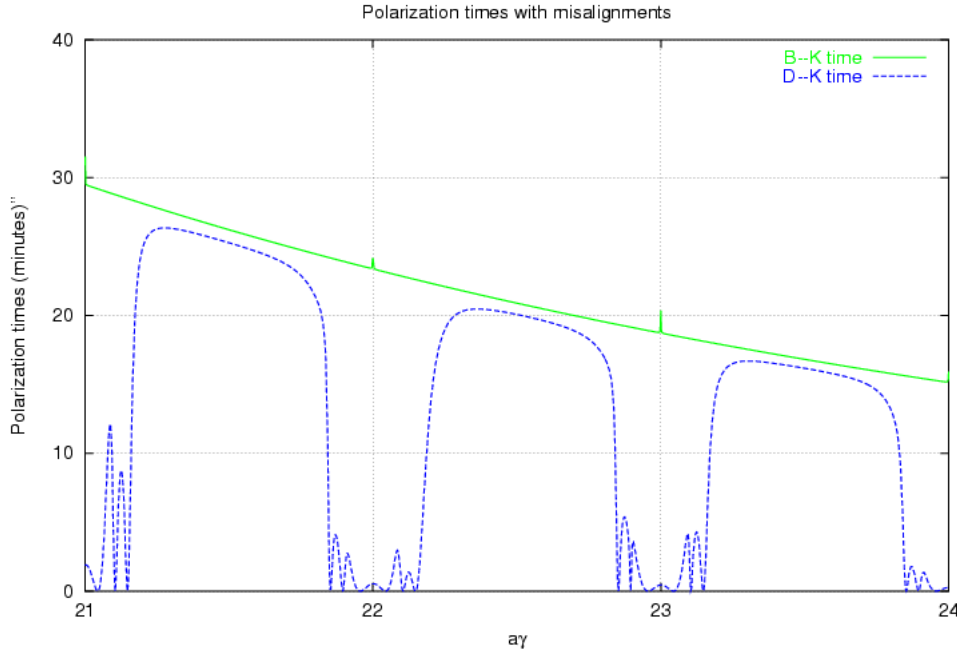


Figure 2.4.6- 4: The characteristic times τ_{bk} and τ_{dk} (minutes) for the simulation in figure 2.4.6- 3.

Some next steps

So far, it appears that with good orbit correction, harmonic closed orbit spin matching will not be needed. Nevertheless, this topic still needs to be thoroughly studied.

Since there is no simple way in standard optics software to represent the effects on the trajectories and the spins of the complicated overlapping fields of solenoids and quadrupoles, special spin-orbit maps for the interaction regions should be established. The calculations with SLICK should then be repeated using the linear parts of these maps to establish whether in linear approximation these combined fields have a significant influence on the spin transparency of the rotator section and on the polarization. The methods used for HERA could be adopted here [27, 26].

The calculations with linearized spin motion do not include the effects of higher order spin-orbit resonances. Thus, a next step will be to carry out class (ii) simulations with SLICKTRACK. This will, for example, give a picture of the strengths of the synchrotron sideband resonances and of whether there are advantages in choosing a special ν_s .

Even with misalignments the natural beam height will be very small. But as has been mentioned elsewhere, to reach high luminosity it will be necessary to increase the beam height. This might be achieved by, for example, running close to a transverse coupling resonance. Perhaps other methods

can be found. In any case experience shows that a proper picture of the polarization for such situations will require using a class (ii) simulation.

Class (ii) simulations are also essential for understanding the full effects of beam–beam forces on the polarization and the effects of non–linear orbital motion including the motion in the complicated fields in the detector.

Class (ii) simulations will also be necessary for evaluating the behavior of the polarization of a pre–polarized beam during injection.

Spin flip

As stated earlier, with the solenoid rotators the sign of the equilibrium longitudinal polarization can be changed by reversing the polarity of the solenoids. But this cannot be done while the beam is stored. However, it might still be possible to reverse the polarization on short time scales and without dumping the beam, by using resonant spin flip driven by an external radio frequency magnetic field. Note that after a reversal the polarization would return through zero to its original orientation with the characteristic time τ_{dk} . Resonant flipping of electron spins has been demonstrated at low energy [28] but it remains to be seen whether it is practical at the much higher energy of 10 GeV where spin diffusion might limit the efficiency [29, 30]. Class (ii) simulations will also provide insights here.

Further aspects of spin rotation

Although solenoid rotators have been chosen for eRHIC, dipole rotators can be kept in reserve.

The simplest kind of dipole rotator system involves just vertical bends which generate a Z shaped modification of the design orbit in the vertical plane [31, 32]. But the design orbit is then sloped at the interaction point and the detector which are just at the midpoint of the system. To reverse the sign of the equilibrium longitudinal polarization, the polarities of the vertical bends and the vertical positions of all the magnets w.r.t. the plane of the ring must be reversed. This in turn requires very flexible bellows between magnets and a mechanical jacking system for the whole interaction region including the quadrupoles very close to the detector.

A much more practical and economical solution is to use spin rotators consisting of strings of interleaved vertical and horizontal bends arranged so that they produce interleaved horizontal and vertical closed beam bumps. Such rotators stand apart from the detector and its nearby quadrupoles. According to the Thomas–BMT equation an orbit deflection of $\delta\theta_{\text{orb}}$ in a transverse magnetic field produces a spin rotation of $\delta\theta_{\text{spin}} = (a\gamma + 1)\delta\theta_{\text{orb}}$. Then at high energy small orbit deflections lead to large spin rotations and although the combined orbit bumps close, \hat{n}_0 can be rotated from vertical to longitudinal before the interaction point. A second rotator returns \hat{n}_0 to the vertical before the next arc. This is the scheme successfully used at HERA [19].

Some advantages and disadvantages of this second kind of dipole scheme are:

Advantages:

- The design orbit is horizontal in the detector and the nearby surrounding quadrupoles.

- By varying the fields and the geometry of the rotators the required rotation can be achieved for a range of energies. Then the polarization can be made essentially longitudinal at any energy in the design range.
- If the rotator is sufficiently short, it need not contain quadrupoles. It is then automatically essentially spin transparent.

Disadvantages:

- As in the case of the Z bend rotator, reversal of the sign of the longitudinal polarization requires the reversal of dipole polarities, very flexible bellows and a jacking system. But in this case only the rotators themselves need jacks, not the whole interaction region. Note that such a jacking system has been in service in HERA since 1994 [19].
- At low energy the relation $\delta\theta_{\text{spin}} = (a\gamma + 1)\delta\theta_{\text{orb}}$ implies that sufficient spin rotation can only be achieved with vertical orbit bumps that might be impractically large.
- Dipole rotators can decrease P_{bk} since \hat{n}_0 is not parallel to the field in most of the magnets. The decrease is most marked if the magnets are short ($\Rightarrow 1/|\rho|^3$ large) in order to save space.
- The generation of vertical emittance in the vertical bends can require strong vertical betatron spin matching [1].

Dipole rotators are best suited for high energy. But it is likely that for energies around 10 GeV or above, a dipole rotator with a tolerable vertical design orbit excursion could be designed for eRHIC.

If these dipole rotators contain no quadrupoles, spin matching involves making the straight sections between the rotators spin transparent for all three modes of motion and involves making the arcs between the rotators spin transparent for vertical motion [1, 19, 27].

References:

1. D.P. Barber, G. Ripken, Handbook of Accelerator Physics and Engineering, Eds.A.W. Chao and M. Tigner, World Scientific, 2nd edition (2001).
2. Articles by D.P. Barber (some with co-authors), in proceedings of ICFA workshop “Quantum Aspects of Beam Physics”, Monterey, U.S.A., 1998, World Scientific (1999). Also as DESY Report 98–96 and at the e-print archive: physics/9901038 – physics/9901044.
3. A.A. Sokolov, I.M. Ternov, Sov. Phys. Dokl. 8(12) (1964) 1203.
4. J.D. Jackson, “Classical Electrodynamics”, 3rd edition, Wiley (1998).
5. Ya.S. Derbenev, A.M. Kondratenko, Sov. Phys. JETP. 37 (1973) 968.
6. S.R. Mane, Phys. Rev. A36 (1987) 105–130.
7. G.H. Hoffstaetter, M. Vogt, D.P. Barber, Phys. Rev. ST Accel. Beams 11 (2) 114001

- (1999).
8. D.P. Barber, G.H. Hoffstaetter, M. Vogt, Proc. 14th Int. Spin Physics Symp., AIP Proc. 570 (2001).
 9. V.N. Baier, V.M. Katkov, Sov. Phys. JETP. 25 (1967) 944.
 10. V.N. Baier, V.M. Katkov, V.M. Strakhovenko, Sov. Phys. JETP. 31 (1970) 908.
 11. J. Kewisch et al., Phys.Rev.Lett. 62(4) (1989) 419. The program SITF is part of the SITROS package.
 12. D.P. Barber. SLICKTRACK is the version of SLICK [15] which includes Monte-Carlo spin-orbit tracking.
 13. A.W. Chao, Nucl. Inst. Meth. 180 (1981) 29.
 14. A.W. Chao, AIP Proc. 87 (1981) 395.
 15. SLICK is a thick lens version of SLIM by D.P. Barber. Private notes (1982).
 16. K. Yokoya, User's manual of SOM: Spin-Orbit Matching (1996).
 17. C.W. de Jager, V. Ptitsin, Yu.M. Shatunov, Proc. 12th Int. Symp. High Energy Spin Physics, World Scientific (1997).
 18. K. Yokoya, KEK Report 92-6 (1992).
K. Yokoya, DESY Report 99-006 (1999)
and at the e-print archive: physics/9902068.
 19. D.P. Barber et al., Phys. Lett. 343B (1995) 436.
 20. S.R. Mane, Nucl. Inst. Meth. A292 (1990) 52.
S.R. Mane, Nucl. Inst. Meth. A321 (1992) 21.
 21. A.A. Zholents, V.N. Litvinenko, BINP (Novosibirsk) Preprint 81-80 (1981). English translation: DESY Report L-Trans 289 (1984).
 22. D.P. Barber et al., DESY Report 82-76 (1982). Note that in that paper, the symbol \vec{n} should be replaced with \vec{n}_0 to correspond with modern notation.
 23. D.P. Barber et al., Particle Accelerators 17 (1985) 243. Note that in that paper, the symbol \vec{n} should be replaced with \vec{n}_0 to correspond with modern notation.
 24. V. Ptitsyn et al., Proc. 2003 IEEE Particle Accelerator Conference (PAC2003), Portland, U.S.A., (2003).
 25. F. Willeke et al., Proc. 2003 IEEE Particle Accelerator Conference (PAC2003), Portland, U.S.A., (2003).
 26. D.P. Barber, E. Gianfelice-Wendt, M. Berglund, Physics World, July 2003.
 27. G.Z.M. Berglund, Ph.D. thesis, DESY-THESIS-2001-044 (2001).
 28. V.S. Morozov et al., Phys. Rev. ST Accel. Beams (4) 104002 (2001).
 29. D.P. Barber et al., Proc. 11th Int. Symp. High Energy Spin Physics, AIP Proc. 343 (1995).
 30. K. Heinemann, DESY Report 97-166 (1997) and at the e-print archive: physics/9709025.
 31. R. Schwitters, B.Richter, SLAC PEP Note 87 (1974).
 32. J. Buon, Nucl. Inst. Meth. A275 (1989) 226.

2.4.7 RF System for the Storage Ring

Choice of Operating Radio Frequency

The choice of RF operating frequency is strongly influenced by practical considerations. First, the requirement for a storage-ring RF cavity having a large aperture, as discussed in the following, limits the choice to a small band of frequencies, between 300 and 500 MHz, for which high-power klystron RF amplifiers are commercially available. Second, the electron-ring operating frequency must be harmonically-related to the eRHIC colliding-frequency.

The highest practicable frequency is preferred in B-factory application, where high bunch-numbers and short bunch-lengths are desired for maximum luminosity. In this application, however, the bunch-number in the ring is determined by the collision frequency, and the electron bunch-length is much shorter than the ion-beam bunch length, by which the minimum β^* at the interaction point is set.

Nevertheless, higher operating frequency is still favorable for reasons such as longer Touschek lifetime, and cost-effectiveness of longitudinal focusing. The frequency, therefore, is chosen to be at the upper-end of available klystron technology. For the room-temperature, copper-cavity option, it is 478.57 MHz, the 17th harmonic of the collision frequency. For the super-conducting cavity option, it is 506.723 MHz, the 18th harmonic of the collision frequency.

Choice of RF Cavity Type

The choice, for the type of RF cavity to use in the electron-ring system, is between cryogenic superconducting and room-temperature copper. A superconducting system has the capability of producing the requisite accelerating RF gap voltage with fewer cavities. This is important in terms of the coupled-bunch instability impedance, which is driven by the higher-order-mode (HOM) RF fields in the cavities. The HOM is proportional to the number of cavities. The number of cavities is determined by the power-handling capability of the RF input coupler. The RF power required is determined by beam loading, or the amount of input power delivered to the accelerated beam. With superconducting cavities virtually all of the input power is delivered to the beam, whereas with room-temperature cavities about one-third of the input power will be dissipated in the cavity walls. Therefore, the number of superconducting cavities can be one-third fewer than the number of room-temperature cavities. The use of superconducting cavities introduces a technological challenge: how to remove the hundreds of kilowatts of HOM power induced in the cavities by the high-current beam. The solution to this problem, for room-temperature cavities, has been demonstrated by the SLAC B-factory. The choice of cavity type is based on the high performance of the high-luminosity, high-current SLAC B-factory, using a conventional room-temperature RF system.

Room Temperature RF Cavity Design

The RF cavity design challenge is to determine the optimum cavity geometry, which simultaneously maximizes the cavity shunt impedance, at 478.57 MHz, which is important for efficient beam acceleration, while minimizing the longitudinal and transverse shunt impedances at the higher-order modes (HOM), which is important for beam stability. The high average beam current of the electron

ring, with beam in a large number of RF buckets, makes the minimization of HOM shunt impedances crucial to successful operation.

The cavity geometry for the eRHIC must provide for a large aperture, through which HOMs are coupled from the cavity into the beam pipe. The cavity profile must be consistent with maximizing the separation between the TM₀₁₀ fundamental mode, at 478.57 MHz, and the next lowest azimuthally-symmetric (monopole) transverse magnetic (TM) modes. All of these TM modes, other than the TM₀₁₀, and all cavity dipole modes are above the corresponding mode cut-off frequencies in the beam pipe.

To minimize HOM impedance, the number of cavities must be minimized, and they must be single-cell, rather than multiple-cell, the type used in PETRA/DESY. As a consequence, the single-cell cavities must operate with higher voltage gradient to produce the required gap voltage and power delivered to the beam.

Optimization of cavity geometry will require a series of computations which analyze cavity modes as a function of cavity shape, making use of the RF computer codes URMEL-Tcode (triangle-mesh version) and Superfish, and analysis of cavity temperature-profiles and thermal-mechanical stress, at nominal dissipated RF power, using MAFIA, in a thermal model, with ANSYS code.

A cavity shape similar to that of the SLAC B-factory, can be used, as shown in Figure 2.4.7-1. The RF system can meet all requirements using 10 klystrons, driving 20 cavities, in the electron ring for eRHIC. The RF system parameters are summarized in Table 2.4.7-1.

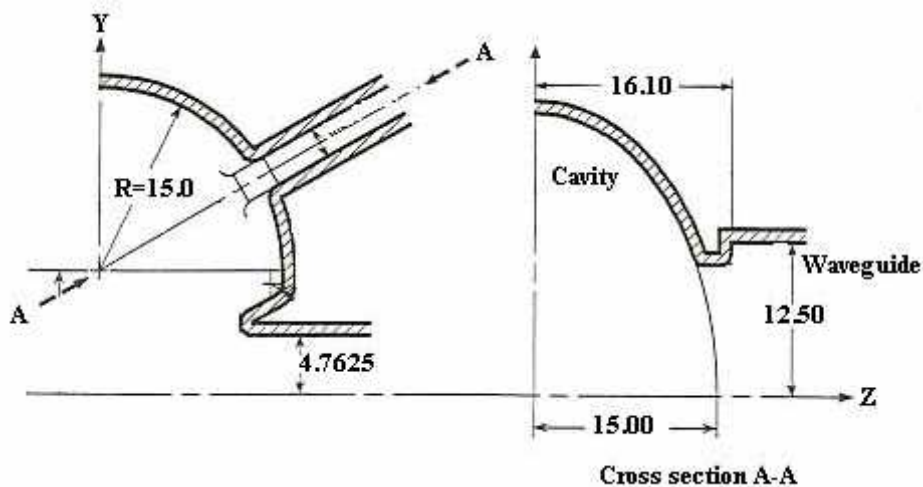


Figure 2.4.7-1 Schematic of a quadrant of the SLAC B-Factory (dim are cm).

RF Operating Frequency	478.57 MHz
Harmonic Number	2040
Gap Voltage, V	25 MV
Beam Current, I	450 mA
Energy Loss/Turn	11.7 MeV
Shunt Impedance/Cavity, R_s	3.5 M Ω
Number of Klystrons	14
Number of Cavities	28
Accelerating Voltage Gradient	4.15 MV/m
HOM Power (est)	100 kW
Wall Loss/Cavity	122 kW
Coupling Factor, β	1-9
Unloaded Q	30,000

Table 2.4.7-1: Electron-Ring RF System Parameters

Higher-Order Mode (HOM) Damping

In the design of accelerating cavities it is customary to maximize the shunt impedance in the fundamental mode, which maximizes the RF accelerating voltage gradient as a function of RF input power. However, in many storage rings, parasitic effects, such as the decelerating and deflecting fields arising from higher-order modes, and the transient-wake forces inside an electron bunch, can have serious cumulative effects that limit the achievable charge-per-bunch to a value well below the fundamental beam limit. In order to evaluate the overall performance of an accelerating system, including the parasitic effects, high-level computational means are required, which include the computer codes MAFIA, URMEL and ARGUS.

Two major cumulative effects are to be considered early in the design of the HOM coupler. These are the multi-bunch instabilities caused by resonant higher-order modes in the cavities, excited by the beam, and single-passage effects due to the wake-fields excited by the beam during its transit of a cavity (e.g. head-tail turbulence, bunch lengthening, and synchro-betatron resonances).

The most important performance goals in the design of a HOM damping system are broad bandwidth and the suppression of coupling to the fundamental cavity mode. Coaxial dampers are used in both normal and super-conducting particle-accelerator cavities. Aperture-coupled hollow waveguide dampers are used in multiple, usually three, to damp the degenerate mode. Suppression of coupling to the fundamental mode is provided by the cutoff characteristic of the waveguide.

The feasibility of obtaining high charge-per-bunch has been demonstrated by the SLAC B-factory RF system. An important feature of the B-factory RF system is an extremely unique waveguide HOM-damper system. It is likely that a design similar or identical to this will be chosen, due to its state-of-the-art status and present availability.

Tuner and Adjustable RF Coupler

To accommodate the high average power dissipation and wide range of beam-loading conditions, associated with the storage mode of operation, cavity tuning and coupling systems with considerable adjustability are required. The design requirements for the tuner and RF coupling systems are given in Tables 2.4.7-2,3, respectively.

Cavity Frequency	478.57 MHz
Frequency Range	3.0 MHz
Travel Range	12 cm
Tuning-Angle Precision	+/- 0.5 Deg.

Table 2.4.7-2: Cavity Tuner Specifications

Design RF Power	500 kW
Input Line	WR-2100 Waveguide
Input VSWR	1.5:1
Coupling Factor	Adjustable up to 10

Table 2.4.7-3: RF Coupling System Characteristics

Tuner Design

A cavity tuning range of 2 MHz is adequate to accommodate the expected detuning caused by beam loading effect and for frequency shift caused by thermal expansion of the cavity body, a function of RF power dissipation. Additional tuning range is required, however, to compensate for frequency shifts, as much as 200 kHz, resulting from changes in RF coupling to the cavity, and as much as 340 kHz resulting from collision frequencies for different proton (ion) energies. Consequently, the tuner is designed for greater than 2.5 MHz, centered about 478.57 MHz. A cross-sectional view of the cavity, in the plane of the tuner, is shown in Figure 2.4.7-2.

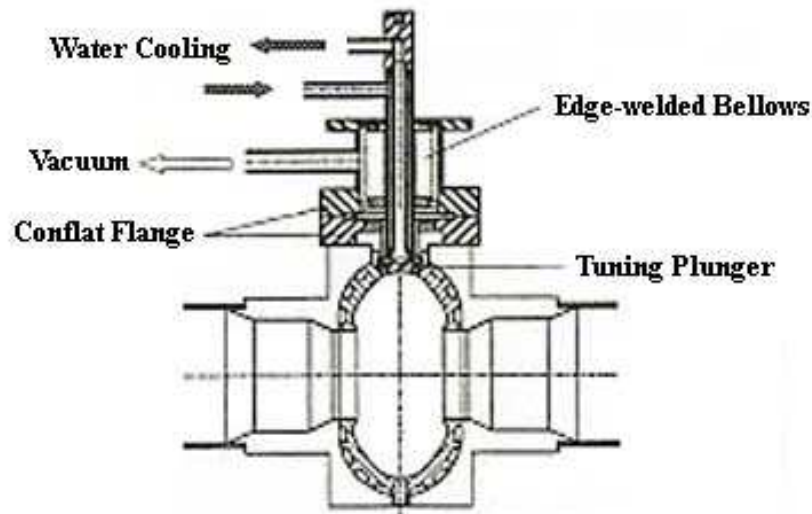


Figure 2.4.7-2: Cross section of cavity and tuner

Input RF Coupler Design

There are two types of input coupling that are appropriate for use at the 500 kW power level. The first is a rotatable loop, terminating a coaxial drive line, introduced at the cavity wall, having a coupling factor, β , adjustable between 1 and 10. The ceramic coupling window must be shielded

from the direct path of ions produced by the beam traversing the cavity. The other type of coupling is by means of an aperture. The design procedure begins with an aperture with a coupling factor of 10, and then the means of reducing the coupling factor without producing significant change in the frequency of the fundamental cavity mode (TM₀₁₀). Such a means is a capacitive post, of adjustable depth of penetration, located at the first electric-field minimum of the standing-wave present in the drive-line waveguide. Such a coupler has been successfully designed, fabricated, and operated in the storage ring of the MIT Bates linear accelerator, as shown in Figures 2.4.7-3,4.

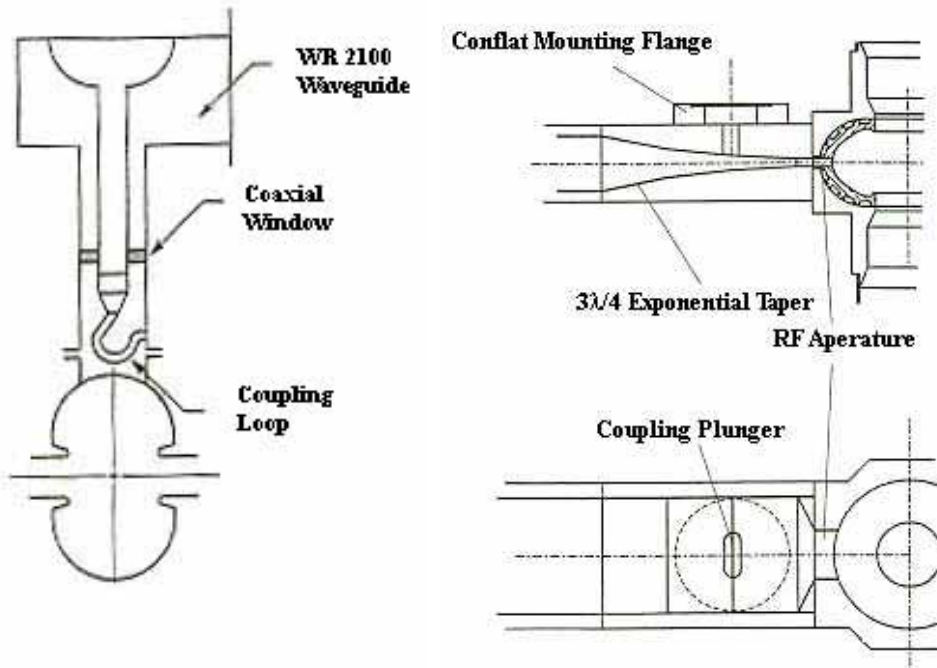


Figure 2.4.7-3 Coaxial Coupling Network

Figure 2.4.7-4 RF input waveguide and Aperture Control

Cavity Window

The cavity window must be capable of the transmission of 500 kW incident power and the RF voltage associated with the standing wave produced by significant reflected power. A coaxial ceramic-disc window, similar to the type used in the SLAC B-factory, is being designed to handle the thermal stress associated with the transmission of up to 2 MW of RF power.

High-Power RF Distribution

The high-power RF distribution system is implemented in WR-2100 rectangular waveguide, consistent with low-loss transmission of 1.2 MW CW, at 478.57 MHz. The output of each klystron is split, by means of a 3-dB, quadrature, high-power hybrid, chosen for superior power-handling capability, and directed to the inputs of two accelerating cavities. The path length from one of the two hybrid outputs is corrected by one-quarter wavelength, to compensate for the 90-degree phase-shift between hybrid outputs, producing in-phase signals at the two cavity inputs. The path between klystron output and hybrid input includes a load-isolator in the form of a four-port, differential-phase-shift, ferrite circulator. This produces a nominally matched-load condition for the klystron, enhancing

its operational stability, regardless of reflections from the cavities. To the extent that the cavity voltage (or current) reflections are matched in amplitude and phase, all of the reflected power will be dissipated in the waster load of the circulator. To the extent that the reflections are mismatched, in amplitude and phase, the reflected power will be shared by the waster load of the hybrid junction (the limiting case is equi-amplitude, quadrature-phase reflections, where all reflected power is directed to the hybrid load).

Both high-power klystrons and high-power circulators (both forward and reverse power), at 1.2 MW CW and 478.57 MHz, are within the range of commercial availability.

Low-Level RF Control System For Room-Temperature Cavities

The low-level RF control system comprises four feedback loops, as listed in Table 4, consistent with the general system performance specifications.

The overall configuration of the control loops is shown in figure 5. The gain of the klystron power amplifier is regulated by the innermost loop, which compares the input and output power levels of the klystron. The variable-attenuation capability of a PIN-diode RF modulator, inserted in the klystron input line, is used to compensate for gain changes in the klystron. A digital phase-shifter is the transducer, connected in the klystron drive line, which responds to error-signals from the phase-comparator to maintain constant transmission-phase across the klystron. Together, these two loops regulate complex klystron gain, so that the stability and performance of the cavity-voltage loop are not perturbed by parameter variations such as klystron cathode voltage and RF drive power.

The cavity resonant frequency is maintained constant by positioning a cavity tuning plunger in response to an error signal generated by comparing the phase of the RF input to the cavity with the phase of the cavity gap voltage. Cavity voltage is also down-converted in a quadrature mixer (vector demodulator and modulator), using a 478.57 MHz reference signal. The resulting in-phase (I) and quadrature (Q) signals are processed in video-bandwidth electronics, up-converted using the same 478.57 MHz reference signal, and applied to the RF drive line. The sensitivity of the down/up conversion process to variations in the amplitude of the reference signal are minimized by the use of automatic level control (ALC) prior to the mixers. The signal processing is accomplished by means of Bitmus-equipped computers, as shown in the block-diagram of the low-level RF system, Figure 2.4.7-5.

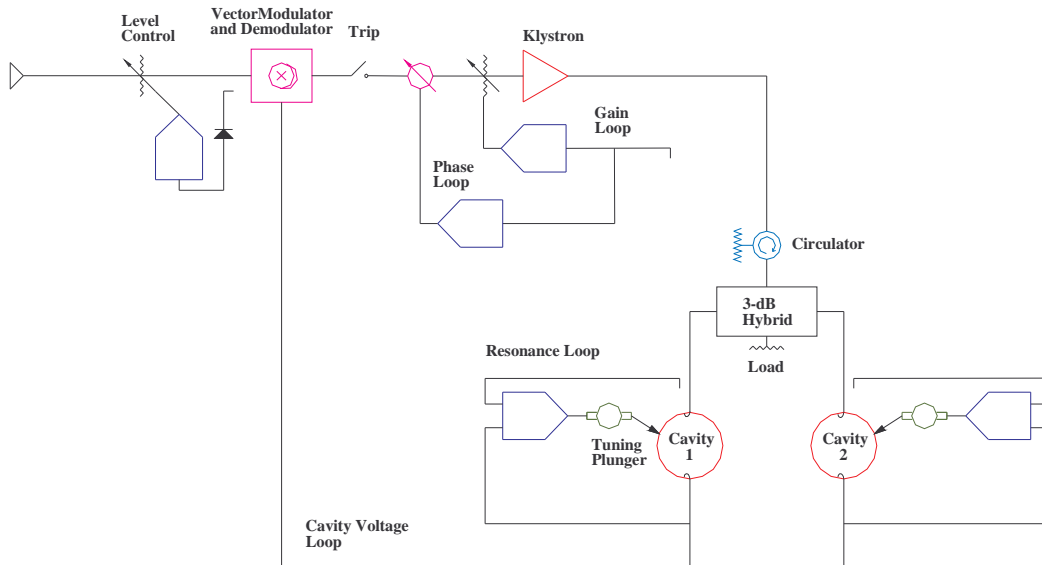


Figure 2.4.7-5: Block diagram of the low level RF system

Loop	Regulated Variable
Voltage	Cavity Voltage (Amplitude and Phase)
Resonance	Cavity Resonant Frequency
Gain	Klystron Transmission Gain
Phase	Klystron Transmission Phase

Table 2.4.7-4: Feedback Loop Function

Superconducting (SC) RF Cavity Design

The design objectives for SC cavities are no different than for room-temperature cavities: maximize the impedance and voltage gradient of the accelerating mode while minimizing the impedances for higher-order modes (HOMs). SC cavities have the advantage of high voltage-gradient (on the order of 10 MV/m, which is significantly greater than that of room-temperature cavities) and much higher values of unloaded Q , due to the greatly diminished surface losses. The high accelerating gradient allows the design of an accelerator with fewer cavities and gaps, which ameliorates the HOM problem and diminishes the sensitivity to coupled-bunch instability, just as in a room-temperature design.

The high unloaded Q permits cavity geometry with large-aperture beam holes, since R/Q is not critical, allowing HOMs to be coupled out into the beam pipes, where absorptive material can be deployed. Single-cell, spherical designs are attractive, minimizing the number of HOMs and the required RF input-coupler power-handling capability. Each cavity is powered by its own RF source, through a load-isolating ferrite circulator, also obviating an RF distribution system. The same computer programs which aid in the design of room-temperature cavities are appropriate for the optimization of SC cavities, as the same cavity parameters are important in both cases. A Cryomodule for a superconducting cavity with HOM-ferrite absorber is shown in Figure 2.4.7-6.

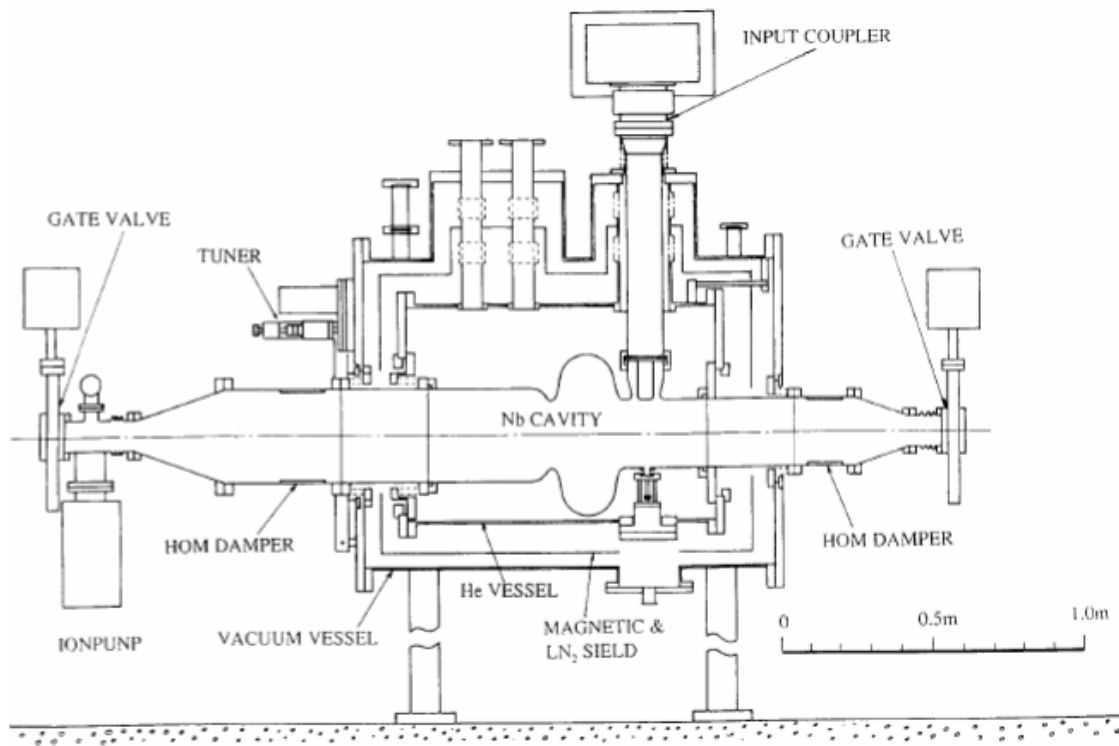


Figure 2.4.7-6: Superconducting Cavity Module KKB Factory

The RF system parameters, for an electron ring using KEKB SC cavities, are given in Table 2.4.7-5.

RF Operating Frequency	506.723 MHz
Harmonic Number	2160
Gap Voltage, V	25 MV
Beam Current, I	450 mA
Energy-Loss/Turn	11.7 MeV
R/Q	93 Ω
HOM Power (est.)	20 kW
Accelerating Voltage Gradient	~ 10 MV/m
Unloaded Q	1×10^9
Number of Cavities	13
Number of MVEDs (Klystron or IOT)	13
Cryostat LHe Volume at 4.2 K	290 Liters
Static loss per Cryomodule at 4.2K	31 W

Table 2.4.7- 5. Electron Ring (Superconducting Cavities) RF System Parameters

Higher-Order Mode (HOM) Damping

Major design issues, for a high-current accelerator, are the nature of the HOM dampers, how to remove the heat produced by the absorbed power (cryostat load) and out-gassing by the absorptive material (ion-pump load). Success has been achieved using ferrite damping material, in the shape of thin cylinders, brazed or sintered to the inside walls of the beam pipes, adjacent to the accelerating cavities. In addition, the location and geometry of the HOM dampers, which affect HOM RF field distribution in the absorptive material, power-density and temperature-rise profiles, and other characteristics, must be optimized.

Low Level RF Control System for SC Cavities

The extremely high Q and narrow bandwidth of SC cavities, compared with ambient-temperature copper cavities, causes phase and amplitude characteristics to be affected to a much higher degree by dimensional perturbations. The design of the low-level RF control system is particularly challenging, therefore, for the following reasons. First, mechanical deformation of the cavities, due to Lorentz Force, will cause cavity detuning by an amount greater than one bandwidth. Second, regardless of the required pre-detuning, in the absence of beam, the cavity resonant frequency will be modulated by unavoidable microphonically-induced mechanical forces. Third, higher stability, in the control of phase and amplitude will be required, with amplitude stability on the order of 10^{-4} and phase stability of 0.5 degrees.

The cavity resonant frequency is maintained constant by driving a Piezo-electric actuator, within each cavity, in response to an error signal generated by comparing the phase of the cavity rf input with the phase of the cavity gap voltage. Cavity voltage is also down-converted, in a quadrature mixer (vector demodulator and modulator), using a 506.723 MHz reference signal. The resulting in-phase (I) and quadrature (Q) signals are processed in video-bandwidth electronics, up-converted using the same 506.723 MHz reference signal, and applied to the RF drive line, to maintain klystron transmission gain and phase. The sensitivity of the down/up conversion process to variations in the amplitude of the reference signal is minimized by the use of automatic level control (ALC) prior to the mixers. The RF control block diagram for superconducting cavity is shown in Figure 2.4.7-7.

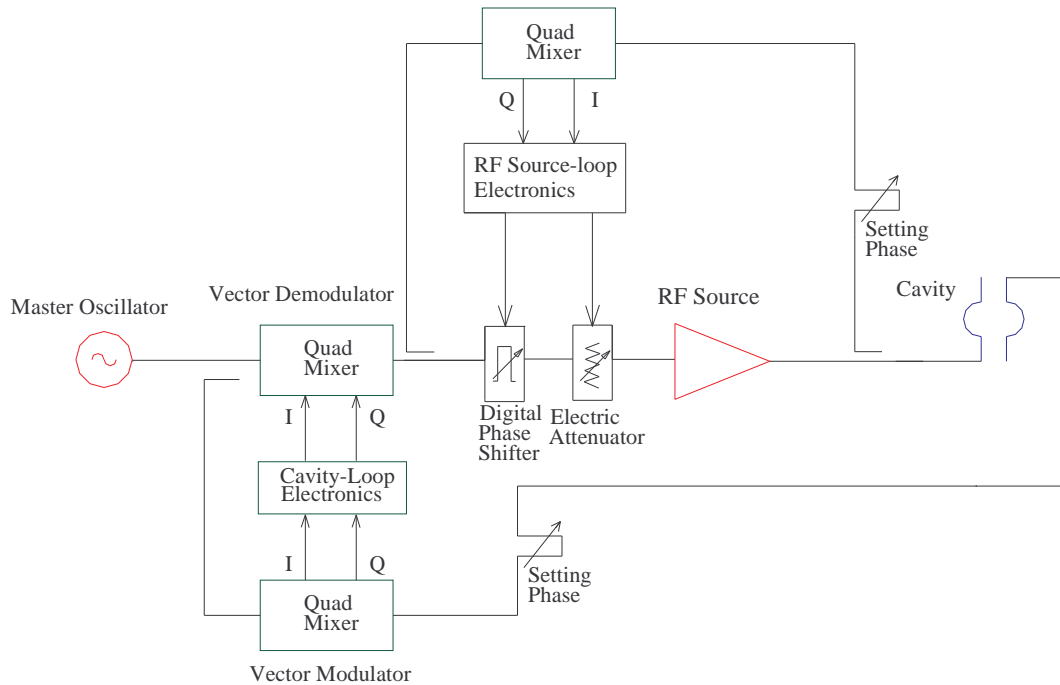


Figure 2.4.7-7: The RF control block diagram for superconducting cavity

CW RF Power Amplifier

Microwave Vacuum Electron Device (MVED) Considerations

High-power multi-cavity klystrons, capable of 1.2 MW, CW, are available from EEV, Thales, Phillips and Toshiba, but must be modified for operation at either 478.57 MHz, or 506.723 MHz, and for extended bandwidth, consistent with group-delay on the order of 100 ns. A klystron, of SLAC/CPI collaborative-design, produces 1.2 MW at 478.57 MHz, with DC beam input of 2 MW (beam voltage of 84 kVDC and beam current of 24 A), for a conversion efficiency of 60%.

DC Power Supply System

In its simplest form, the electrical part of a CW RF source is an MVED and a DC power supply. Again, the optimum (least complicated, most reliable, highest efficiency) form of such a power supply is the line-frequency, poly-phase, full-wave (typically 12-pulse) transformer-rectifier. The DC energy-storage requirements are determined by the required ripple-reduction factor, and can be either in the form of inductive or capacitive storage, or a combination of both.

Protection of the high-power MVED from internal damage resulting from the discharge of energy and electrical charge stored in shunt filter capacitance, by an electron-gun arc, is always an issue. Many RF systems, especially at MW power levels, use a triggered shunt charge-diverter, called an “electronic crowbar” for protection. The low-impedance “crowbar” diverter cannot dissipate stored energy itself, and is therefore used in conjunction with resistance, in series with the MVED cathode,

which can. This resistance also limits peak fault current, but also must dissipate continuous power during normal operation. With short-circuit current limited by resistance, the energy dissipated in the electron-gun arc is directly proportional to the total charge transport, since the voltage drop of the arc (on the order of 20 V.) is nearly constant, regardless of current amplitude (up to several thousand amperes). If stored charge is less than one Coulomb, series resistance alone can provide adequate protection, since it will dissipate all but a tiny fraction of the stored energy. Often the short-circuit “follow-on” current from the transformer-rectifier, limited by total leakage reactance to approximately 10 times normal current, will produce a greater amount of charge transport, unless it is interrupted at the first zero-crossing (1/2 cycle) by high-speed, solid-state (SCR) switchgear. In many cases, an SCR primary phase-shift voltage controller also provides the high-speed interrupt. The latest of protection means is the high-voltage, solid-state, IGBT DC-interrupting switch, in series with the MVED cathode, supplanting all other forms of protection, with insignificant charge let-through and the capability of short-duration automatic reset. Presently it is also the most expensive means of protection.

References:

1. KEKB B Factory Conceptual Design Report
2. SLACB PEP-II “An Asymmetric B-factory”, Conceptual Design Report 1993
3. Shin-Ichi Kurokawa” Status of KEKB Project”
4. A. Zolfaghari et al. “Bates South Hall Ring RF Control System” 1993
5. A. Zolfaghari et al. “Design of a tuner and adjustable RF Coupler for CW 2856 MHz RF Cavity” 1991

2.5 Electron Polarimetry

The First Electron Beam Polarimeter Workshop at BNL was held on November 8, 2002 [1]. Representatives from five laboratories participated in discussions of polarimetry for an electron-ion collider. This section is based on discussions held during and following the workshop on important questions related to eRHIC polarimetry. Since a detailed design for a beam polarimeter has yet to be formulated, this section emphasizes items which require significant development or careful consideration in the design of the electron accelerator and ring.

2.5.1 Introduction

Accurate measurements of the electron polarization are essential for the experimental program at eRHIC. Measurements will be provided by polarimeters which can be separated into two categories: those which determine the beam polarization prior to injection into the electron storage ring, and those which monitor the beam polarization during storage. These two types of polarimeters provide complementary information valuable for optimizing the electron polarization and minimizing systematic errors.

The initial polarization will be established by measurements performed in the polarized source and accelerator through a combination of methods. Because the ring will be filled only infrequently, the use of methods which are destructive to the beam is acceptable in the linac. One possible scenario would include a low energy polarimeter monitor the polarization from the polarized source on a continuous basis. This can be accomplished through the well-known technique of Mott polarimetry [2] or other promising methods[3,4]. The polarization should also be periodically measured following acceleration. This can be accomplished efficiently by a Moller polarimeter which stops the beam or samples some fraction of it. Such devices are in use for highly energetic external beams at several other labs including SLAC [5] and Jefferson Lab. Overall, it should be possible to determine the electron polarization prior to injection very accurately. Details of linac polarimetry are not discussed in this report.

Because the polarization in the ring changes dynamically, it is essential to have accurate polarization measurements for the stored electron beam as a function of time. The polarization build-up time and equilibrium polarization due to synchrotron radiation has been calculated for the eRHIC design and it is essential to be able to compare to measurements to ensure that optimal performance is being achieved. It will also provide the only determination of polarization for positron beams, which will be initially unpolarized. An efficient polarimeter will provide important feedback for beam tuning in minimizing the effects of depolarizing resonances. A fast polarimeter also allows consideration of an adiabatic spin flipper for the eRHIC ring [6].

Polarimeters for the storage ring must employ a mechanism which is nondestructive to the beam. A proven method meeting this criterion is that of laser back-scattering, which entails Compton scattering of laser photons from the stored beam. This method is based on the coupling between electron (or positron) polarization and circularly polarized photons in the Compton scattering cross section. Compton polarimetry can be used to determine both longitudinal and transverse components of the beam polarization. Longitudinal polarimetry relies on the measurement of an asymmetry as a

function of the backscattered photon energy. Transverse polarimetry relies on the measurement of an azimuthal asymmetry with respect to the electron momentum in the backscattered photon flux.

At eRHIC, a longitudinal polarimeter will be located between the spin rotators in the electron-ion Interaction Region, thereby directly measuring the quantity needed for experiments. A second polarimeter in the eRHIC electron ring, located outside the spin rotators where the polarization is predominantly perpendicular to the circulation plane will measure the transverse polarization, thereby providing a consistency check which is independent of the spin rotators. This technique has been successfully employed at the HERA electron-proton collider [7,8,9], where complementary information provided by two independent polarimeters has provided important consistency checks and improved the accuracy of both measurements. A proposed layout for eRHIC polarimeters is shown in Fig. 2.5-1.

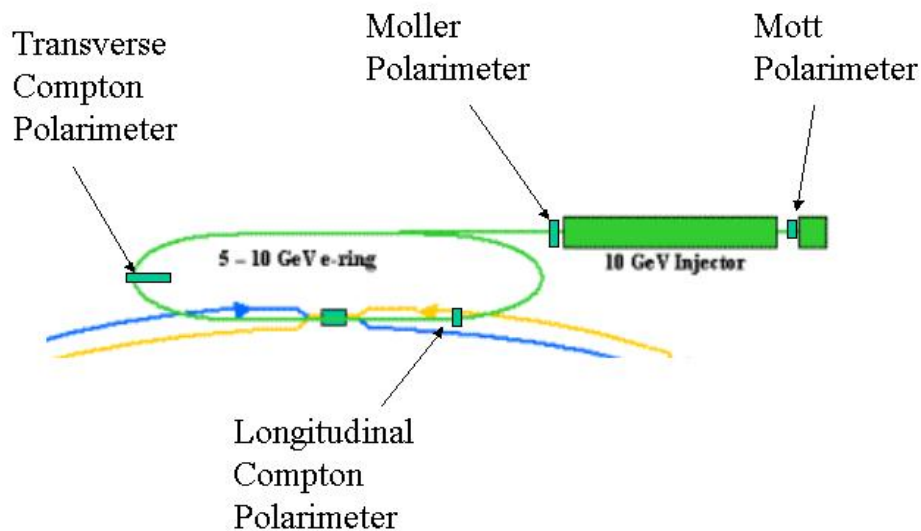


Figure 2.5 -1: Proposed locations for electron polarimeters at eRHIC.

Compton polarimetry is very effective in high energy electron storage rings for several reasons. The electromagnetic interaction can be modeled well, allowing an accurate determination of the absolute analyzing power of the polarimeter. The analyzing power for Compton scattering rises with electron energy, thereby improving the attainable statistical and systematic accuracy. In addition, increasing the energy of the electron beam also boosts the energy of backscattered photons and focuses them into a narrower kinematics cone. Both improve the ratio of signal to background, an essential consideration due to the very high intensity of eRHIC beams. Narrowing the cone of scattered photons reduces the size of detector needed. Higher energy photons can be more readily separated from the bremsstrahlung background, which is also focused in the beam direction. The electron energy at eRHIC, assuming a range of 5-10 GeV, will be sufficient to allow for accurate polarization measurements. Compton polarimeters in the Amsterdam Pulse Stretcher Ring at NIKHEF [10] and the South Hall Ring at MIT-Bates [11] have been successfully built and operated for high precision polarization experiments. Jefferson Lab [12] has also successfully operated Compton polarimeters for external beams at lower energies than eRHIC will operate.

As shown schematically in Fig 2.5-2, each Compton polarimeter at eRHIC will feature a laser system, an interaction region for the laser and electron beam, and a detector for products of Compton scattering, either backscattered photons or Compton scattered electrons.

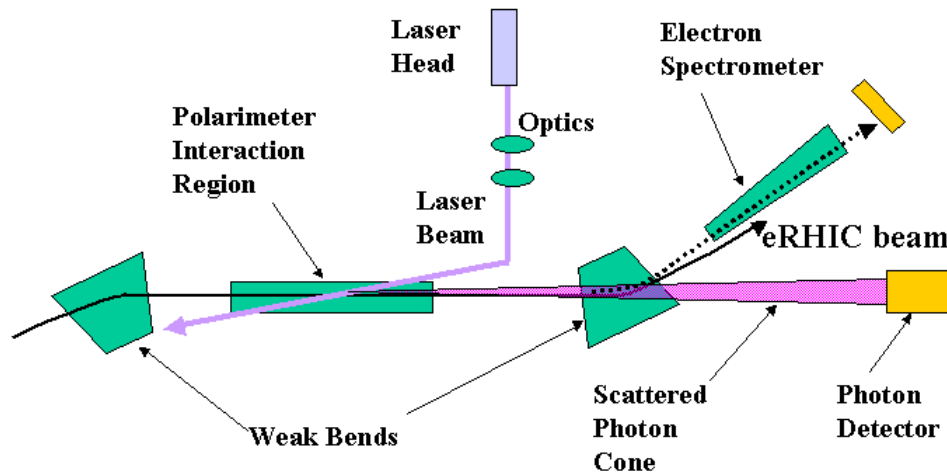


Figure 2.5-2: Schematic view (not to scale) of Compton polarimeter for eRHIC.

While details will differ, many issues are common to longitudinal and transverse polarimetry. An overview of questions related to each of these systems is presented in the remainder of this section, with primary consideration given to the identification of issues potentially affecting design of the ring. The section concludes with a discussion of the statistical and systematic accuracy which could be expected for these types of polarimeters.

2.5.2 Electron beam

The design of the polarimeter will be governed by properties of the electron beam. To accurately sample the beam polarization, the interactions between laser and electron beams for the Compton polarimeters must be placed in straight sections of the eRHIC ring. In these regions, accurate diagnostics and controls for the electron beam trajectory are essential. To a high degree, the electron trajectory defines the momentum direction of backscattered photons. This places a premium on electron beam, particularly in the transverse polarimeter. The location of this device is planned for a 3-m long straight section in the east arc of the ring. The longitudinal polarimeter must be placed in the south straight section downstream of the electron-ion interaction point.

A complicating factor for the longitudinal polarimeter placement is the rapid spin precession of the electron beam when it is polarized in the plane of the ring, as is the case between the spin rotators. The spin precession angle is directly proportional to the bending angle and for a 10 GeV beam, a bend of 1 degree will rotate the spin by nearly 25 degrees. Because the detector includes a magnetic field, the longitudinal projection of the beam polarization will precess as the electron beam is extracted from the electron-ion IP. To compensate for this effect, a weak bend will be introduced upstream of the polarimeter to rotate the spin back to its orientation at the collision point. Once again, very good local diagnostics are necessary to constrain the beam trajectory and minimize systematic uncertainties in the polarization measurement due to spin precession.

The use of short straight sections should aid in the minimization of background. This is a particularly important consideration in eRHIC where the intense beam will generate copious quantities of bremsstrahlung photons. Bremsstrahlung is likely to be the dominant source of background, as its angular distribution is peaked in the same direction as that of backscattered photons. In addition to reducing the efficiency of the measurement, excessive fluxes of bremsstrahlung photons can cause additional problems such as damage to ring vacuum windows. Minimization of bremsstrahlung can be achieved through a combination of vacuum optimization and reduction of the length of the polarimeter's interaction region. The interaction regions should be limited to a few meters in length.

Other considerations related to the electron beam concern focusing. Focusing the electron beam at the interaction point improves the statistical accuracy of the polarization measurement. The beam size should be considered carefully though, as very strong focusing of the electron beam introduces divergence into the backscattered flux, thereby diminishing the correlation between position and energy needed for transverse polarimetry. Typical beam sizes in existing Compton polarimeters are of the order of a few tenths of a millimeter with divergence of the order of tens of microradians.

2.5.3 Laser system

The design of the laser system is another important element in the design of the Compton polarimeters. Multiple criteria merit consideration in the selection of the laser including wavelength, power, emittance, stability, and pulse structure. The laser optics, particularly in the interaction with the electron beam must also be considered carefully in the interaction region design.

The spectrum of gamma rays produced by Compton scattering will have an endpoint energy directly proportional to the energy of incident photons. Maximizing the endpoint energy in the backscatter spectrum is desirable to increase the asymmetry and improve the signal-to-background ratio. In this respect, the relationship between laser wavelength and scattered photon energy strongly favors the use of a short wavelength laser in or near the ultraviolet region. Fig 2.5-3 shows the longitudinal analyzing power as a function of scattered photon energy for lasers at 266 nm and 532 nm.

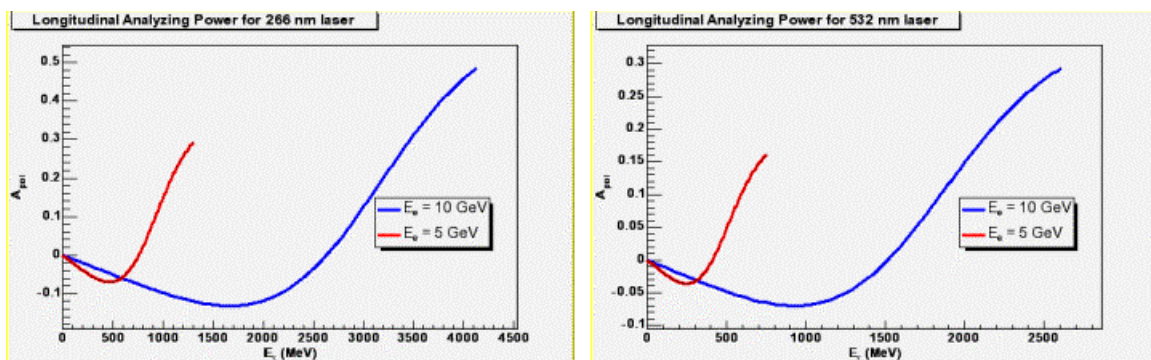


Figure 2.5-3: Analyzing powers as a function of scattered photon energy for longitudinal Compton polarimeters with 266 nm (left plot) and 532 nm (right plot) lasers at electron energies of 5 GeV (red) and 10 GeV (blue).

The selection of a laser system will also be influenced by intensity requirements. It has been observed in other colliders that significant variation in polarization between bunches can occur. The laser should be sufficiently powerful to provide a statistically precise measurement of the polarization for

each fill. With commercially available UV lasers of order 10 Watts, it is estimated that statistical precision of better than 1% in the polarization can be attained within an hour. However, there is substantial uncertainty in the background that will be generated by bremsstrahlung from residual gas, which will be dependent upon vacuum conditions. It is also desirable to have sufficient laser intensity to accurately sample the electron polarization on a pulse-by-pulse basis. One possible option for increasing the laser intensity is the use of a Fabry-Perot amplification cavity. Such a device is in operation in the Hall A Compton Polarimeter at Jefferson Lab [13] and is being instrumented in the HERA Longitudinal Polarimeter. Such a device could substantially increase the statistical accuracy of polarization measurements at eRHIC. If such a system is planned, it should be included early in the design of the polarimeter interaction region. The use of an amplification cavity would require enclosure in the vacuum system. It may restrict the crossing angle between the laser and electron beam and would influence both the laser and electron optics. In addition, the use of a build-up cavity may limit the frequency at which the laser helicity can be changed. Such an arrangement is acceptable for external beams for which the current remains constant and its polarization can be reversed pulse-by-pulse. In the eRHIC ring where the electron beam polarization cannot be frequently reversed, it is desirable to be able to change the laser circular polarization frequently. The performance of the cavity in the HERA Longitudinal Polarimeter should provide a good basis for evaluating the utility of such devices in storage rings.

Besides raising the laser power, the statistical accuracy of the polarization measurement can be improved by either lengthening the interaction region or tightly focusing the laser and introducing a small crossing angle between the beams. The desired crossing angle between the laser and the electron beam will dictate the design of the laser optics. For very small angles of incidence, long focal length lenses are required. Provision must also be made for introducing the laser into the ring's vacuum system. The transverse polarimeter at HERA features a crossing angle of 3 mrad between the laser and electron beam [14]. A comparable crossing angle for eRHIC appears desirable as a means of defining the Compton scattering vertex accurately. The laser systems in most polarimeters suffer at some level from helicity-dependent translations of the laser position. The use of a larger crossing angle decreases the sensitivity of the scattering vertex position to such translations, thereby reducing systematic false asymmetries resulting from helicity-dependent luminosity and helicity-dependent laser trajectories. The use of a well-focused laser can also allow measurements of the beam's intensity and polarization profile if highly stable optical mounts and feedback are used to stabilize the laser and electron trajectories. The use of a crossing angle has the additional benefit that optics can be removed and from the vacuum system from the line of sight of backscattered photons. This allows for easier access, increases versatility and minimizes damage to the optics. It also allows circular polarization to be generated close to the interaction region substantially reducing polarization transport asymmetries.

2.5.4 Detection options

The eRHIC Compton polarimeters will require detectors capable of analyzing backscattered photons, scattered electrons, or both. There are precedents for both options. Most Compton polarimeters have relied on gamma ray calorimeters. The use of a calorimeter for scattered photons is a scheme offering many attractive features. It is proven technology, having been used in a number of laboratories. Calorimeters consisting of dense materials such as lead glass or cesium iodide can be constructed in a compact manner for relatively low cost. The photon kinematics also features a

correlation between angle and energy. A segmented calorimeter can use this information for beam alignment and reduction of instantaneous rate. This correlation is essential to preserve in the transverse polarimeter as it forms the basis for the polarization measurement.

The primary concern related to photon calorimetry is the intensity of the eRHIC electron beam. The electron beams of eRHIC will be the most intense beams to use Compton polarimetry. While the beam intensity will increase the rate of backscattered photons, thereby improving the statistical accuracy of measurements, it will also produce substantial background from bremsstrahlung. Because this radiation is emitted in the same direction and cannot be distinguished from backscattered photons, a creative solution will be required to eliminate background contributions to the measurement. At the very least, highly segmented detectors and fast data acquisition systems will be required with proper gain matching and summing of detectors. Even very fast scintillators will suffer serious problems with piled up pulses. Operation in a single-photon counting mode is likely to prove impossible. Operation in multi-photon mode works well from a statistical point of view, but relies heavily on very accurate modeling of the polarimeter's analyzing power and stable performance of the calorimeter.

A possible alternative or complementary approach involves detection of the scattered electron. This approach has not been used often in polarimetry, but has been used to produce tagged photon beams at facilities including such as LEGS [15] at Brookhaven's NSLS. Detection of the electron would require some sort of magnetic field for momentum analysis. A magnetic analyzer could range from a bending magnet to a separate magnetic channel, possibly including a septum magnet to separate scattered electrons from the beam. Any such device would have to include a robust position-sensitive detector.

The use of a magnetic spectrometer would have a few significant advantages over a calorimeter. Foremost among these is that the energy analysis would allow an energy spectrum to be constructed for any segmented detector. It would not be necessary to run in an integration mode. Each cell of the detector could produce its own asymmetry which could be compared to the projected shape from Monte Carlo simulations.

Another important advantage is that the spectrometer would serve as a filter for the rejection of bremsstrahlung. This is particularly significant because the electrons producing very high energy bremsstrahlung photons, would not traverse the spectrometer.

There are many open questions and issues related to detection of the electron. This detection scheme clearly requires additional space in the polarimeter interaction region. The use of a septum magnet could lead to problems with radiation and beam storage. The introduction of a new magnetic field would affect the beam trajectory and may complicate efforts to account for spin precession correctly. It would significantly complicate the interpretation of positional information for the transverse polarimeter. Also, unless the scattering vertex between the laser and electron beam is very well defined, the acceptance of the spectrometer could be helicity-dependent and variable. The nonlinear relationship between the energy of the Compton edge and the beam energy would increase the demands for the necessary momentum bite and resolution. Momentum resolution of at least 1% would be desirable at both 5 and 10 GeV.

One possible compromise would involve combining the two approaches. The benefits of coincident detection of scattered electrons and backscattered photons have been demonstrated in the Jefferson

Lab Hall-A Compton Polarimeter. The photon counters are fast plastic scintillators with low energy resolution. Energy analysis is provided by a bending magnet and a silicon detector internal to the vacuum system. A similar approach could be considered for eRHIC polarimetry, in which the asymmetry is based on a photon counter, but complementary information on the energy resolution is obtained by detecting the electron for a limited fraction of events.

2.5.5 Summary

Overall, the outlook for electron polarimetry at eRHIC appears promising. No insurmountable hurdles are foreseen in the construction of laser-backscattering polarimeter. Realistic estimates for statistical precision can be obtained by looking at the performance of existing Compton polarimeters. For the Hall-A Polarimeter at Jefferson Lab, statistical uncertainties of 1% are obtained within an hour for a 4 GeV electron beam. Raising the beam energy reduces the time needed to reach this level of precision. The HERA Longitudinal Polarimeter at 27 GeV reaches this level of precision in about one minute.

The accuracy of beam polarization measurements will ultimately be limited by systematic errors. SLAC has reduced systematic uncertainties to the level of 0.5% for an external 46 GeV beam. Systematics of 1-2% are more commonly attained, although reaching this level is not trivial. All depend on specifics of the instrument, but are often dominated by modeling of the analyzing power, detector stability, and beam alignment issues. Careful consideration of these issues from the outset will increase the chance of success.

References:

1. http://www.phenix.bnl.gov/WWW/publish/abhay/Home_of_EIC/e_polarimetry/epol_8nov2002_ws.html
2. T.J. Gay and F.B. Dunning, Rev. Sci. Instrum 63 (1992) 1635.
3. T.J. Gay et al, Phys Rev A, 53 (1996) 1623.
4. C. Cacho et al, Phys Rev Lett, **88** (2002) 066601.
5. H.R. Band et al, Nuclear Instruments and Methods **A400** (1997) 24.
6. V.S. Morozov et al, Phys Rev ST Accel. Beams **4** (2001) 104002 .
7. D.P. Barber et al, Nuclear Instruments and Methods **A329** (1993) 79-111.
8. D.P. Barber et al, Physics Letters B **343** (1995) 436-443.
9. M. Beckmann et al, Nuclear Instruments and Methods **A479** (2002) 334-348.
10. I. Passchier et al, Nuclear Instruments and Methods **A414** (1998) 446-458.
11. W.A. Franklin et al, AIP Conf Proc **675** (2002) 1058-1062.
12. N. Falletto et al, Nuclear Instruments and Methods **A459** (2001) 412-425.
13. N. Falletto et al, Nuclear Instruments and Methods **A459** (2001) 412-425.
14. D.P. Barber et al, Nuclear Instruments and Methods **A329** (1993) 79-111
15. C.E. Thorn et al, Nuclear Instruments and Methods **A285**(1989) 447.